

A SYSTEMATIC SEARCH FOR THE REDDEST FAR-INFRARED AND SUB-MILLIMETER GALAXIES: REVEALING DUST-EMBEDDED STARBURSTS AT HIGH REDSHIFTS

HAOJING YAN,¹ ZHIYUAN MA,² JIA-SHENG HUANG,³ AND LULU FAN^{4,5,6}

¹*Department of Physics and Astronomy, University of Missouri-Columbia, USA*

²*Department of Astronomy, University of Massachusetts, Amherst, USA*

³*CASSACA, National Astronomical Observatories, Chinese Academy of Sciences, Beijing 100012, China*

⁴*CAS Key Laboratory for Research in Galaxies and Cosmology, Department of Astronomy, University of Science and Technology of China, Hefei 230026, China*

⁵*School of Astronomy and Space Sciences, University of Science and Technology of China, Hefei, Anhui 230026, China*

⁶*Shandong Provincial Key Lab of Optical Astronomy and Solar-Terrestrial Environment, Institute of Space Science, Shandong University, Weihai, 264209, China*

ABSTRACT

We present the results of our systematic search for the reddest far-infrared (FIR) and submillimeter (sub-mm) galaxies using the data from the Herschel Multi-tiered Extragalactic Survey (HerMES) and the SCUBA2 Cosmological Legacy Survey (S2CLS). The red FIR galaxies are “500 μm risers,” whose spectral energy distributions increase with wavelength across the three FIR passbands of the Spectral and Photometric Imaging REceiver (SPIRE) of Herschel. Within 106.5 deg^2 of the HerMES fields, we have selected 629 500 μm risers. The red sub-mm galaxies are “SPIRE dropouts,” which are prominent detections in the S2CLS 850 μm data but are extremely weak or invisible in the SPIRE bands. Within the 2.98 deg^2 common area of HerMES and S2CLS, we have selected 95 such objects. These very red sources could be dusty starbursts at high redshifts ($z \gtrsim 4\text{--}6$) because the peak of their cold-dust emission heated by star formation is shifted to the reddest FIR/sub-mm bands. The surface density of 500 μm risers is $\sim 8.2 \text{ deg}^{-2}$ at the $\geq 20 \text{ mJy}$ level in 500 μm , while that of SPIRE dropouts is $\sim 19.3 \text{ deg}^{-2}$ at the $\geq 5 \text{ mJy}$ level in 850 μm . Both type of objects could span a wide range of redshifts, however. Using deep radio data in these fields to further select the ones likely at the highest redshifts, we find that the surface density of $z > 6$ candidates is 5.5 deg^{-2} among 500 μm risers and is $0.8\text{--}13.6 \text{ deg}^{-2}$ among SPIRE dropouts. If this is correct, the dust-embedded star formation processes in such objects could contribute comparably as Lyman-break galaxies to the global SFR density at $z > 6$.

Keywords: galaxies: high-redshift; galaxies: starburst; infrared radiation; (ISM:) dust, extinction

1. INTRODUCTION

A surprising fact that has recently emerged from the exploration of the early universe is that very dusty starburst galaxies exist at $z > 6.3$, which is in the epoch of cosmic hydrogen reionization (EoR; e.g., Fan et al. 2006; Planck Collaboration et al. 2016). Some of these objects were discovered using quasars at $z \gtrsim 6\text{--}7$ as probes, revealed as either being their host galaxies (e.g., Walter et al. 2003; Venemans et al. 2012, 2016, 2017), or being their companions (Decarli et al. 2017),

and some were discovered by targeting sources found in far-infrared (FIR) to submillimeter/millimeter (sub-mm/mm) surveys (Riechers et al. 2013; Strandet et al. 2017). Their IR luminosities (L_{IR} ; integrated over rest-frame $8\text{--}1000 \mu\text{m}$) are so high that they qualify as ultra-luminous infrared galaxies (ULIRGs; $L_{\text{IR}} \geq 10^{12} L_{\odot}$), and the inferred star formation rates (SFRs) are often an order of magnitude higher than those of the most luminous galaxies at the same redshifts found through the conventional “dropout” technique based on rest-frame UV emission. Therefore, there is a possibility that dust-embedded star formation activities in the universe could exceed those “exposed” ones even in such an early epoch. Most of these currently known dusty starbursts in the EoR are invisible in the deep rest-frame UV images, and thus their dust-hidden star formation cannot be recovered through the extinction-corrected UV emission. Their huge amount of dust suggests very active star formation in even earlier epochs and a short time scale of

yanha@missouri.edu

zhiyuanma@umass.edu

jhuang@nao.cas.cn

llfan@ustc.edu.cn

metal enrichment throughout the ISM, both of which remain to be verified by future observations. This population also impacts our understanding of the intergalactic medium (IGM) in the early universe. The necessary condition for the reionization to happen is a strong Lyman photon background, which is already difficult to account for unless the UV luminosity functions of galaxies at $z > 6$ have very steep faint-end slopes (e.g., Yan & Windhorst 2004; Yan et al. 2010; Bouwens et al. 2015). The existence of dusty starbursts at $z > 6$, albeit only a small number having been confirmed to date, indicates that dust could already be ubiquitous in galaxies when the universe was merely a few hundred million years old. This would exacerbate the tight situation in explaining the Lyman photon budget for reionization, as dust blocks UV light and thus would significantly decrease the Lyman photon escape fraction.

Currently, the sample of confirmed dusty starbursts in the EoR is still very small. The most promising, unbiased way (i.e., without being tied to the known high- z quasars) to significantly increase the sample size is to do sub-mm/mm spectroscopy on large sets of candidates preselected based on their spectral energy distributions (SEDs) in the FIR-to-mm regime. Such a preselection has recently been made possible by the wide-field FIR surveys done using the Spectral and Photometric Imaging Receiver (SPIRE; Griffin et al. 2010) onboard the Herschel Space Observatory (Pilbratt et al. 2010), which offered high-sensitivity photometry in its three broad bands at 250, 350, and 500 μm . *Herschel* completed two major extragalactic surveys with this instrument, namely the Herschel Astrophysical Terahertz Large Area Survey (H-ATLAS; Eales et al. 2010; Smith et al. 2017) over $\sim 660 \text{ deg}^2$ in five areas and the Herschel Multi-tiered Extragalactic Survey (HerMES; Oliver et al. 2012) over $\sim 70 \text{ deg}^2$ in six tiered levels of depth and spatial coverage combinations (the released data actually cover wider areas). In addition, HerMES extended beyond its shallowest tier to the Herschel Stripe 82 Survey (HerS; Viero et al. 2014) and the HerMES Large Mode Survey (HeLMS; see Asboth et al. 2016), which observed ~ 80 and $\sim 280 \text{ deg}^2$ in and around the Sloan Digital Sky Survey Stripe 82 region, respectively. Combining all of these surveys, there are now over a million FIR sources awaiting exploration.

Tailored for the SPIRE bands, the so-called “500 μm peaker” or “500 μm riser” technique selects candidates of high-redshift ULIRGs by searching for sources that are progressively brighter from 250 to 500 μm (Pope & Chary 2010; Roseboom et al. 2012). This is based on the fact that young stars nominally can only heat dust to a few tens of kelvin, and therefore the FIR/sub-mm SED can be approximated well by a modified blackbody (MBB) emission that has a broad peak at roughly 80–100 μm . Within the SPIRE bands, this peak would move to the redder side of 250 μm at longer wavelengths if the object is at $z \gtrsim 4$, and hence the SED shows a rising trend from 250 to 500 μm . This method has directly resulted in the ULIRG at $z = 6.337$ presented by Riechers et al. (2013), which was then the redshift record holder among all dusty starbursts that are not related

to quasars. The current record holder in this category, which is at $z = 6.900$ (Strandet et al. 2017, selected as a red mm source), is also a 500 μm riser based on its SPIRE photometry obtained after the source redshift was identified. Admittedly, this method has the drawback that it does not have sufficient resolution power in redshift; instead, it can only select sources at $z \gtrsim 4$ in general. This is due to the degeneracy between dust temperature (T_d) and redshift (see, e.g. Pope & Chary 2010): a lower T_d and a fixed redshift would shift the peak of the SED to a longer wavelength, which would be the same behavior if T_d is kept the same but the source is moved to a higher redshift. Regardless, this method is still the most effective in producing a large number of legitimate candidates at $z \gtrsim 4$ in a comprehensive manner, and the samples at different redshift ranges will need to be separated after spectroscopic identification. The latter is particularly important for the study of objects in the EoR, as they might constitute only a small fraction among the candidates thus selected.

Using the early HerMES data, Dowell et al. (2014) presented the first systematic search for 500 μm risers in three fields (First Look Survey, Lockman Hole, and GOODS-North) totaling 21 deg^2 , which resulted in 38 objects. They used the “difference map” technique, where the candidate selection is done on the difference map between the 500 and the 250 μm maps after smoothing the latter to the beam size of the former (i.e., from $17.''6$ to $35.''2$ FWHM) and assigning some certain weights to each. Asboth et al. (2016) applied the same method to the 274 deg^2 HeLMS field and published 477 500 μm risers. Ivison et al. (2016) took a different approach in the 660 deg^2 H-ATLAS fields. These authors started from the goal of constructing the most complete source catalog: sources are first identified on the 250 μm map (which has the best solution and sensitivity) and removed from the 350 and the 500 μm maps, additional sources are identified on these 350 and 500 μm residual maps, and candidate 500 μm risers are then selected from this complete catalog. They obtained 7961 500 μm risers in total, at least $\sim 26 \pm 5\%$ of which should be reliable. Donevski et al. (2018) used the similar methodology (but a different implementation) to search for 500 μm risers in the 55 deg^2 Herschel Virgo Cluster Survey, and selected 133 such objects.

An extension of the 500 μm riser technique to longer wavelengths has recently been proposed, which selects objects that continue the rising SED trend to the red side of 500 μm . Depending on the exact location of the redder band in use, it is referred to as the technique of “850 μm ” or “870 μm ” riser, etc. The dust emission peak of 850/870 μm risers should be at $\lambda_{\text{obs}} \gtrsim 850/870 \text{ } \mu\text{m}$, and thus statistically, they should be at higher redshifts than 500 μm risers. The first such object with confirmed redshift was presented by Riechers et al. (2017), which is an 870 μm riser and is at $z = 5.655$. Ivison et al. (2016) presented 850 and/or 870 μm observations for 109 of their 7961 500 μm risers, and only about three of them qualify as significant 850/870 μm risers (measured using $60''$ aperture and with $S/N \geq 5$). Duivenvoorden et al. (2018) carried out 850 μm follow-

up observations of 188 $500\ \mu\text{m}$ risers of [Asboth et al. \(2016\)](#) (67 are detected at $S/N \geq 5$), however none of them qualify as $850\ \mu\text{m}$ risers (regardless of S/N). These results suggest that such objects could be very rare.

In this work, we present our search of 500 and $850\ \mu\text{m}$ risers using the data from the HerMES program and the SCUBA2 Cosmological Legacy Survey (S2CLS; [Geach et al. 2017](#); [Michałowski et al. 2017](#)). As compared to the existing search of $500\ \mu\text{m}$ risers, ours is done at a fainter level than those by [Asboth et al. \(2016\)](#) and [Ivison et al. \(2016\)](#), and is over much large areas than those by [Dowell et al. \(2014\)](#) and [Donevski et al. \(2018\)](#). As explained in detail later, we do not directly select $850\ \mu\text{m}$ risers due to the limitation of the data. Instead, we select “SPIRE dropouts,” which are objects prominent in $850\ \mu\text{m}$ but very weak or invisible in SPIRE, as potential $850\ \mu\text{m}$ risers. A similar term, “Herschel drop-out”, was first used by [Boone et al. \(2013\)](#) when reporting a gravitationally lensed $870\ \mu\text{m}$ source that is invisible in Herschel data (including those obtained by SPIRE). Their follow-up study suggests a significant population of such objects in lensed fields ([Boone et al. 2015](#)), however the results are yet to be published. The next explicit reference to SPIRE dropout is in the recent paper by [Greenslade et al. \(2019\)](#), who present a serendipitous discovery of such an object in the H-ATLAS North Galactic Pole field. Our selection, on the other hand, is done in a systematic manner over the largest area available to date.

This paper is organized as follows. We first briefly describe the HerMES and the S2CLS data in §2. The selections of $500\ \mu\text{m}$ risers and SPIRE dropouts are detailed in §3 and §4, respectively. A source-by-source comparison to the known objects in the literature is given in §5. The radio properties of both types of objects are presented in §6. In §7, we discuss their surface densities, their prospects of being at high- z , and the implication of dust-embedded star formation in the early universe. Finally, we summarize our results in §8. The full catalogs of both types of objects as well as the ancillary catalogs are released with this paper. In our discussion, we adopt the following cosmological parameters: $\Omega_M = 0.27$, $\Omega_\Lambda = 0.73$, and $H_0 = 71\ \text{km s}^{-1}\ \text{Mpc}^{-1}$.

2. PRIMARY DATA SETS

Here we describe the data used in our selection of high- z ULIRG candidates, which are those from the HerMES and the S2CLS programs. Some other ancillary data that we use in our analysis of the candidates will be described in the relevant sections separately because such data are different in different fields.

2.1. HerMES FIR data

We used the SPIRE maps and the source catalogs included in the fourth data release (“DR4”) of the HerMES program¹. These maps were created using the algorithm as described in [Levenson et al. \(2010\)](#) and

[Viero et al. \(2013\)](#), and incorporated all the HerMES SPIRE observations as well as the latest calibration updates. The three-band source catalogs were extracted based on the “blind” $250\ \mu\text{m}$ positions (referred to as “xID250”), which were done in the same way as in the earlier releases ([Wang et al. 2014](#)). We did not use the PACS data, as these are not sensitive enough for our purpose.

The fields used in our study are listed in Table 1. These do not include any of the HerMES cluster fields, nor the two new fields that are not in the nominal HerMES program, namely SA13 ($0.17\ \text{deg}^2$) and XMM-13hr ($0.56\ \text{deg}^2$). Furthermore, we had to exclude the Boötes field because its DR4 xID catalog does not have $500\ \mu\text{m}$ photometry due to a software problem whose nature is still not yet clear². The field sizes listed in the table were calculated by counting the number of pixels that have values > 1.0 in the coverage maps as included in the third extension (“EXP”) of the released maps. In total, these data cover $106.54\ \text{deg}^2$.

2.2. S2CLS

As one of the JCMT Legacy Surveys, S2CLS was designed to do deep SCUBA2 mapping of eight well-studied extragalactic fields, mostly in $850\ \mu\text{m}$ ([Geach et al. 2017](#)). The $850\ \mu\text{m}$ maps and the source catalogs have been released to the public, and we refer the reader to [Geach et al. \(2017\)](#) for details. Five of these fields are within the HerMES coverage and hence are relevant to this work, which we list in Table 2. The listed field sizes were calculated by counting the pixels that are not assigned “NAN” in the RMS maps³. In total, these five fields cover $2.98\ \text{deg}^2$.

3. SELECTION OF $500\ \mu\text{m}$ RISERS

By definition, $500\ \mu\text{m}$ risers are the strongest in $500\ \mu\text{m}$ and become successively weaker in 350 and $250\ \mu\text{m}$, and thus ideally, the selection should be done using a source catalog whose detection is based on the $500\ \mu\text{m}$ map. However, as the $500\ \mu\text{m}$ band has the worst spatial resolution (FWHM beam size of $36''$) and hence the worst blending problem, a $500\ \mu\text{m}$ -based source extraction would often result in meaningless color measurements because a seemingly single $500\ \mu\text{m}$ source might well be a blend of two or more sources at shorter wavelengths. Therefore, we took a two-step approach. First, we used the HerMES xID catalogs, which are based on the $250\ \mu\text{m}$ detections and take advantage of the best spatial resolution available (FWHM beam size of $18''$) to search for $500\ \mu\text{m}$ risers that are still visible in $250\ \mu\text{m}$. We then subtracted off all the sources at the reported xID $250\ \mu\text{m}$ positions from the $500\ \mu\text{m}$ maps and

² This has been a persistent problem in this field since the previous HerMES data release (DR3), which is noted in the DR3 documentation. Basically, the photometric code running on its $500\ \mu\text{m}$ map returns all zero values for the flux densities.

³ The released S2CLS maps in the COSMOS field actually incorporate some observations from a sequel program “S2-COSMOS” ([Simpson et al. 2019](#)); however, the S2CLS source catalog in this field is still largely confined to the footprint covered by the S2CLS when it ceased operation ($\sim 1.35\ \text{deg}^2$).

¹ Released in 2016 July; see <https://hedam.lam.fr/HerMES/index/dr4>

extracted sources again on the residual 500 μm maps to find those 500 μm sources that are too faint to enter the 250 μm -based catalogs. Our procedures are detailed below.

3.1. Selection Based on HerMES DR4 xID Catalogs

The first pass was to use the xID catalogs to select 500 μm risers that satisfy these criteria:

$$f_{500}/et_{500} \geq 5 \text{ and } f_{500} > f_{350} > f_{250}. \quad (1)$$

Here we adopt the naming convention of the HerMES DR4, where f_{250} , f_{350} and f_{500} are the flux densities in 250, 350 and 500 μm , respectively, while et_{250} , et_{350} and et_{500} are the total errors in these three bands, respectively (including the contributions from both the instrumental noise and the confusion noise). In other words, the above criteria select objects that have $S/N \geq 5$ in 500 μm , and have successively increasing SEDs from blue to red. The latter is effectively the same as that of Dowell et al. (2014) and Asboth et al. (2016), because these authors search for positive signals on their difference maps (see §1). This is also similar to that used by Donevski et al. (2018), with the difference that they also require $f_{250} > 13.2$ mJy and $f_{500} > 30$ mJy. We note that Ivison et al. (2016) use different color criteria that require $f_{500}/f_{350} \geq 0.85$ and $f_{500}/f_{250} \geq 1.5$.

3.2. Selection Based on 500 μm residual maps

In the second pass, we used the Herschel Interactive Processing Environment (HIPE; Ott 2010), which is the standard software package of Herschel for handling its data, to create the base images for the analysis. For a given field, we ran the HIPE routine `subtractedFromImage` to subtract off all the sources in the xID catalog, regardless of their reported S/N (some have S/N as low as ~ 1 in 250 μm). This left residual images in all three SPIRE bands.

We then used the 500 μm residual image to detect sources and to obtain photometry in all three bands simultaneously, following the general approach as described in Wang et al. (2014). We first ran the `StarFinder` software (Diolaiti et al. 2000) to extract sources, with the two critical parameters `correlation.threshold`, set to 0.9, and `min.sourcedist`, set to 1. The list of sources were then passed to the HIPE task `sourceExtractorSimultaneous` to obtain the fluxes and the detection errors of the sources in all three bands on the residual maps. HIPE does not produce total errors that include the confusion noise, which we had to derive based on the HerMES xID catalog of the field. The catalog reports both the detection error (due to the instrumental noise alone) and the total error for a given source, the latter of which is computed by adding the terms due to the detection error and the confusion noise error in quadrature. This allowed us to calculate the

confusion noise error term for all the sources. We plotted the histogram of this term in each band and adopted the peak value as the overall confusion noise in this band for all the new sources that we found.

A complication that we had to deal with was that the residual 250 μm map is not completely clean because the subtraction can never be perfect. The “leftover” of a bright 250 μm source on the residual 250 μm map, while not included in the new 500 μm source list as described above, can still skew the flux measurement of a newly found 500 μm source in the simultaneous three-band photometry step if it is too close to the position of the new 500 μm source in question. We did not have a better choice other than discarding the affected 500 μm sources completely, which was done in a “cleaning” step. We ran the HIPE task `sourceExtractorSussextractor` with `detThreshold=3` on the 250 μm residual map to identify any significant leftover signatures, and then removed all the sources in our 500 μm residual-map-based catalog that are within $36.''15$ of any of the 250 μm leftover signatures⁴.

The additional 500 μm risers in a given field were then selected from the “cleaned” catalog using the same criteria as in Equation 1.

3.3. Final catalogs

We visually examined the candidates selected above in all three SPIRE bands to reject any possible contaminants. In most cases, the contamination is either due to a false positive in 500 μm or due to severe blending that makes the photometry (especially that in 500 μm) unreliable. We have created our final catalogs in two tiers. In the Tier 1 catalogs, we only retain those objects that are visually prominent in 500 μm and are the least affected by blending. Some of them still have close neighbors; however, we have judged based on our experience that their photometry should still be reliable. There are also a significant number of borderline cases that cannot be included in the Tier 1 catalogs. For the sake of completeness, we put them to the Tier 2 catalogs. In Figure 1, we show some examples of the objects in both tiers as well as the rejected contaminants. Table 1 summarizes the distribution of 500 μm risers in all 11 fields, and the full catalogs of Tier 1 objects are presented in Table 13. The Tier 2 objects are given in Appendix.

In the rest of this paper, we will only discuss the Tier 1 objects. Figure 2 shows their flux density and color distributions. The median of f_{500} for the xID-based and the residual-based objects is 32.3 and 35.1 mJy, respectively, while that for the whole sample is 33.2 mJy. Figure 3 shows their spatial distribution on top of the 250 μm error images that are used to indicate the sensitivity levels of the survey in different areas (smaller errors, or lighter regions, indicate higher sensitivities).

⁴ In theory, the “leftover” of a bright 350 μm source would create the same problem, but in practice we found that this did not need to be treated separately. This is because the 350 μm band is much less sensitive than the 250 μm band, and the vast majority of the 350 μm leftover signatures are already included in the 250 μm cases.

Table 1. Summary of 500 μm riser Tier 1 sample

HerMES Field	Area (deg ²)	$N_{\text{conf}}^{500\mu\text{m}}$ (mJy)	N_x	\tilde{f}_{500}^x (mJy)	N_R	\tilde{f}_{500}^R (mJy)	N_{tot}	\tilde{f}_{500} (mJy)	Σ (deg ⁻²)
ADFS	7.93	4.72	24	37.1	16	34.5	40	35.2	5.04
CDFS	12.57	3.63	123	27.9	17	20.9	140	27.6	11.14
COSMOS	4.76	4.90	25	30.8	0	...	25	30.8	5.25
EGS	3.30	4.05	24	27.4	2	32.9	26	28.3	7.88
ELAIS-N1	12.71	4.70	45	35.0	6	43.0	51	35.7	4.01
ELAIS-N2	8.29	5.10	25	38.2	14	37.3	39	37.3	4.70
ELAIS-S1	8.46	4.30	50	29.5	18	29.9	68	29.7	8.04
FLS	6.91	5.10	31	38.8	10	39.3	41	38.8	5.93
GOODS-N	0.63	3.31	6	25.8	0	...	6	25.8	9.52
Lockman	20.31	4.30	103	30.5	38	33.4	141	30.7	6.94
XMM-LSS	20.67	6.05	31	42.2	21	39.7	52	41.3	2.52

NOTE— $N_{\text{conf}}^{500\mu\text{m}}$ is the confusion noise of the 500 μm map, which we use as a proxy to the sensitivity of the map. N_x and N_R are the number of 500 μm risers selected based on the HerMES DR4 xID catalog and the 500 μm residual map, respectively, while \tilde{f}_{500}^x and \tilde{f}_{500}^R are their corresponding median f_{500} value. N_{tot} is the total number of objects selected in the field, and \tilde{f}_{500} is their median f_{500} value. Σ is the surface density based on the total, which is affected by the survey limit of the field (see §7.1).

Table 2. Summary of SPIRE dropout Tier 1 sample

S2CLS Field	Area (deg ²)	N	S_{850}^{med} (mJy)	Σ (deg ⁻²)
COSMOS	1.34	26	6.3	19.4
EGS	0.32	6	5.3	18.8
LH	0.28	3	6.3	10.7
GOODS-N	0.07	3	6.7	42.9
UDS	0.94	57	4.5	60.6

NOTE—N is the total number of SPIRE dropouts found in the field (those found by Methods A and B combined) and S_{850}^{med} is the median deboosted S_{850} . Σ is the surface density, which is affected by both the survey limit and the size of the field (see §7.3). No correction of incompleteness or contamination is taken into account.

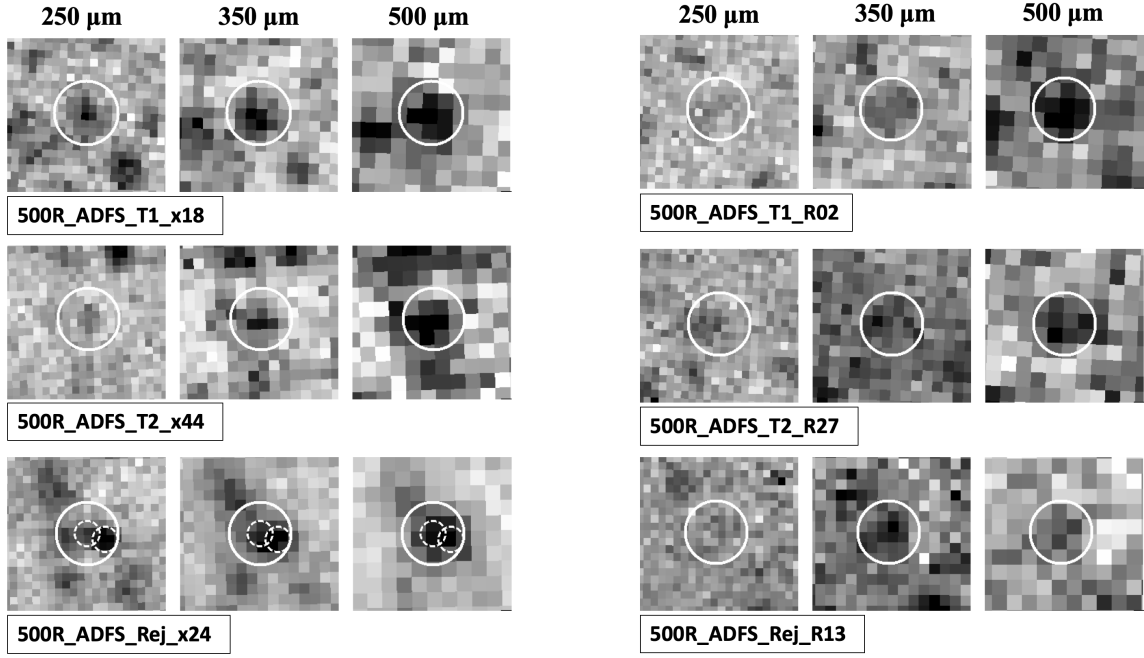


Figure 1. SPIRE image stamps of some $500\ \mu\text{m}$ riser candidates in the ADFS field as examples. The ones shown on the left panel are selected using the HerMES DR4 xID catalog, while those on the right panel are selected using the detections based on the $500\ \mu\text{m}$ residual map produced after subtracting the $250\ \mu\text{m}$ -detected sources. The labels in the boxes are the object IDs. The stamps are $2' \times 2'$ in size and are oriented north up and east left. The white circles are $25''$ in radius and are centered on the candidates. In each panel, (1) the images from left to right are in 250 , 350 , and $500\ \mu\text{m}$, respectively; (2) the first row is a Tier 1 object; (3) the second row is a Tier 2 object; and (4) the last row is a rejected contaminator. The rejected one in the left panel is due to unreliable photometry caused by two blended objects (indicated by the two small, dashed circles), while the one in the right panel is due to the false positive in $500\ \mu\text{m}$.

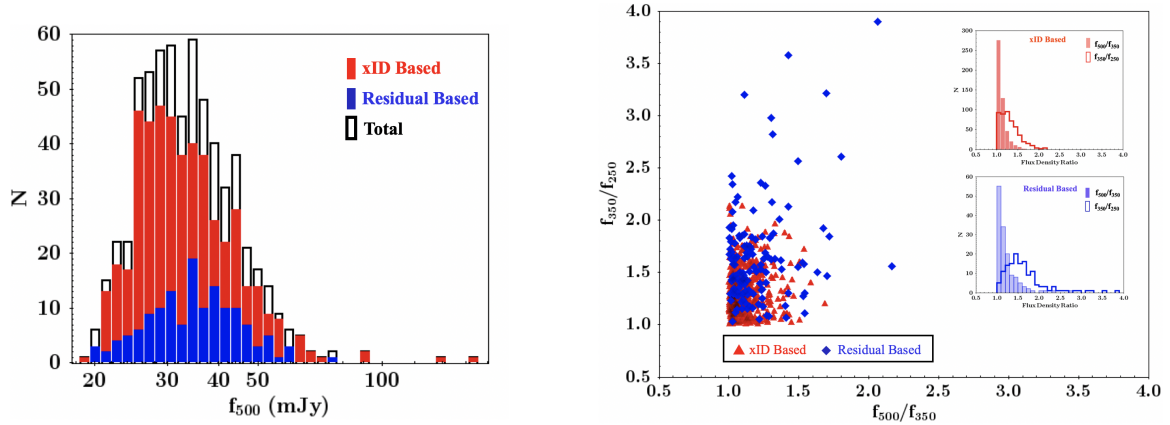


Figure 2. (Left) Distributions of f_{500} for the $500\ \mu\text{m}$ risers selected based on the HerMES DR4 xID catalogs (filled red) and the residual maps (filled blue), and the total (open black). (Right) Flux density ratios of the $500\ \mu\text{m}$ risers selected based on the HerMES DR4 xID catalogs (red triangles) and the residual maps (blue diamonds). The insets show the histograms of the ratios for the two sets, respectively.

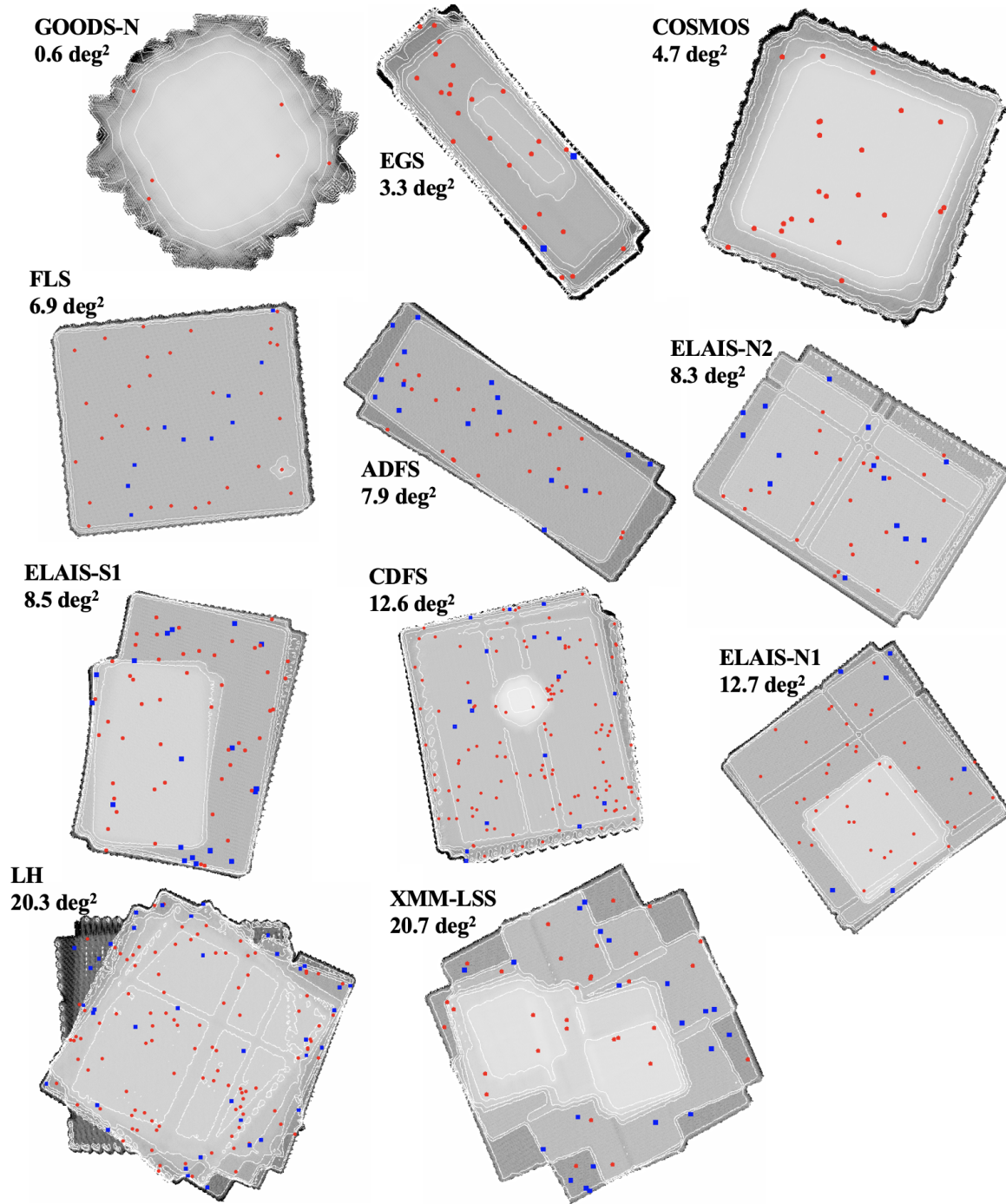


Figure 3. Positions of the 500 μm risers in each field selected based on the HerMES DR4 xID catalog (red circles) and the 500 μm residual map (blue boxes), overlaid on top of the 250 μm error map displayed in inverted gray scale. Smaller values on the error map (lighter regions) indicate deeper exposures. White contours are plotted on the error maps for the illustration purposes. The fields are shown in the order of their sizes (from left to right, and from top to bottom), but the sizes are not displayed to scale.

Table 3. Catalog of Tier 1 500 μm risers

ID	RA (degrees)	DEC (degrees)	f_{250} (mJy)	f_{350} (mJy)	f_{500} (mJy)	Radio Code	ID	RA (degrees)	DEC (degrees)	f_{250} (mJy)	f_{350} (mJy)	f_{500} (mJy)	Radio Code
500R_CDFS_T1_x004	52.7319600	-28.8153230	47.3 \pm 3.4	59.0 \pm 3.9	60.0 \pm 3.9	1	x176	52.5909230	-27.7079180	17.7 \pm 3.4	19.5 \pm 4.0	27.2 \pm 3.9	0
x007	52.5725400	-27.5764300	37.5 \pm 3.4	37.7 \pm 3.9	45.4 \pm 3.9	0	x177	52.5599670	-28.9544070	23.9 \pm 3.4	25.6 \pm 4.0	36.1 \pm 3.9	99
x009	53.7353200	-29.8309040	39.1 \pm 3.4	47.1 \pm 3.9	48.8 \pm 4.2	99	x178	53.5423740	-28.6750700	16.3 \pm 3.4	25.1 \pm 3.9	30.2 \pm 4.0	0
x162	52.6515000	-26.7467480	18.1 \pm 3.4	23.2 \pm 4.0	23.9 \pm 4.0	99	R32	53.9888420	-27.9607340	9.6 \pm 3.4	17.7 \pm 3.8	22.0 \pm 4.0	0
x166	51.7917800	-28.3055460	19.5 \pm 3.4	20.7 \pm 3.9	22.3 \pm 4.2	0	R33	54.0337730	-27.8183910	11.6 \pm 3.4	19.1 \pm 3.8	21.7 \pm 3.9	99
x170	52.7494700	-28.8928720	18.2 \pm 3.4	18.7 \pm 3.9	20.9 \pm 4.1	0	R37	52.8901080	-26.8169130	9.5 \pm 3.4	15.5 \pm 3.9	20.6 \pm 3.9	99

NOTE—Catalog of Tier 1 500 μm risers, using part of those in the CDFS as examples. The entire catalog is available in Appendix. When referred to in full, the object name consists of the leading string and the sequential ID. The leading string has the field name coded in. In addition, “T1” stands for “Tier 1.” For clarity, the leading string is omitted except in the first entry of the field. In the sequential ID, “x” or “R” indicates the method with which the object is selected (using the HerMES xID catalog or the residual map, respectively). The equatorial coordinates (J2000.0) are in degrees. The flux density and the total error are in the units of mJy. For those “x” objects, these are from the HerMES xID catalog, while for those “R” objects, these are based on our own photometry (see §3.2). The “Radio Code” indicates the status of the object in terms of radio observations (see §6.1 for details): “1” – detected in either FIRST and/or deeper radio data, “0” – covered by deeper radio data but not detected, and “99” – outside of the coverage of deeper radio data. The radio properties of those with code “1” and “0” are summarized in Tables 5, 7 and 8.

4. SELECTION OF SPIRE DROPOUTS AS POTENTIAL 850 μ M RISERS

We further selected potential 850 μ m risers in the five S2CLS fields. It would be natural to expect that a subset of the 500 μ m risers selected above in these fields could be 850 μ m risers. However, we found that none of them are. This is in part due to the limited SPIRE survey sensitivities. The noise in the HerMES maps is at the level of ~ 4 –5 mJy (confusion noise included), which means that a HerMES source at $S/N \sim 5$ would have a flux density of $\gtrsim 20$ mJy in the SPIRE bands. None of the S2CLS sources in these fields have $S_{850} > 20$ mJy.

On the other hand, we noticed that some of the S2CLS sources are very weak or invisible in the HerMES data. For simplicity, we shall refer to such 850 μ m sources as the “SPIRE dropouts.” It is impossible to judge at this stage whether these objects are 850 μ m risers, again because the sensitivity of the SPIRE data is too shallow to sufficiently constrain the SEDs at the bluer wavelengths. However, if 850 μ m risers do exist in these S2CLS fields, they must be among these SPIRE dropouts.

We selected the SPIRE dropouts in a two-step approach. We only considered the most reliable 850 μ m sources that have detection S/N (“detection.SNR” in the S2CLS catalogs) ≥ 5 . We first cross-matched these S2CLS sources with the HerMES sources in the xID catalogs, and found those that were missing from the latter. We refer to this step as the selection using “Method A.” The matching radius was chosen based on the positional uncertainties in both. Following Equations 1 and 2 in [Ma & Yan \(2015\)](#) (see also [Ivison et al. \(2007b\)](#)), the uncertainty σ_{pos} can be expressed as

$$\sigma_{\text{pos}} = \frac{0.6}{S/N} \sqrt{\theta_a^2 + \theta_b^2} = \frac{0.6 \times 1.414 \times \theta}{S/N}, \quad (2)$$

where θ_a and θ_b are the beam sizes along the major and the minor axes, respectively, and θ is the total beam size when the beam is symmetric. For the SCUBA2 850 μ m and the SPIRE 250 μ m, θ is 13'' and 18'', respectively. We treated the 250 μ m positions as being reliable if the

sources have $f_{250}/et_{250} \geq 3$. Plugging in $S/N = 5$ and 3 for 850 and 250 μ m, respectively, and adding in quadrature the two terms, we obtained the positional matching error of $\sigma_{\text{pos}} = 5.''55$, which we adopted as the matching radius.

In the next step, we also selected the matched 850 μ m sources that have $S/N < 3$ in 250 μ m. For a source below this limit, the SPIRE photometry is prone to large errors; while the reported SPIRE flux densities are still brighter than the 850 μ m one, the true situation could be the opposite. Therefore, this step was to make certain that we would not miss the real SPIRE dropouts whose “detections” in SPIRE are artificially boosted due to their low S/N in the HerMES data. We refer to this secondary step as the selection using “Method B.”

Similar to what was done with the 500 μ m risers, all of the above candidate SPIRE dropouts were visually examined to remove contaminations. The most common contaminators are due to blending, especially in the SPIRE bands. There are also cases where it was difficult to decide whether there was a detection in any of the SPIRE bands, and if yes, whether the weak detection would decrease the prospect of the candidate being a 850 μ m riser. The visual judgment on the latter was aided by using the reported SPIRE flux densities (despite them having large errors). Specifically, we required $(S_{850} + 0.5 \times \text{Err}S_{850}) > (f_{250} - 2 \times et_{250})$ to keep such a candidate, where $\text{Err}S_{850}$ and et_{250} are the errors in 850 μ m and 250 μ m, respectively. In both “A” and “B” categories, the most probable candidates were ranked as “Tier 1,” and the less probable ones were ranked as “Tier 2.” In Figure 4, we show some examples in both tiers as well as some rejected contaminators. The full catalogs of the Tier 1 objects are presented in Table 4, while those of the Tier 2 objects are given in Appendix. In the rest of this paper, we only discuss the Tier 1 objects. Their flux density distribution is shown in Figure 5, while their spatial distributions in different fields are shown in Figure 6.

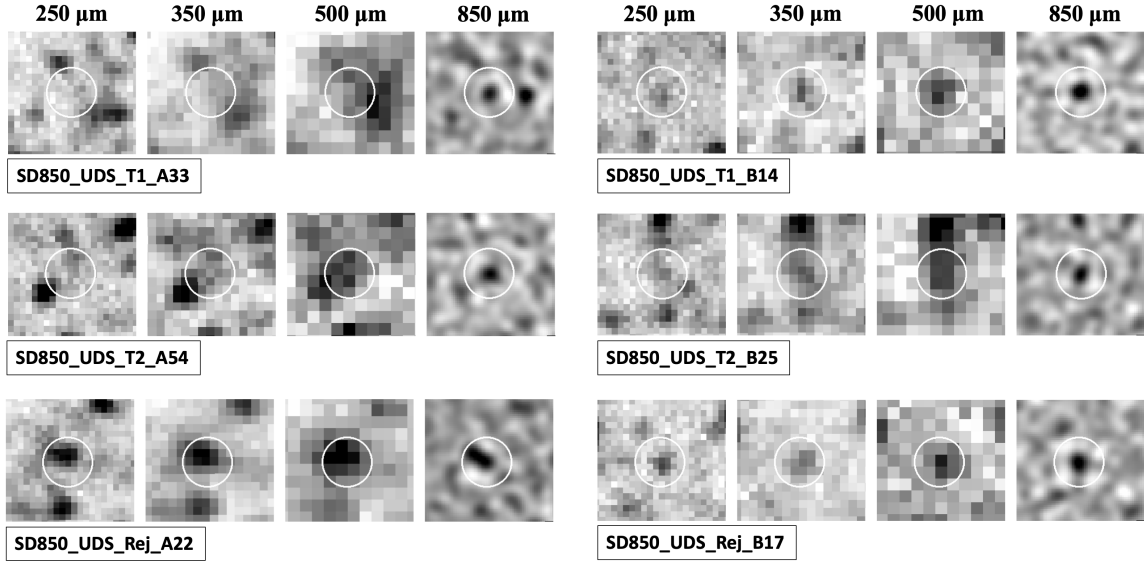


Figure 4. Image stamps of six candidate SPIRE dropouts in the UDS field as examples. The objects have their IDs labeled in the black box, which all use “SD850” as the leading string. The ones shown on the left panel are selected by Method “A” (designated by “A” in their IDs), which is to search for 850 μm sources that have no counterparts in the HerMES 250 μm -based xID catalog. The ones shown in the right panel are selected by Method “B” (designated by “B” in their IDs), which is to search for those that have very weak 250 μm counterparts ($S/N < 3$) in the xID catalog. The stamps are $2' \times 2'$ in size and are oriented North-up and East-left. The white circles are $25''$ in radius and are centered on the candidates. In each panel, (1) the images from left to right are the HerMES 250, 350, 500 μm and the S2CLS 850 μm , respectively, (2) the first row is a Tier 1 object, designated by “T1” in the ID, (3) the second row is a Tier 2 object, designated by “T2” in the ID, and (4) the last row is a rejected contaminator, designated by “Rej” in the ID. The contaminators shown here are representative of two common cases when the candidates have to be rejected. The one in the left panel has a very close neighbor, which severely contaminates the source position in 500 μm and therefore is difficult to judge if it is a real SPIRE dropout. The one in the right panel, despite being reported as a 250 μm source with $S/N < 3$ in the xID catalog, has very obvious detections in all three SPIRE bands, with reported $f_{250} = 13.6 \pm 4.6$ mJy. Given its $S_{850} = 5.6$ mJy, it is unlikely to be brighter in 850 μm than in the SPIRE bands.

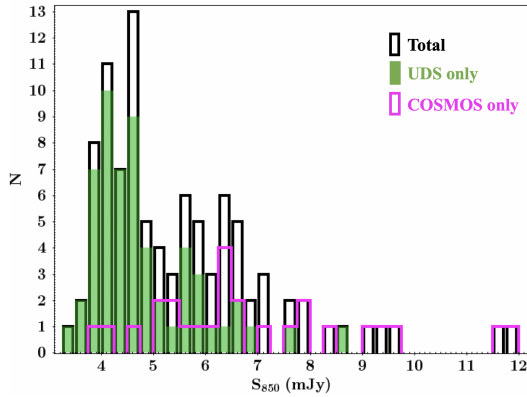


Figure 5. 850 μm flux density (S_{850}) distribution of the Tier 1 SPIRE dropouts in our sample (95 objects in total). The objects selected in the UDS field (57 objects; shown in green) make up 60.0%, most of which are at the faint end. Those in the COSMOS field (26 objects; shown in purple) are the next largest group in the sample and make up 27.3% of the total. There is a clear offset of the representative S_{850} values between the two subsets, which is largely due to the different survey limits in these two fields.

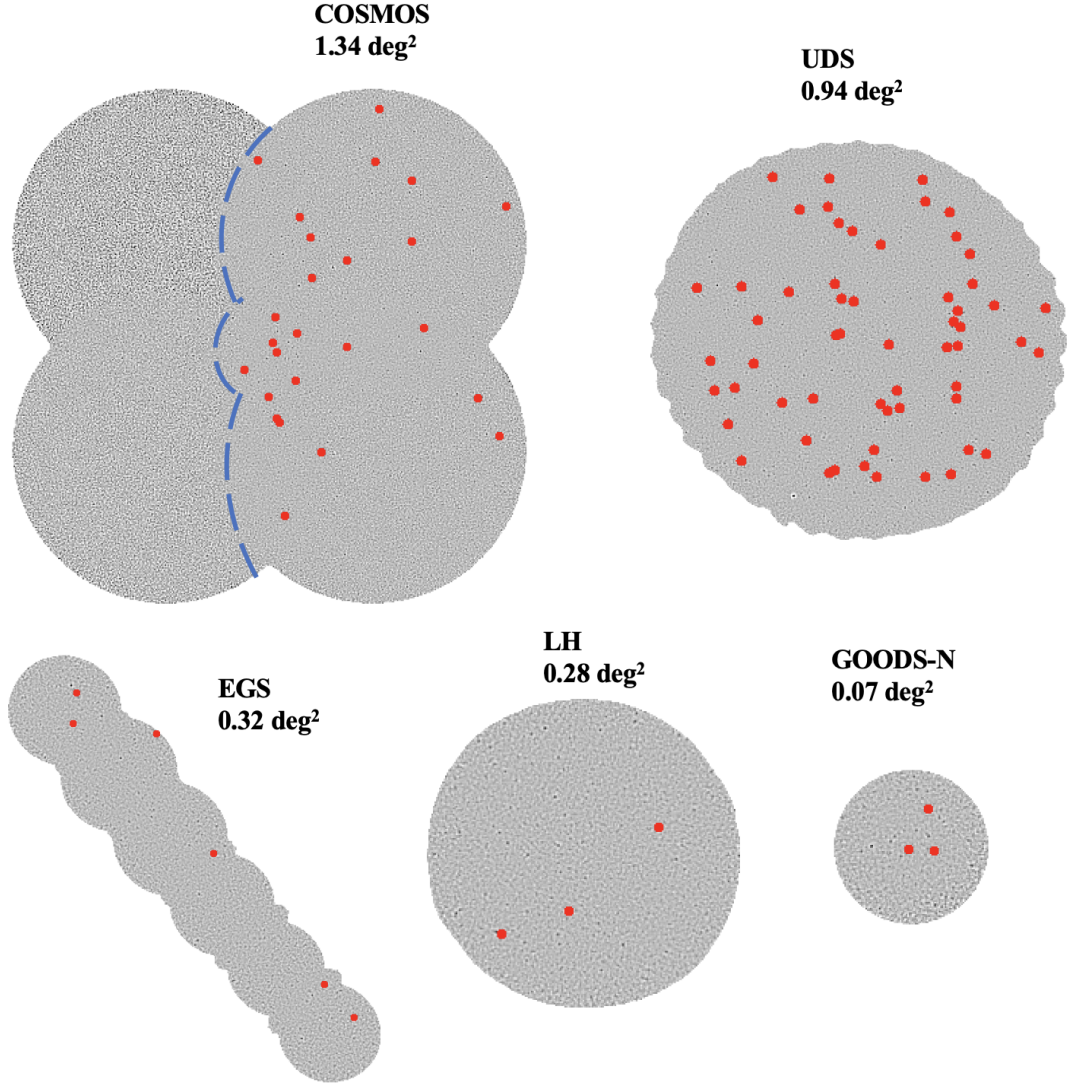


Figure 6. Positions of the SPIRE dropouts in each field (red dots) selected based on the S2CLS and the HerMES data, overlaid on the S2CLS 850 μm maps. The fields are shown in decreasing order of their sizes (from left to right, and from top to bottom), but the sizes are not displayed to scale. Note that the released map of the COSMOS field include the data from the S2XLS, however the S2CLS catalog (and hence our search in this field) is based on the S2CLS data only (the western part separated by the dashed curve) and covered 1.34 deg^2 .

Table 4. Catalog of Tier 1 SPIRE dropouts based on S2CLS 850 μm data

Object Name	RA ₈₅₀ (degrees)	DEC ₈₅₀ (degrees)	S/N ₈₅₀	S ₈₅₀ (mJy)	RA _{SPIRE} (degrees)	DEC _{SPIRE} (degrees)	f ₂₅₀ (mJy)	f ₃₅₀ (mJy)	f ₅₀₀ (mJy)	Δ ($''$)	Radio Code
SD850 COSMOS.T1.A02	150.038273	2.140164	9.0	9.0 ± 1.3	0
A03	149.989321	2.457937	8.7	11.8 ± 1.9	0
A04	149.792953	2.815101	8.3	11.7 ± 2.1	1
B03	150.109433	2.257389	6.7	5.5 ± 1.1	150.109220	2.256556	2.5 ± 3.4	3.4 ± 6.6	0.0 ± 13.0	3.1	0
B05	150.027677	2.642935	6.3	8.0 ± 1.8	150.027700	2.642787	3.9 ± 3.4	8.5 ± 6.6	12.9 ± 5.0	0.5	0
B06	150.088867	2.010723	6.0	6.3 ± 1.4	150.087950	2.011739	3.7 ± 3.4	5.5 ± 6.6	5.2 ± 5.2	4.9	1

NOTE—Catalog of Tier 1 SPIRE dropouts, using part of the entries in the COSMOS field as examples. The entire catalog is available in Appendix. When referred to in full, the object name consists of the leading string and the sequential ID. The leading string has the field name coded in. In addition, “T1” stands for “Tier 1”. For clarity, the leading string is omitted except in the first entry of the field. In the sequential ID, “A” or “B” indicates that the object is selected by Method A or B (see §4). RA₈₅₀ and DEC₈₅₀ are the equatorial coordinates (J2000.0) based on the positions given in the S2CLS catalog. The “deboosted” flux density in 850 μm from that catalog is reported under S₈₅₀. The “B” objects have weak SPIRE counterparts in the HerMES xID catalog, and their SPIRE positions and flux densities are listed under RA_{SPIRE} and DEC_{SPIRE}, f_{250} , f_{350} , and f_{500} , respectively. The separation between their SCUBA2 and SPIRE positions is given under “ Δ ”. “Radio Code” indicates whether the object is detected in the radio data (“1”) or not (“0”), or is outside of the radio data coverage (“99”), which is detailed in §6.2. The radio properties of those with code “1” and “0” are summarized in Table 10 and 11, respectively.

5. COMPARISON TO THE LITERATURE

While limited, there are some similar, very red FIR/sub-mm galaxies in the literature that are found in regions in common with this work. Here we compare these to our samples.

5.1. Comparison of 500 μm risers

The largest sample that we compare to is that of [Dowell et al. \(2014\)](#), which consists of 1, 18 and 21 500 μm risers in the GOODS-N, the FLS, and the LH fields, respectively.

The one in the GOODS-N, their GOODS-N 8, was selected as a candidate from the xID catalog in our first step; however, it was removed from the final catalog due to a blending problem.

In the FLS field, 8 of their 18 objects are in our Tier 1 catalog, namely their FLS 3, 5, 17, 19, 24, 25, 30, and 33 (FLS 3 is the $z = 6.34$ object HFLS3 reported in [Riechers et al. \(2013\)](#)). In addition, their FLS 20 is in our Tier 2 catalog. Five other objects are not in our sample but can be accounted for, namely, FLS 1, 6, 26, 31, and 32 (FLS 1 is at $z = 4.29$ as reported in [Dowell et al. \(2014\)](#)). Based on the DR4 xID catalog, the first four of them have $f_{350} > f_{500}$ and $f_{350} > f_{250}$, and thus are “350 μm peakers” instead of 500 μm risers. FLS 32 has $S/N < 5$ in 500 μm and hence does not meet our criteria. The remaining four objects, FLS 7, 22, 23, and 34, are not included either in the xID catalog or the catalog generated based on the photometry in the 500 μm residual map. Upon visual examination of the images, we find that (1) FLS 7 is severely affected by blending due to a much brighter neighbor; (2) FLS 22 is too close to the field edge, and neither the xID nor our own extraction on the residual map includes this object; (3) FLS 23 is missed most likely due to its faintness; and (4) FLS 34 must be a misidentification due to blending and thus not a real source.

In the LH field, three of their sources are included in our Tier 1 catalog, namely, their LSW 20, 25, and 102 (LSW 20 is at $z = 3.36$ as reported in [Dowell et al. \(2014\)](#)). Their LSW 28 was selected as a candidate in our first step but was later rejected due to the severe blending problem and its being too weak. Twelve of their sources are in the xID catalog (their LSW 26, 29, 31, 47, 48, 49, 50, 52, 53, 54, 55, 56, 58, 60, 76, 81, and 82) but were not selected by our procedure because they are all 350 μm peakers instead of 500 μm risers. The rest five objects, their LSW 49, 50, 55, 56, and 82 are not in either the xID catalog nor our catalog based on the residual map. Among them, LSW 50 is too faint in both 250 and 500 μm to be included, and the other four all suffer from severe blending.

The “prototype” 870 μm riser in [Riechers et al. \(2017\)](#), their ADFS-27, is a 500 μm riser in the first place (but not a SPIRE dropout); however, it is not included in our sample because it has $S/N = 4.4 < 5$ in 500 μm .

We note that two famous SMGs with known redshifts in GOODS-N, GN10 at $z = 4.04$ and GN20 at $z = 4.05$ ([Daddi et al. 2009a,b](#)), are also not included in our sample. The former one is severely blended with neighbors

and thus is not extracted, while the latter is actually a 350 μm peaker based on the xID catalog.

5.2. Comparison of SPIRE Dropouts

The only known SPIRE dropouts that we can compare to are the two millimeter galaxies reported by [Ikarashi et al. \(2017\)](#) in the XMM-LSS field, which were first detected by using ASTE/AzTEC at 1.1 mm ([Ikarashi et al. 2015](#)). Based on the subsequent identifications in the HerMES and the S2CLS data, [Ikarashi et al. \(2017\)](#) point out that they are secure detections in 850 μm but are invisible in the SPIRE data. These two objects, their ASXDF1100.053.1 and 231.1, are recovered in our SPIRE dropouts and correspond to our SD850_UDS_T1_A36 and A42, respectively.

6. RADIO PROPERTIES

It is well known that FIR galaxies dominated by dust-embedded star formation follow a tight FIR-radio relation (see [Condon 1992](#), for review). The corollary is that their observed spectral indices between FIR/sub-mm and radio wavelengths should be a strong function of redshift due to the opposing K-corrections in these two regimes (see e.g. [Carilli & Yun 1999](#)). As a result, high-redshift dusty star forming galaxies in general should be radio weak unless they also host an active galactic nucleus (AGN). Therefore, we examine the radio properties of our candidates whenever sufficiently deep radio data are available. We first examine them against the public data from the Faint Images of the Radio Sky at Twenty-cm (FIRST; [Becker et al. 1995](#)), which covered over 10,000 deg^2 of the Galactic Caps at 1.4 GHz to the typical sensitivity of $\text{rms} \sim 0.15 \text{ mJy beam}^{-1}$. Some of our fields have deeper radio data, which we subsequently examine as well. While in most cases they only cover a fraction of the area, these are valuable in further selecting the most promising high-redshift candidates.

6.1. Radio Properties of 500 μm risers

In determining the matching radius to the radio sources, we consider the positional errors due to both the SPIRE and the radio beams ($\sigma_{\text{pos}}^{\text{SPIRE}}$ and $\sigma_{\text{pos}}^{\text{radio}}$, respectively), which are calculated based on Equation 2 and then are added in quadrature to obtain the total error $\sigma_{\text{pos}} = \sqrt{(\sigma_{\text{pos}}^{\text{SPIRE}})^2 + (\sigma_{\text{pos}}^{\text{radio}})^2}$. In most cases, the former is the dominant term. For the xID-based and the residual-based objects, we use $\theta = 18''$ and $36''$ in Equation 2, which are the 250 and the 500 μm beam sizes, respectively. We take this approach because the positions of these two sets are based on the 250 and the 500 μm maps, respectively. For reference, these correspond to $\sigma_{\text{pos}}^{\text{SPIRE}} = 3.''05$ and $6.''11$, respectively, at $S/N = 5$. For different objects, $\sigma_{\text{pos}}^{\text{SPIRE}}$ vary because of their different S/N s in SPIRE. As the radio positional error is usually much smaller, we do not consider the radio source S/N individually but calculate at the fixed $S/N = 5$. To simplify the matching process, we search for the radio counterparts within a generous matching radius of $r = 10''$, calculate the positional offsets, Δ_{pos} ,

between our objects and the matched radio sources, and determine the ratios Δ/σ between Δ_{pos} and σ_{pos} . The matches with $\Delta/\sigma \leq 1.5$ are deemed to be reliable and are listed in Table 5 and 7. The unmatched ones are indicated as such in Table 13, and we quote their upper limits based on the relevant radio catalogs. We discuss both the matched and the unmatched sources below in some detail.

6.1.1. Cross-matching with the FIRST sources

All of our equatorial and northern fields are covered by FIRST, which, albeit being shallow, is useful in detecting the most obvious radio AGNs. The angular resolution of FIRST is $5''$, and therefore $\sigma_{\text{pos}}^{\text{radio}} = 0.''85$.

As it turns out, none of our objects in COSMOS, EGS, ELAISN1, and GOODS-N have FIRST matches within $10''$. In the other four equatorial and northern fields, we have seven matches with $\Delta/\sigma \leq 1.5$, which are summarized in the top part of Table 5. Four of these radio counterparts have monotonically increasing SED from FIR to radio, suggesting that they are likely blazars (see Ma & Yan 2015, Section 4.7). 500R_ELAIN2.T1.x03 and 500R_LH.T1.x003 are indeed listed as blazars in the Fermi Large Area Telescope AGN catalog (Ackermann et al. 2015). The former one is associated with SDSS J163915.80+412833.7 at $z = 0.69$ (Schneider et al. 2010). 500R_FLS.T1.x07 is also listed as a blazar by Marchã & Caccianiga (2013) and Mingaliev et al. (2014), and has the known redshift of $z = 0.2974$ (Marleau et al. 2007). Finally, 500R_LH.T1.x039 is also likely a blazar and has $z = 0.5795$ based on the SDSS DR13. Therefore, the contamination of the 500 μm riser sample due to blazars is only $\sim 1.0\%$ (4 out of the 381 total in the northern and equatorial fields). The other three objects have $S_{1.4} > 1$ mJy and must host strong AGNs.

Table 5 summarizes the above results.

6.1.2. Cross-matching with deeper radio data

All our fields have partial radio data deeper than FIRST, which we further use for the radio counterpart identification. Unfortunately, most of the radio images are not publicly available, and hence our discussion below is based on the catalogs published by the respective authors. Table 6 summarizes the matching results, and the details are provided below for each field.

— *ADFS* Currently, the only deep radio data in this field are those of White et al. (2012), which were obtained at 1.4 GHz using the Australia Telescope Compact Array (ATCA). The beam size is $6.''2 \times 4.''9$, which corresponds to $\sigma_{\text{pos}}^{\text{ATCA}} = 0.''95$. Ten of our objects are within the coverage, and only one (500R_ADFS.T1.x14) is matched within $10''$. However, it has $\Delta/\sigma = 1.7$ and is not regarded as a real match.

The sensitivity of this radio map varies greatly from the field center (1σ sensitivity, or rms, of $18\text{--}50\ \mu\text{Jy beam}^{-1}$) to the edge ($\sim 200\ \mu\text{Jy beam}^{-1}$). We cannot obtain the brightness upper limit that is close to the real sensitivity limit at the location of each nondetection because we do not have the map at hand. We choose to assign a universal, conservative upper limit of

1 mJy to all these nondetections, which corresponds to $\sim 5\sigma$ noise at the field edge.

— *CDFS* There have been two 1.4 GHz surveys in this field, which are described in Miller et al. (2013) and Franzen et al. (2015), respectively. The data from the former were obtained at the Very Large Array (VLA) and have reached the rms of $7.4\ \mu\text{Jy beam}^{-1}$ over $0.324\ \text{deg}^2$ with the beam size of $2.''8 \times 1.''6$. Miller et al. (2013) provide a catalog that includes only the objects above 5σ , which corresponds to $37.0\ \mu\text{Jy}$. The data from the latter were obtained at the Australia Telescope, which have reached the rms of $14\ \mu\text{Jy beam}^{-1}$ over $3.6\ \text{deg}^2$ with the beam size of $16'' \times 7''$. The catalog also only includes the objects above 5σ ($\gtrsim 70\ \mu\text{Jy}$). Their positional uncertainties contributing to the total positional errors are therefore $\sigma_{\text{pos}}^{\text{VLA}} = 0.''39$ and $\sigma_{\text{pos}}^{\text{AT}} = 2.''10$, respectively.

Two of our objects are within the coverage of Miller et al. (2013), but neither has a counterpart in their catalog. We assign them the 5σ upper limit of $37\ \mu\text{Jy}$.

There are 32 additional objects that fall within the coverage of Franzen et al. (2015), and 8 of them are matched with counterparts in their catalog. In particular, 500R_CDFS.T1.x004 has $S_{1.4} = 10.86 \pm 0.56$ mJy, which indicates that its radio emission is most likely powered by AGN. The next brightest, x183, has $S_{1.4} = 0.95 \pm 0.06$ mJy, is a borderline case. The other six objects are likely star formation dominated. For the 24 objects that are not matched, we assign them the 5σ upper limit of $70\ \mu\text{Jy}$.

— *COSMOS* This field has the best radio data among all, especially those obtained at the VLA. The 1.4 GHz source catalogs are presented in Schinnerer et al. (2007, 2010). A deeper radio map at 3 GHz has been obtained by Smolčić et al. (2017), which covers $2\ \text{deg}^2$ to rms of $2.3\ \mu\text{Jy beam}^{-1}$ at the resolution of $0.''75$ (corresponding to $\sigma_{\text{pos}}^{\text{VLA3GHz}} = 0.''13$). The source catalog includes 10,830 sources above 5σ ($\gtrsim 11.5\ \mu\text{Jy}$). Here we only use the 3 GHz data because they are deeper and also cover a wider area than the 1.4 GHz data.

There are 17 of our objects falling within the 3 GHz coverage, among which 10 have counterparts with $\Delta/\sigma \leq 1.5$. All of these counterparts have $S_{3.0} < 100\ \mu\text{Jy}$, with the faintest having $13\ \mu\text{Jy}$. It is highly likely that their radio fluxes are powered by star formation. The other seven objects are not matched (three of them have radio sources within $10''$ but have $\Delta/\sigma > 1.5$), for which we assign the 5σ $S_{3.0}$ upper limit of $11.5\ \mu\text{Jy}$. Assuming a power-law SED of $S_\nu \sim \nu^{-0.8}$, this corresponds to $S_{1.4}$ upper limit of $21.2\ \mu\text{Jy}$.

— *EGS* The deepest public radio data in this field are those from the VLA 1.4 GHz survey of Ivison et al. (2007a), which have reached rms of $\sim 26\ \mu\text{Jy beam}^{-1}$ over $0.73\ \text{deg}^2$ with the beam size of $\sim 3.''8$ (corresponding to $\sigma_{\text{pos}}^{\text{VLA}} = 0.''66$). Eight of our objects are within the coverage, and only two of them are matched with counterparts in their catalog. They both have $S_{1.4} < 100\ \mu\text{Jy}$ and are likely star formation dominated. For the six unmatched, we assign a universal 5σ upper

Table 5. Match of Tier 1 500 μm risers to FIRST

Object Name	σ_{pos} ($''$)	Δ_{pos} ($''$)	Δ/σ	RA_F	DEC_F	$S_{1.4}$ (mJy)	$\sigma_{1.4}$ (mJy beam $^{-1}$)	Comments
500R_ELAIN2_T1_x03	1.9	2.6	1.4	16:39:15.813	+41:28:33.61	91.76	0.161	blazar ^a ; $z = 0.69$ ^b
500R_ELAIN2_T1_x49	3.5	1.7	0.5	16:36:46.387	+40:14:36.67	7.25	0.143	...
500R_FLS_T1_x07	2.4	0.8	0.3	17:25:35.004	+58:51:39.92	71.06	0.147	blazar ^c , ^d ; $z = 0.2874$ ^e
500R_FLS_T1_x50	4.4	6.0	1.4	17:23:15.537	+59:09:18.93	1.13	0.143	...
500R_LH_T1_x003	1.4	0.6	0.4	10:37:44.322	+57:11:55.57	130.02	0.147	blazar ^a
500R_LH_T1_x039	2.3	1.4	0.6	10:40:37.806	+55:40:52.73	61.39	0.144	likely blazar; $z = 0.5795$ ^f
500R_XMMLSS_T1_x83	4.7	4.6	1.0	02:19:19.156	−06:45:54.16	1.77	0.143	...
500R_FLS_T1_x36	3.4	9.1	2.7	17:06:42.635	+60:37:57.43	3.59	0.331	...
500R_FLS_T1_x03	2.4	7.5	3.1	17:08:52.043	+58:48:56.87	1.67	0.137	...
500R_FLS_T1_R11	5.2	9.5	1.8	17:11:31.799	+59:39:24.99	14.22	0.149	...
500R_LH_T1_R06	4.0	8.8	2.2	11:00:48.619	+59:20:09.32	9.49	0.155	...

NOTE—Tier 1 500 μm risers matched to the radio sources in the FIRST catalog. The matching radius is $r = 10''$. σ_{pos} is the total positional error due to the uncertainties of the SPIRE and the FIRST data. Δ_{pos} is the separation between the SPIRE and the FIRST positions. Δ/σ is the ratio of the two, and only the top seven matches with $\Delta/\sigma \leq 1.5$ are deemed to be reliable. The bottom four are listed for reference. The equatorial coordinates (J2000.0) are the FIRST positions. $S_{1.4}$ and $\sigma_{1.4}$ are the integrated flux density and the RMS sensitivity taken from the FIRST catalog, respectively. The references for the blazar identifications and the redshifts are (a) Ackermann et al. (2015), (b) Schneider et al. (2010), (c) Marchã & Caccianiga (2013), (d) Mingaliev et al. (2014), (e) Marleau et al. (2007), and (f) SDSS DR13.

Table 6. Summary of matching Tier 1 500 μm risers to deep radio data

Field	Facility	Area (deg 2)	Beam Size ($''$)	$\sigma_{\text{pos}}^{\text{Radio}}$ ($''$)	Sensitivity (μJy)	Obj Coverage	Obj Matched
ADFS	ATCA, 1.4 GHz	2.5	6.2×4.9	0.95	18–200	10/40	0
CDFS	VLA, 1.4 GHz	0.324	2.8×1.6	0.39	37.0	2/140	0
	AT, 1.4 GHz	3.6	16×7	2.10	70	32/140	8
COSMOS	VLA, 3.0 GHz	2	0.75	0.13	11.5	17/25	10
EGS	VLA, 1.4 GHz	0.73	3.8	0.66	130	8/26	2
ELAISN1	GMRT, 610 MHz	9	6×5	0.94	350	35/51	0
ELAISN2	GMRT, 610 MHz	6	6.5×5	0.98	425	31/39	2
ELAISS1	AT, 1.4 GHz	2.7	16×7	2.10	75	16/68	0
FLS	VLA, 1.4 GHz	5	5	0.86	115	27/41	6
GOODS-N	VLA, 1.4 GHz	0.44	1.7	0.29	20	4/6	1
LH	GMRT, 610 MHz	13	6×5	0.94	300	89/141	3
XMM-LSS	VLA, 1.4 GHz	0.8	5×4	0.77	100	1/52	0

NOTE—The values of $\sigma_{\text{pos}}^{\text{Radio}}$ are calculated based on Equation 2 and $S/N = 5$. The sensitivity levels are based on the source catalogs that we used, and in most cases correspond to $S/N = 5$ (see §6.1.2 for details). For the data that are not obtained at 1.4 GHz, the conversion to 1.4 GHz for the quoted sensitivity levels can be done by assuming a power law SED of $S_\nu \sim \nu^{-0.8}$. The number pairs under “Obj Coverage” are those of the objects in the areas covered by the relevant radio data and the total in the Tier 1 samples, respectively, while the numbers under “Obj Matched” are those of the objects detected above the quoted sensitivity levels.

limit of 130 μJy , which are all in the star-formation-dominated regime.

— *ELAISN1* The only radio resources appropriate here are the data taken by the Giant Meterwave Radio Telescope (GMRT) at 610 MHz Garn et al. (2008a), which cover $\sim 9 \text{ deg}^2$ to an rms of $\sim 40\text{--}70 \mu\text{Jy beam}^{-1}$ with the beam size of $6'' \times 5''$ (corresponding to $\sigma_{\text{pos}}^{\text{GMRT}} = 0.''94$). The source catalog includes the objects with 610 MHz flux density $S_{610} > 0.14 \text{ mJy}$.

Thirty-five of our objects are covered by this radio map, but none of them are matched with counterparts in the aforementioned 610 MHz catalog. We opt to assign

a rather conservative upper limit of 0.35 mJy (about 5σ in the less sensitive region of the map) to these sources. Assuming a power-law SED of $S_\nu \sim \nu^{-0.8}$, this corresponds to $S_{1.4} < 0.18 \text{ mJy}$, which is still in the sub-millijansky regime and thus the sources are likely star formation dominated.

— *ELAISN2* The only appropriate radio data in this field are also obtained by the GMRT at 610 MHz Garn et al. (2009), which cover $\sim 6 \text{ deg}^2$ to rms $\sim 85 \mu\text{Jy beam}^{-1}$ with the beam size of $6.''5 \times 5''$ (corresponding to $\sigma_{\text{pos}}^{\text{GMRT}} = 0.''98$). The source catalog includes the objects with $S_{610} > 0.3 \text{ mJy}$.

Table 7. Match of Tier 1 500 μm risers to deep radio data

Object Name	σ_{pos} ($''$)	Δ_{pos} ($''$)	Δ/σ	f_{500} (mJy)	RA _{radio}	DEC _{radio}	S_{radio} (μJy)	HizIdx (500)	References
500R_CDFS_T1.x004	2.4	3.1	1.3	60.0 ± 3.9	3:30:55.67	-28:48:55.16	10863 ± 558	0.01	(a)
500R_CDFS_T1.x023	2.8	1.4	0.5	41.1 ± 3.9	3:30:25.84	-27:38:10.41	161 ± 25	0.26	(a)
500R_CDFS_T1.x104	3.5	4.7	1.3	26.0 ± 3.9	3:33:35.54	-28:41:32.72	286 ± 22	0.09	(a)
500R_CDFS_T1.x107	3.0	1.2	0.4	36.0 ± 3.9	3:29:35.25	-27:39:23.39	106 ± 18	0.34	(a)
500R_CDFS_T1.x183	3.9	4.7	1.2	26.0 ± 3.9	3:26:37.13	-28:46:11.38	945 ± 61	0.03	(a)
500R_CDFS_T1.x187	3.7	2.4	0.6	22.0 ± 4.0	3:30:34.00	-27:39:43.26	129 ± 24	0.17	(a)
500R_CDFS_T1.x193	3.4	2.7	0.8	21.9 ± 3.9	3:26:44.36	-28:10:52.01	159 ± 24	0.14	(a)
500R_CDFS_T1.x282	5.0	1.4	0.3	24.7 ± 3.9	3:29:22.71	-27:21:53.06	548 ± 41	0.05	(a)
500R_COSMOS_T1.x01	2.9	2.5	0.9	26.2 ± 5.1	9:59:21.57	1:47:37.45	25.5 ± 2.6	0.56	(b)
500R_COSMOS_T1.x05	2.2	1.6	0.7	27.4 ± 5.0	10:01:38.55	2:37:36.71	29.1 ± 2.8	0.51	(b)
500R_COSMOS_T1.x07	2.5	2.9	1.2	27.9 ± 5.2	10:03:01.79	1:39:10.52	35.8 ± 3.5	0.42	(b)
500R_COSMOS_T1.x08	2.2	0.3	0.1	28.1 ± 5.0	10:01:42.20	2:37:27.10	18.7 ± 2.4	0.82*	(b)
500R_COSMOS_T1.x13	2.2	1.2	0.5	28.6 ± 5.1	9:58:45.94	2:43:29.27	56.1 ± 3.6	0.28	(b)
500R_COSMOS_T1.x23	2.1	2.5	1.2	31.1 ± 5.2	10:01:57.69	1:44:46.97	89.8 ± 5.0	0.19	(b)
500R_COSMOS_T1.x24	2.7	4.0	1.5	31.4 ± 5.2	10:02:40.43	1:45:44.11	12.7 ± 2.4	1.34*	(b)
500R_COSMOS_T1.x25	3.8	2.5	0.7	31.4 ± 5.3	10:00:17.35	1:58:27.82	46.4 ± 3.2	0.37	(b)
500R_COSMOS_T1.x26	3.9	4.0	1.0	32.2 ± 5.1	10:00:59.18	1:33:06.73	24.3 ± 3.8	0.72*	(b)
500R_COSMOS_T1.x31	2.6	1.5	0.6	36.0 ± 5.2	10:01:26.02	1:57:51.32	24.1 ± 2.6	0.81*	(b)
500R_EGS_T1.x10	2.1	0.8	0.4	44.0 ± 4.3	14:22:33.33	53:14:18.95	67 ± 12	0.65	(c)
500R_EGS_T1.x27	3.6	1.9	0.5	22.0 ± 4.4	14:24:01.70	53:23:19.47	611 ± 13	0.04	(c)
500R_FLS_T1.x11	3.1	1.8	0.6	35.0 ± 5.8	17:18:51.84	59:54:03.84	148 ± 25	0.24	(d)
500R_FLS_T1.x28	3.2	3.3	1.0	34.7 ± 6.9	17:14:40.46	58:20:35.02	135 ± 26	0.26	(d)
500R_FLS_T1.x30	3.6	3.8	1.1	41.6 ± 5.8	17:18:39.95	58:20:37.13	129 ± 22	0.32	(d)
500R_GOODSN_T1.x20	3.0	4.4	1.5	18.9 ± 3.4	12:35:09.43	62:11:13.40	41.4 ± 7.7	0.46	(e)
500R_LH_T1.x204	3.1	0.8	0.3	37.1 ± 4.7	10:50:31.14	56:30:45.9	1134 ± 121	0.03	(f)
500R_LH_T1.x262	4.6	3.2	0.7	27.5 ± 4.5	10:42:50.88	57:31:19.7	518 ± 78	0.05	(f)
500R_ADFS_T1.x14	2.9	4.8	1.7	29.4 ± 5.6	4:46:58.70	-53:23:29.90	304 ± 38	...	(g)
500R_COSMOS_T1.x02	2.8	6.1	2.2	26.4 ± 5.0	10:01:42.55	2:00:14.69	109.0 ± 6.3	...	(c)
500R_COSMOS_T1.x10	2.2	4.2	1.9	28.3 ± 5.2	10:01:40.44	2:30:10.44	11.6 ± 2.3	...	(c)
500R_COSMOS_T1.x34	1.7	6.0	3.5	39.8 ± 5.1	10:00:09.49	2:22:19.48	142.0 ± 7.5	...	(c)
500R_GOODSN_T1.x01	1.1	1.9	1.7	43.5 ± 3.5	12:39:05.94	62:05:36.40	72.9 ± 14.0	...	(e)

NOTE—Tier 1 500 μm risers matched to the radio sources in various surveys that are deeper than FIRST. The matching radius is $r = 10''$. Only the top 26 matches that have $\Delta/\sigma \leq 1.5$ are deemed to be reliable. “HizIdx(500)” is calculated based on Equation 3. Those that with HizIdx(500) ≥ 0.7 (potentially at $z > 6$; see §6.4.1) are boldfaced and marked with asterisk. The bottom five objects only have lower limits of HizIdx (reported in Table 8) because they are treated as having no radio counterparts and thus only have upper limits of their radio flux densities. The radio catalogs are from the references listed in the last column. These are (a) [Franzen et al. \(2015\)](#), 1.4 GHz; (b) [Smolčić et al. \(2017\)](#), 3 GHz; (c) [Iverson et al. \(2007a\)](#), 1.4 GHz; (d) [Condon et al. \(2003\)](#), 1.4 GHz; (e) [Morrison et al. \(2010\)](#), 1.4 GHz; (f) [Garn et al. \(2008b, 2010\)](#), 610 MHz; (g) [White et al. \(2012\)](#), 1.4 GHz.

Thirty-one of our objects are within the coverage of this radio map. Two of them are matched with counterparts, and both are FIRST sources as already discussed above. For the other 29 objects, we assign a conservative upper limit of 0.425 mJy (corresponding to $S_{1.4} < 0.22$ mJy when assuming $S_\nu \sim \nu^{-0.8}$). Similar to the discussion above, these objects are likely star formation dominated in radio.

— *ELAISS1* This field has 1.4 GHz data from the Australia Telescope as described in [Franzen et al. \(2015\)](#), which cover 2.7 deg^2 to $17 \mu\text{Jy beam}^{-1}$ with the beam size of $16'' \times 7''$ (corresponding to $\sigma_{\text{pos}}^{\text{AT}} = 2.''10$). The public source catalog includes the sources that are above 5σ . Sixteen of our objects are within the coverage; however, none of them are matched with counterparts. We therefore assign them the 5σ upper limit of $75 \mu\text{Jy}$.

— *FLS* About 5 deg^2 of this field have 1.4 GHz data obtained by the VLA to rms $\sim 23 \mu\text{Jy beam}^{-1}$ with the beam size of $5''$ (corresponding to $\sigma_{\text{pos}}^{\text{VLA}} = 0.''86$). These

are described in [Condon et al. \(2003\)](#), who also present a catalog that includes the sources above 5σ . Their 1.4 GHz map covers 27 of our objects, among which 6 are matched in the radio catalog within $10''$. Three of them have already been discussed in the match to the FIRST sources: 500R_FLS_T1.x07 and x50 have reliable FIRST counterparts, while R11 does not. The match to R11 in this catalog also has $\Delta/\sigma > 1.5$ (it is the same radio source as in the FIRST catalog) and therefore is not a reliable counterpart. The other three new matches here are all reliable ones and are likely dominated by star formation. For the 21 unmatched objects, we assign the 5σ upper limit of $115 \mu\text{Jy}$.

— *GOODS-N* This field has deep VLA 1.4 GHz data as described in [Morrison et al. \(2010\)](#), who cover its central $40' \times 40'$ area, with the beam size of $\sim 1.''7$ (corresponding to $\sigma_{\text{pos}}^{\text{VLA}} = 0.''29$). The data have reached an rms noise of $\sim 3.9 \mu\text{Jy beam}^{-1}$ near the center and $\sim 8 \mu\text{Jy beam}^{-1}$ at $15'$ from the center. The catalog

of Morrison et al. (2010) include sources stronger than 20 μ Jy.

Four of our objects are in the radio coverage. Two are matched within 10'', among which only one is reliable and is likely dominated by star formation. For those that are not matched (including the one without a reliable match), we assign an upper limit of 20 μ Jy.

– *LH* While this field has a number of deep radio surveys (see, e.g., Ibar et al. 2009; Owen & Morrison 2008; Owen et al. 2009; Vernstrom et al. 2016) within limited areas, unfortunately none of our objects fall within their coverages. The medium-deep GMRT 610 MHz surveys of Garn et al. (2008b, 2010) offer the only radio maps that cover most of the field (and thus most of our objects) to a sensitivity level that is significantly deeper than FIRST. The combined 610 MHz map extends ~ 13 deg² to rms ~ 80 μ Jy beam⁻¹ with the beam size of 6'' \times 5'' (corresponding to $\sigma_{\text{pos}}^{\text{GMRT}} = 0.''94$). The central ~ 5 deg² region has reached a slightly deeper sensitivity of rms ~ 60 μ Jy beam⁻¹ (Garn et al. 2008b). The catalogs presented in these two papers, which are extracted independently, include the sources above $S_{610} > 0.2$ mJy. For the matching here, we merge the two catalogs into one that contains unique sources.

In total, 89 of our objects falling within this 610 MHz map. Only three of them are matched within 10'' and are all reliable matches. One of them (500R_LH.T1.x003) is a FIRST source already mentioned above. The other two have $S_{610} = 1.13 \pm 0.12$ and 0.546 ± 0.08 mJy, respectively. If assuming a power-law SED of $S(\nu) \sim \nu^{-0.8}$ they would have $S_{1.4} = 0.58$ and 0.28 mJy, respectively, which would be in the AGN-dominated regime. We assign a conservative S_{610} upper limit of 0.3 mJy to the 86 unmatched objects, which would be in the sub-millijansky regime at 1.4 GHz ($S_{1.4} < 0.15$ mJy) and hence are likely star formation dominated.

– *XMM-LSS* This field has VLA 1.4 GHz data covering ~ 1.3 deg² as described in Simpson et al. (2006). However, their source catalog only covers 0.8 deg² and includes the objects that have $S_{1.4} > 100$ μ Jy. The beam size is 5'' \times 4'' (corresponding to $\sigma_{\text{pos}}^{\text{VLA}} = 0.''77$). Only one of our objects is within the coverage, and it is not matched with a counterpart. We assign an upper limit of 100 μ Jy, which is in the star formation dominated regime.

The above results are detailed in Tables 7 and 8 for the radio detections and nondetections, respectively.

Table 8. Tier 1 500 μ m risers undetected in radio

ID	f_{500}	S_{radio}	HizIdx	ID	f_{500}	S_{radio}	HizIdx	ID	f_{500}	S_{radio}	HizIdx
	(mJy)	(μ Jy)	(500)		(mJy)	(μ Jy)	(500)		(mJy)	(μ Jy)	(500)
500R_ADFS.T1.x03	56.5 \pm 6.0	< 1000	> 0.06	x28	34.0 \pm 5.8	< 1000	> 0.03	R20	33.8 \pm 5.5	< 1000	> 0.03
x14	29.6 \pm 5.6	< 1000	> 0.03	x41	37.1 \pm 5.4	< 1000	> 0.04	R34	28.3 \pm 5.5	< 1000	> 0.03
x18	37.9 \pm 5.5	< 1000	> 0.04	R05	42.0 \pm 5.5	< 1000	> 0.04				
x20	37.1 \pm 5.7	< 1000	> 0.04	R14	35.3 \pm 5.5	< 1000	> 0.04				
500R_CDFS.T1.x007	45.4 \pm 3.9	< 70	> 0.65	x124	33.5 \pm 4.1	< 70	> 0.48	x211	31.1 \pm 3.9	< 70	> 0.44
x015	56.2 \pm 3.9	< 70	> 0.80*	x134	22.7 \pm 3.9	< 70	> 0.32	x240	23.9 \pm 4.0	< 70	> 0.34
x034	44.7 \pm 4.3	< 70	> 0.64	x166	22.3 \pm 4.2	< 70	> 0.32	x246	36.6 \pm 4.6	< 70	> 0.52
x037	36.2 \pm 5.4	< 70	> 0.52	x170	20.9 \pm 4.1	< 70	> 0.30	x268	21.4 \pm 4.0	< 70	> 0.31
x038	37.7 \pm 4.0	< 70	> 0.54	x176	27.2 \pm 3.9	< 70	> 0.39	x284	32.1 \pm 4.0	< 70	> 0.46
x048	27.9 \pm 4.2	< 37	> 0.75*	x178	30.2 \pm 4.0	< 70	> 0.43	R14	26.8 \pm 3.9	< 70	> 0.38
x058	25.9 \pm 4.2	< 70	> 0.37	x180	28.9 \pm 4.8	< 70	> 0.41	R27	22.8 \pm 4.0	< 70	> 0.33
x118	27.9 \pm 3.9	< 70	> 0.40	x189	29.1 \pm 4.0	< 70	> 0.42	R32	22.0 \pm 4.0	< 70	> 0.31
x119	25.8 \pm 4.2	< 70	> 0.37	x190	28.6 \pm 4.0	< 37	> 0.77*				
500R_COSMOS.T1.x02	26.4 \pm 5.0	< 11.5	> 1.25*	x16	28.9 \pm 5.0	< 11.5	> 1.37*	x35	41.0 \pm 5.0	< 11.5	> 1.94*
x04	27.2 \pm 5.1	< 11.5	> 1.29*	x21	30.8 \pm 5.0	< 11.5	> 1.45*				
x10	28.3 \pm 5.2	< 11.5	> 1.34*	x34	39.8 \pm 5.1	< 11.5	> 1.87*				
500R_EGS.T1.x08	33.0 \pm 4.4	< 130	> 0.25	x36	29.1 \pm 4.3	< 130	> 0.22	x45	23.3 \pm 4.3	< 130	> 0.18
x09	25.0 \pm 4.6	< 130	> 0.19	x42	27.1 \pm 4.5	< 130	> 0.21	x46	24.0 \pm 4.8	< 130	> 0.18
500R_ELAIN1.T1.x001	170.7 \pm 5.1	< 350	> 0.95*	x044	35.0 \pm 5.0	< 350	> 0.19	x075	38.9 \pm 5.1	< 350	> 0.22
x003	51.1 \pm 5.3	< 350	> 0.28	x045	39.5 \pm 5.2	< 350	> 0.22	x078	40.0 \pm 5.8	< 350	> 0.22
x004	55.2 \pm 4.9	< 350	> 0.31	x053	28.4 \pm 5.0	< 350	> 0.16	x079	36.0 \pm 5.1	< 350	> 0.20
x008	55.2 \pm 4.9	< 350	> 0.31	x054	48.9 \pm 5.0	< 350	> 0.27	x081	29.8 \pm 5.2	< 350	> 0.17
x009	43.1 \pm 5.0	< 350	> 0.24	x056	28.9 \pm 5.1	< 350	> 0.16	x082	28.2 \pm 5.2	< 350	> 0.16
x012	31.1 \pm 5.1	< 350	> 0.17	x057	27.6 \pm 5.2	< 350	> 0.15	x083	29.3 \pm 5.0	< 350	> 0.16
x025	36.9 \pm 5.7	< 350	> 0.21	x060	33.8 \pm 5.2	< 350	> 0.19	x087	27.9 \pm 5.5	< 350	> 0.16
x026	37.6 \pm 5.0	< 350	> 0.21	x061	40.8 \pm 5.2	< 350	> 0.23	x091	28.6 \pm 5.3	< 350	> 0.16
x028	27.4 \pm 5.0	< 350	> 0.15	x062	32.9 \pm 5.1	< 350	> 0.18	x093	34.0 \pm 4.9	< 350	> 0.19

Table 8 continued

Table 8 (*continued*)

ID	f_{500}	S_{radio}	HizIdx	ID	f_{500}	S_{radio}	HizIdx	ID	f_{500}	S_{radio}	HizIdx
	(mJy)	(μJy)	(500)		(mJy)	(μJy)	(500)		(mJy)	(μJy)	(500)
x031	32.6 ± 4.9	< 350	> 0.18	x064	35.7 ± 5.9	< 350	> 0.20	x099	25.3 ± 4.9	< 350	> 0.14
x033	36.5 ± 5.5	< 350	> 0.20	x068	28.0 ± 5.0	< 350	> 0.16	x103	25.9 ± 5.0	< 350	> 0.14
x038	35.8 ± 4.9	< 350	> 0.20	x070	40.9 ± 5.2	< 350	> 0.23				
500R_ELAISN2_T1_x02	65.8 ± 6.1	< 425	> 0.30	x27	45.0 ± 5.9	< 425	> 0.21	R05	46.9 ± 5.8	< 425	> 0.21
x04	52.5 ± 5.9	< 425	> 0.24	x28	33.6 ± 6.4	< 425	> 0.15	R06	44.7 ± 6.0	< 425	> 0.20
x07	48.8 ± 5.9	< 425	> 0.22	x30	33.4 ± 6.0	< 425	> 0.15	R07	43.3 ± 5.9	< 425	> 0.20
x08	48.3 ± 6.2	< 425	> 0.22	x31	35.0 ± 6.2	< 425	> 0.16	R08	43.0 ± 5.9	< 425	> 0.20
x09	42.7 ± 6.2	< 425	> 0.20	x33	35.8 ± 6.1	< 425	> 0.16	R15	37.3 ± 5.8	< 425	> 0.17
x12	44.4 ± 6.0	< 425	> 0.20	x36	53.8 ± 7.1	< 425	> 0.25	R17	35.0 ± 5.9	< 425	> 0.16
x18	31.2 ± 6.0	< 425	> 0.14	x38	34.9 ± 5.9	< 425	> 0.16	R27	31.4 ± 5.9	< 425	> 0.14
x19	38.2 ± 6.0	< 425	> 0.17	x43	32.8 ± 6.0	< 425	> 0.15	R28	29.8 ± 5.8	< 425	> 0.14
x20	38.2 ± 5.9	< 425	> 0.17	x45	31.4 ± 6.0	< 425	> 0.14	R29	29.6 ± 5.9	< 425	> 0.14
x24	32.6 ± 5.9	< 425	> 0.15	x51	34.1 ± 6.4	< 425	> 0.16				
500R_ELAISS1_T1_x02	44.8 ± 4.8	< 75	> 0.60	x47	32.0 ± 4.7	< 75	> 0.43	x84	25.9 ± 4.6	< 75	> 0.35
x18	53.3 ± 4.7	< 75	$> 0.71^*$	x55	26.6 ± 4.7	< 75	> 0.35	x85	25.4 ± 4.7	< 75	> 0.34
x26	37.2 ± 5.0	< 75	> 0.50	x61	24.0 ± 4.7	< 75	> 0.32	R16	29.0 ± 4.6	< 75	> 0.39
x37	26.6 ± 4.9	< 75	> 0.35	x71	25.2 ± 4.7	< 75	> 0.34	R26	25.8 ± 5.1	< 75	> 0.34
x45	28.2 ± 4.7	< 75	> 0.38	x72	35.3 ± 4.8	< 75	> 0.47				
x46	25.0 ± 4.8	< 75	> 0.33	x76	28.1 ± 5.0	< 75	> 0.37				
500R_FLS_T1_x02	41.0 ± 5.9	< 150	> 0.27	x23	33.2 ± 6.1	< 150	> 0.22	R01	51.0 ± 5.8	< 150	> 0.34
x09	48.7 ± 5.8	< 150	> 0.32	x29	32.8 ± 6.0	< 150	> 0.22	R02	46.5 ± 5.8	< 150	> 0.31
x12	33.7 ± 5.8	< 150	> 0.22	x31	64.4 ± 5.8	< 150	> 0.43	R05	39.9 ± 5.8	< 150	> 0.27
x15	41.9 ± 5.8	< 150	> 0.28	x32	32.5 ± 5.8	< 150	> 0.22	R07	38.6 ± 5.8	< 150	> 0.26
x16	38.2 ± 5.9	< 150	> 0.25	x33	30.2 ± 5.8	< 150	> 0.20	R10	36.1 ± 5.8	< 150	> 0.24
x18	45.0 ± 5.9	< 150	> 0.30	x37	34.8 ± 5.8	< 150	> 0.23	R13	32.5 ± 5.8	< 150	> 0.22
x21	47.2 ± 5.9	< 150	> 0.31	x46	33.8 ± 6.6	< 150	> 0.23	R16	29.1 ± 5.8	< 150	> 0.19
500R_GOODSN_T1_x01	43.5 ± 3.5	< 20.0	$> 2.18^*$	x03	29.2 ± 3.4	< 20.0	$> 1.46^*$	x09	24.1 ± 3.4	< 20.0	$> 1.20^*$
500R_LH_T1_x001	137.5 ± 4.5	< 300	> 0.46	x126	30.9 ± 4.5	< 300	> 0.10	x230	30.3 ± 4.6	< 300	> 0.10
x002	75.2 ± 0.0	< 300	> 0.25	x127	32.8 ± 4.6	< 300	> 0.11	x233	35.6 ± 4.6	< 300	> 0.12
x005	70.8 ± 4.8	< 300	> 0.24	x136	24.7 ± 4.6	< 300	> 0.08	x235	26.1 ± 5.2	< 300	> 0.09
x012	50.2 ± 4.6	< 300	> 0.17	x137	29.1 ± 4.7	< 300	> 0.10	x238	25.3 ± 4.5	< 300	> 0.08
x019	43.4 ± 5.3	< 300	> 0.14	x138	38.3 ± 4.5	< 300	> 0.13	x239	23.2 ± 4.5	< 300	> 0.08
x038	42.0 ± 4.7	< 300	> 0.14	x154	25.0 ± 4.6	< 300	> 0.08	x240	24.8 ± 4.8	< 300	> 0.08
x041	31.4 ± 4.6	< 300	> 0.10	x155	22.6 ± 4.5	< 300	> 0.08	x245	30.5 ± 4.6	< 300	> 0.10
x056	45.1 ± 4.5	< 300	> 0.15	x162	29.9 ± 4.7	< 300	> 0.10	x248	31.5 ± 4.7	< 300	> 0.11
x057	36.2 ± 5.6	< 300	> 0.12	x170	27.3 ± 4.5	< 300	> 0.09	x249	30.7 ± 4.9	< 300	> 0.10
x058	34.8 ± 4.5	< 300	> 0.12	x172	29.1 ± 4.6	< 300	> 0.10	x252	26.1 ± 4.7	< 300	> 0.09
x062	29.9 ± 4.6	< 300	> 0.10	x173	32.4 ± 5.2	< 300	> 0.11	R11	46.6 ± 4.6	< 300	> 0.16
x063	27.5 ± 4.7	< 300	> 0.09	x174	25.6 ± 4.9	< 300	> 0.09	R13	46.3 ± 5.9	< 300	> 0.15
x067	34.8 ± 4.8	< 300	> 0.12	x179	25.5 ± 4.8	< 300	> 0.09	R22	37.3 ± 4.7	< 300	> 0.12
x070	40.5 ± 4.7	< 300	> 0.14	x180	26.7 ± 4.5	< 300	> 0.09	R27	36.1 ± 5.2	< 300	> 0.12
x076	42.9 ± 4.5	< 300	> 0.14	x184	27.7 ± 4.6	< 300	> 0.09	R37	33.8 ± 5.5	< 300	> 0.11
x078	29.3 ± 5.2	< 300	> 0.10	x188	26.0 ± 4.6	< 300	> 0.09	R39	33.1 ± 5.2	< 300	> 0.11
x080	30.1 ± 4.7	< 300	> 0.10	x190	25.7 ± 4.5	< 300	> 0.09	R43	31.2 ± 4.5	< 300	> 0.10
x085	36.0 ± 4.7	< 300	> 0.12	x192	25.4 ± 4.6	< 300	> 0.08	R45	31.0 ± 4.8	< 300	> 0.10
x090	30.0 ± 4.5	< 300	> 0.10	x196	29.8 ± 4.5	< 300	> 0.10	R50	30.2 ± 4.8	< 300	> 0.10
x092	28.6 ± 4.6	< 300	> 0.10	x199	23.2 ± 4.5	< 300	> 0.08	R51	29.7 ± 4.7	< 300	> 0.10
x093	39.4 ± 5.1	< 300	> 0.13	x201	23.0 ± 4.5	< 300	> 0.08	R55	27.3 ± 4.7	< 300	> 0.09
x096	30.7 ± 4.6	< 300	> 0.10	x203	25.6 ± 4.5	< 300	> 0.09	R57	26.6 ± 4.6	< 300	> 0.09
x097	30.9 ± 4.6	< 300	> 0.10	x206	27.9 ± 5.2	< 300	> 0.09	R58	26.5 ± 4.6	< 300	> 0.09
x099	29.7 ± 4.5	< 300	> 0.10	x208	31.5 ± 4.7	< 300	> 0.10	R66	25.1 ± 4.8	< 300	> 0.08
x105	35.0 ± 4.8	< 300	> 0.12	x211	26.0 ± 4.5	< 300	> 0.09	R67	25.1 ± 4.6	< 300	> 0.08
x107	35.3 ± 4.8	< 300	> 0.12	x216	24.9 ± 4.5	< 300	> 0.08	R68	24.9 ± 4.6	< 300	> 0.08

Table 8 *continued*

Table 8 (continued)

ID	f_{500}	S_{radio}	HizIdx	ID	f_{500}	S_{radio}	HizIdx	ID	f_{500}	S_{radio}	HizIdx
	(mJy)	(μ Jy)	(500)		(mJy)	(μ Jy)	(500)		(mJy)	(μ Jy)	(500)
x110	35.2 ± 4.7	< 300	> 0.12	x217	29.4 ± 4.8	< 300	> 0.10	R71	24.3 ± 4.8	< 300	> 0.08
x119	29.7 ± 4.9	< 300	> 0.10	x224	22.7 ± 4.5	< 300	> 0.08	R73	24.2 ± 4.6	< 300	> 0.08
x125	33.6 ± 5.4	< 300	> 0.11	x226	30.3 ± 4.6	< 300	> 0.10				
500R_XMMLSS_T1_x70	39.4 ± 6.5	< 100	> 0.39								

NOTE—Tier 1 500 μ m risers covered by various radio surveys deeper than FIRST but are not detected. As in Table 3, the leading string in the object ID is omitted for clarity except when the object is the first entry of a given field. The upper limits of their radio flux densities are based on the radio catalogs described in §6.1. The lower limits of HizIdx(500) are calculated using these upper limits. Those that have HizIdx(500) ≥ 0.7 (potentially at $z > 6$) are boldfaced and marked with asterisk (see §7.4).

6.1.3. Summary of radio source matching

In most cases, the currently available radio data in these fields are still very limited in both coverage and sensitivity. Nevertheless, we can still draw two important conclusions. First, radio data are effective in revealing the contamination from blazars whose SEDs have the same rising trend but are due to their nonthermal emissions. While they only constitute a small fraction ($\sim 1.0\%$) among 500 μ m risers (see Table 5), these contaminants are often the brightest among the sample and thus are the easiest to select for follow-up studies. Therefore, checking the sample against radio surveys sensitive to a few mJy level will be desirable. Second, only a small fraction of 500 μ m risers harbor nonblazar, radio-loud AGNs. The FIRST data, whose sensitivity reaches well below ~ 1 mJy (the conventional dividing line between AGN-dominated and star-formation-dominated regimes), have revealed three such AGNs, or $\sim 0.8\%$, among our 500 μ m risers (see Table 5). The data in the CDFS (not accessible by FIRST) have added two more (including one at the borderline; see Table 6) among the 32 that are within the radio coverage. If adding the latter, the radio-loud AGN fraction among our 500 μ m risers is $\sim 1.2\%$.

We shall point out that harboring a radio-loud AGN is not a criterion against a source being at high redshift. In fact, AGNs as strong as quasars at high redshifts can have cold-dust emissions due to heating by star formation, and it is known that such systems do exist (see, e.g., Ma & Yan 2015). Due to the lack of further observations, we will not discuss these radio-loud AGNs any further in this paper. On the other hand, 30 of our 500 μ m risers have radio emissions in the star-formation-dominated regime (§6.1.2). As we will discuss in §7.4, they are not likely at high redshifts. The more interesting objects are those that are weak or not detected in the deepest radio data, which will be discussed in detail in §7.4.

6.2. Radio Properties of SPIRE Dropouts

For the same reason, here we discuss the radio properties of the SPIRE dropouts in the areas where sufficiently deep radio data are available. We again use the same matching procedure as in §6.1, i.e., searching for matches within the matching radius of $r = 10''$, and then determining if a match is reliable by checking if it satisfies $\Delta/\sigma \leq 1.5$. The dominant term to σ_{pos} is σ_{SCUBA2} , which is the positional uncertainty due to the large beam

size of SCUBA2 850 μ m ($13''$) and is calculated individually based on the source S/N, “detection-SNR” as in the S2CLS catalog. The radio source position uncertainty is calculated at the fixed S/N = 5 as in §6.1, and only contributes a negligible amount to σ_{pos} in all cases here. The matching results are summarized in Table 9. The matched sources are shown in Table 10, and the unmatched ones are indicated as such in Table 11. We provide some details below for all these fields.

– *COSMOS* The VLA 3 GHz map of Smolčić et al. (2017) covers the entire field and hence all of our SPIRE dropouts in this field. Among the 26 Tier 1 objects, 15 objects have 3 GHz matches within $r = 10''$. Ten of them have $\Delta/\sigma \leq 1.5$ and hence are reliable. The other five are not regarded as the real counterparts. These 5 objects, together with the 11 that have no entries in the 3 GHz catalog, are assigned the conservative, 5 σ upper limit of $S_{3.0} \leq 11.5 \mu\text{Jy}$ (corresponding to $S_{1.4} \leq 21.2 \mu\text{Jy}$ under $S_\nu \sim \nu^{-0.8}$).

– *EGS* The VLA 1.4 GHz map of Ivison et al. (2007a) covers about only half of the field and four of our objects (out of six). However, none are matched with radio counterparts. We assign them the 5 σ upper limit of 130 μJy .

– *GOODS-N* The VLA 1.4 GHz map of Morrison et al. (2010) covers the entire field and hence all three of our Tier 1 objects. However, none of them are matched. We assign the 5 σ upper limit of 20 μJy to all of them.

– *LH* This field is fully covered by the deep VLA 1.4 GHz map of (Owen & Morrison 2008), which extends over an area of $40' \times 40'$ and reaches rms $\sim 2.7 \mu\text{Jy beam}^{-1}$ with the beam size of $1.''63 \times 1.''57$ (corresponding to $\sigma_{\text{pos}}^{\text{VLA}} = 0.''27$). The radio catalog includes the sources that are detected above 5 σ . Two of the three Tier 1 objects are matched with their radio counterparts in this catalog, with $S_{1.4} = 28.5 \pm 4.2$ and $47.7 \pm 7.1 \mu\text{Jy}$. For the object that is not included in the radio catalog, we assign the 5 σ upper limit of 13.5 μJy .

– *UDS* For this field, we mostly use the VLA 1.4 GHz data of Arumugam (2013), which are $2\times$ deeper than those of Simpson et al. (2006) and are of $3\times$ higher resolution (beam size $1.''82 \times 1.''63$, corresponding to $\sigma_{\text{pos}}^{\text{VLA}} = 0.''29$). However, these data are not directly available. We use instead the catalog of Michałowski et al. (2017), where all the S2CLS sources in this field have been matched for radio counterparts to S/N = 3 using the data of Arumugam (2013). As it turns out,

Table 9. Summary of matching Tier 1 SPIRE dropouts to deep radio data

Field	Facility	Area (deg ²)	Beam Size ($''$)	$\sigma_{\text{pos}}^{\text{Radio}}$ ($''$)	Sensitivity (μJy)	Obj Coverage	Obj Matched
COSMOS	VLA, 3.0 GHz	1.34	0.75	0.13	11.5	26/26	10
EGS	VLA, 1.4 GHz	0.16	3.8	0.66	130	4/6	0
GOODS-N	VLA, 1.4 GHz	0.07	1.7	0.29	20	3/3	1
LH	VLA, 1.4 MHz	0.28	1.63 \times 1.57	0.27	13.5	3/3	2
UDS	VLA, 1.4 GHz	0.94	1.82 \times 1.63	0.29	60	57/57	9

NOTE—The quoted numbers under “Area” are for the overlapping regions of the 850 μm and the radio observations. The values of $\sigma_{\text{pos}}^{\text{Radio}}$ are calculated based on Equation 2 and $S/N = 5$. The sensitivity levels are based on the source catalogs that we used, and in most cases correspond to $S/N = 5$, except in UDS where it corresponds to $S/N = 3$. For the 3 GHz data in COSMOS, the conversion to 1.4 GHz for the quoted sensitivity levels can be done by assuming a power law SED of $S_\nu \sim \nu^{-0.8}$. The number pairs under “Obj Coverage” are those of the objects in the areas covered by the relevant radio data and the total in the Tier 1 samples, respectively, while the numbers under “Obj Matched” are those of the objects detected above the quoted sensitivity levels.

8 of our 57 objects have reported 1.4 GHz detections that fulfill our matching criterion. They have $S_{1.4}$ ranging from 56.2 to 639 μJy , with S/N of 3.3 to 35.2. Based on the sensitivity map provided in Figure 2.1 of Arumugam (2013), we assign the universal 3σ upper limit of 60 μJy to the rest objects that do not have reported radio counterparts in Michałowski et al. (2017). The two objects that are also in Ikarashi et al. (2017), our SD850-UDS-T1-A36 and A42, need further explanation. According to Ikarashi et al. (2017), A42 (their ASXDF1100.231.1) is detected at $S/N = 3.3$ in the data of Arumugam (2013) (but no flux density is given). However, the catalog of Michałowski et al. (2017) based on the same data does not list it as being detected to $S/N = 3$. Here we follow Michałowski et al. (2017), treat it as a nondetection, and put it in Table 11. For A36 (their ASXDF1100.053.1), Ikarashi et al. (2017) have obtained their own VLA 6 GHz measurement of $S_{6.0} = 4.5 \pm 1.1 \mu\text{Jy}$. Its radio position is not given, however. We treat this source as a detection and put it in Table 10. Thus, the number of radio-undetected SPIRE dropouts in this field is 48.

In summary, the radio data cover most of these fields. About 23% of the Tier 1 SPIRE dropouts are detected, and all of them are in the star formation dominated regime. There are still $\sim 77\%$ of the Tier 1 SPIRE dropouts not detected in radio, partly due to the fact that the radio data are still not deep enough. However, there is also a possibility that some of them are at high redshifts, which we will discuss further in §7.4.

7. DISCUSSION

In the above sections, we present our large samples of 500 μm risers and SPIRE dropouts. Admittedly, these samples suffer from the same drawback of the parent catalogs that we have used (the HerMES DR4 catalogs and the S2CLS catalog), namely, the difficulty in obtaining high-precision photometry due to source blending in single-dish data, which is a long-standing problem. We refer the reader to the relevant documentations cited above for the details such as source incompleteness, spurious detections, photometric errors, etc. Moreover, there could be an additional source of incompleteness introduced in our visual inspection step, which cannot

be assessed through simulations because we do not have the means to reproduce the parent catalogs. Therefore, any applications of our samples for statistical purposes should be done with caution. With these caveats in mind, here we discuss some limited statistical properties of our samples, their prospect of being at high z , and their implications for the dust-embedded star formation in the early universe, all to the extent that we believe is still reasonable.

7.1. Surface density of 500 μm risers

At the first glance, it seems that the surface density of 500 μm risers varies greatly among these 11 fields (see Table 1): the average is 6.45 deg^{-2} with the dispersion of 2.54 deg^{-2} , and the highest value is a factor of 4.4 of the lowest. We show that, however, this is largely due to the different sensitivity levels (i.e., survey limits) of the fields.

The survey limits of the HerMES DR4 data are not directly given in the existing HerMES documentations. For our purposes, we adopt the confusion noise (see §3 and Table 1) as the proxy to the sensitivity, because it is the dominant noise term in all of the HerMES data studied here. The left panel of Figure 7 shows the surface densities of the 500 μm risers versus the confusion noises in 500 μm ($N_{\text{conf}}^{500\mu\text{m}}$). The open circles indicate the total surface densities in the field, while the red triangles and the blue diamonds are for the densities calculated using the xID-based and the residual-based objects, respectively. Clearly, the xID-based surface density increases as $N_{\text{conf}}^{500\mu\text{m}}$ decreases, i.e., as the sensitivity improves⁵. This indicates that there are more 500 μm risers at the fainter levels. The total surface density shows a similar

⁵ As the SPIRE observations were simultaneous in all three bands, we see the same trends when using the confusion noise in 250 μm as the variable. The 350 μm total errors as reported in the DR4 xID catalogs are incorrect in ELAIS-N2, which result in the incorrect calculation of $N_{\text{conf}}^{350\mu\text{m}}$ in the field. After discarding this field, we also obtain similar trends using $N_{\text{conf}}^{350\mu\text{m}}$ as the variable. The erroneous $N_{\text{conf}}^{350\mu\text{m}}$ do not affect our target selection, however.

Table 10. Match of Tier 1 SPIRE dropouts to radio data

Object Name	σ_{pos} ($''$)	Δ_{pos} ($''$)	Δ/σ	S_{850} (mJy)	RA _{radio}	DEC _{radio}	S_{radio} (μJy)	HizIdx (850)	References
SD850_COSMOS.T1.A04	1.4	1.3	1.1	11.7 ± 2.1	9:59:10.33	2:48:55.72	21.7 ± 2.7	0.29	(1)
SD850_COSMOS.T1.A11	1.5	1.8	0.8	5.4 ± 1.4	9:59:31.16	2:14:33.99	30.5 ± 2.7	0.10	(1)
SD850_COSMOS.T1.A15	2.2	2.0	1.1	5.8 ± 1.4	10:00:16.99	1:43:26.79	16.9 ± 2.3	0.19	(1)
SD850_COSMOS.T1.A18	3.0	2.0	1.5	5.1 ± 1.3	9:58:34.65	2:18:02.71	14.8 ± 2.4	0.19	(1)
SD850_COSMOS.T1.A20	0.4	2.1	0.2	4.7 ± 1.2	10:00:47.10	2:10:16.62	11.4 ± 2.3	0.22	(1)
SD850_COSMOS.T1.A23	2.2	2.1	1.0	6.3 ± 1.7	9:59:58.79	2:34:58.02	21.6 ± 2.5	0.16	(1)
SD850_COSMOS.T1.A30	2.0	2.2	0.9	6.7 ± 1.8	9:58:43.44	2:45:18.14	15.7 ± 2.5	0.23	(1)
SD850_COSMOS.T1.B06	2.7	1.9	1.5	6.3 ± 1.4	10:00:21.36	2:00:41.26	18.9 ± 2.5	0.18	(1)
SD850_COSMOS.T1.B14	1.1	2.1	0.5	4.1 ± 0.9	10:00:23.26	2:13:44.09	14.1 ± 2.4	0.16	(1)
SD850_COSMOS.T1.B16	1.2	2.1	0.5	6.3 ± 1.6	10:00:37.27	2:49:11.19	13.3 ± 2.5	0.26	(1)
SD850_GOODSN.T1.B01	2.1	1.5	1.4	7.2 ± 1.2	12:36:31.92	62:17:14.70	26.4 ± 4.9	0.27	(2)
SD850_LH.T1.A02	1.4	1.6	0.9	6.8 ± 1.4	10:45:02.00	59:04:03.30	28.5 ± 4.2	0.24	(3)
SD850_LH.T1.A03	1.7	1.7	1.0	6.3 ± 1.6	10:47:20.72	58:51:53.00	47.7 ± 7.1	0.13	(3)
SD850_UDS.T1.A09	1.4	1.8	0.8	6.4 ± 1.1	2:19:08.88	-5:13:55.30	639.2 ± 18.2	0.01	(4)
SD850_UDS.T1.A41	1.9	2.3	0.8	4.8 ± 1.1	2:16:41.95	-5:07:04.00	56.2 ± 15.8	0.09	(4)
SD850_UDS.T1.A48	4.0	2.7	1.5	4.1 ± 1.0	2:16:46.94	-4:45:08.80	532.6 ± 29.3	0.01	(4)
SD850_UDS.T1.A57	2.8	2.6	1.1	4.3 ± 1.1	2:17:51.14	-4:48:06.70	101.0 ± 16.5	0.04	(4)
SD850_UDS.T1.A62	2.6	2.8	1.0	4.0 ± 1.0	2:18:16.70	-5:15:45.10	58.2 ± 15.8	0.07	(4)
SD850_UDS.T1.B04	2.0	1.3	1.5	8.5 ± 1.4	2:18:07.19	-4:44:13.80	67.7 ± 18.6	0.13	(4)
SD850_UDS.T1.B11	2.2	1.6	1.3	6.9 ± 1.2	2:19:24.88	-5:09:20.70	84.7 ± 21.2	0.08	(4)
SD850_UDS.T1.B16	2.4	2.0	1.2	5.6 ± 1.1	2:17:03.08	-4:43:17.80	119.8 ± 36.4	0.05	(4)
SD850_UDS.T1.A36	4.8 ± 1.1	4.6 ± 1.1	0.33	(5)
SD850_COSMOS.T1.A03	3.0	1.3	2.4	11.8 ± 1.9	9:59:57.29	2:27:30.54	28.8 ± 2.7	...	(1)
SD850_COSMOS.T1.A19	5.7	2.1	2.8	5.1 ± 1.2	10:00:28.82	2:05:23.53	21.7 ± 2.7	...	(1)
SD850_COSMOS.T1.A22	5.0	2.1	2.3	5.5 ± 1.4	10:00:23.38	2:01:21.50	27.8 ± 2.8	...	(1)
SD850_COSMOS.T1.A26	9.6	2.1	4.5	4.0 ± 0.9	10:00:08.15	2:17:11.55	21.5 ± 2.6	...	(1)
SD850_COSMOS.T1.B05	3.6	1.7	2.1	8.0 ± 1.8	10:00:06.49	2:38:37.44	12.6 ± 2.4	...	(1)
SD850_GOODSN.T1.A02	7.2	1.6	4.6	5.9 ± 1.3	12:36:51.72	62:12:21.40	56.0 ± 4.5	...	(2)

NOTE—Tier 1 SPIRE dropouts matched to the radio sources in various surveys. The matching radius is $r = 10''$. Only the top 21 matches that have $\Delta/\sigma \leq 1.5$ are deemed to be reliable. “HizIdx” is calculated based on Equation 3. For the bottom six objects, they only have lower limits of HizIdx because they are treated as with no radio counterparts and thus only have upper limits of their radio flux densities. The radio data are from the references listed in the last column. These are: (1) Smolčić et al. (2017), 3 GHz; (2) Morrison et al. (2010), 1.4 GHz; (3) Owen & Morrison (2008), 1.4 GHz; (4) Michałowski et al. (2017), 1.4 GHz; (5) Ikarashi et al. (2017), 6 GHz.

behavior, because the total sample is dominated by the xID-based objects.

The behavior of the surface density of the residual-based objects, however, is almost flat. To further investigate this seemingly counterintuitive problem, we check the median f_{500} values (f_{500}^{med}) of the 500 μm risers in all fields. These are shown in the right panel of Figure 7 against $N_{\text{conf}}^{500\mu\text{m}}$ using the same legends. The xID-based objects show the trend of decreasing f_{500}^{med} with decreasing $N_{\text{conf}}^{500\mu\text{m}}$, which is consistent with the expectation that when we reach fainter limits, we find fainter 500 μm risers. The residual-based objects also follow the same trend in general, which is to say that this type of object is also fainter when we reach fainter survey limits. This suggests that the flat behavior of the blue diamonds in the left panel is simply due to the canceling of two opposite effects: as the sensitivity improves, some 500 μm risers that would not be detected in 250 μm at a brighter level are now detected in 250 μm (they would move from the “residual-based” sample to the “xID-based” sample); in the meantime, roughly the same amount of 500 μm risers not detectable in 500 μm previously at a brighter level now becomes detected in

500 μm (roughly the same number of objects replenishes the “residual-based” sample).

To better describe the behavior of the open circle in the left panel of Figure 7, we perform a linear fit and obtain $\Sigma = -3.03 \times N_{\text{conf}}^{500\mu\text{m}} + 20.3$, with the dispersion of 1.0.

7.2. Comparison to the literature

Here we compare to the surface densities of 500 μm risers as inferred from the work of other teams as mentioned in §1.

The sample of Dowell et al. (2014) using the early HerMES data consists of 39 objects over 21 deg², with $f_{500}^{\text{med}} = 31.9$ mJy. Therefore, their overall surface density is 1.9 deg⁻². Their objects have been selected using $f_{500} \geq f_{350} \geq f_{250}$ (as measured on their smoothed maps), which are similar to (but not exactly the same as) our criteria. They also impose an additional requirement of $f_{500} \geq 30$ mJy. It is difficult to compare to the S/N level of their objects, because they require S/N > 4 on the difference maps. Ignoring this complication, we select a subsample from our objects, requiring $f_{500} \geq 30$ mJy. This results in 396 objects and implies

Table 11. Tier 1 SPIRE dropouts undetected in radio

ID	S_{850}	S_{radio}	HizIdx	ID	S_{850}	S_{radio}	HizIdx	ID	S_{850}	S_{radio}	HizIdx
	(mJy)	(μ Jy)	(850)		(mJy)	(μ Jy)	(850)		(mJy)	(μ Jy)	(850)
SD850-COSMOS-T1-A02	9.0 ± 1.3	< 11.5	> 0.43	A12	7.6 ± 1.8	< 11.5	> 0.36	A31	7.2 ± 2.0	< 11.5	> 0.34
A03	11.8 ± 1.9	< 11.5	$> \mathbf{0.56^*}$	A13	6.7 ± 1.6	< 11.5	> 0.32	B03	5.5 ± 1.1	< 11.5	> 0.26
A06	9.5 ± 2.0	< 11.5	> 0.45	A19	5.1 ± 1.2	< 11.5	> 0.24	B05	8.0 ± 1.8	< 11.5	> 0.38
A07	9.5 ± 2.0	< 11.5	> 0.45	A22	5.5 ± 1.4	< 11.5	> 0.26	B07	8.5 ± 1.9	< 11.5	> 0.40
A08	6.2 ± 1.5	< 11.5	> 0.30	A26	4.0 ± 0.9	< 11.5	> 0.19				
A10	7.9 ± 1.9	< 11.5	> 0.38	A29	6.3 ± 1.8	< 11.5	> 0.30				
SD850-EGS-T1-A09	5.7 ± 1.4	< 130	> 0.04	A12	4.7 ± 1.1	< 130	> 0.04				
A11	7.1 ± 1.7	< 130	> 0.05	A13	5.0 ± 1.3	< 130	> 0.04				
SD850-GOODSN-T1-A01	6.7 ± 1.4	< 20	> 0.33	A02	5.9 ± 1.3	< 20	> 0.30				
SD850-LH-T1-A04	4.7 ± 1.2	< 13.5	> 0.35								
SD850-UDS-T1-A05	7.5 ± 1.2	< 60	> 0.13	A45	4.4 ± 1.1	< 60	> 0.07	A79	3.8 ± 1.0	< 60	> 0.06
A08	6.7 ± 1.2	< 60	> 0.11	A47	4.4 ± 1.1	< 60	> 0.07	A81	3.8 ± 1.0	< 60	> 0.06
A10	6.2 ± 1.2	< 60	> 0.10	A50	4.2 ± 1.1	< 60	> 0.07	A82	3.9 ± 1.1	< 60	> 0.06
A11	5.8 ± 1.1	< 60	> 0.10	A51	4.7 ± 1.1	< 60	> 0.08	A84	3.4 ± 1.0	< 60	> 0.06
A15	6.0 ± 1.2	< 60	> 0.10	A54	4.4 ± 1.1	< 60	> 0.07	A85	3.6 ± 1.0	< 60	> 0.06
A16	6.7 ± 1.4	< 60	> 0.11	A55	4.2 ± 1.1	< 60	> 0.07	B14	5.7 ± 1.2	< 60	> 0.09
A18	5.6 ± 1.1	< 60	> 0.09	A56	4.1 ± 1.0	< 60	> 0.07	B18	5.4 ± 1.1	< 60	> 0.09
A19	5.9 ± 1.1	< 60	> 0.10	A59	4.4 ± 1.1	< 60	> 0.07	B22	5.2 ± 1.1	< 60	> 0.09
A23	5.6 ± 1.2	< 60	> 0.09	A60	4.2 ± 1.1	< 60	> 0.07	B24	4.6 ± 1.0	< 60	> 0.08
A33	4.9 ± 1.1	< 60	> 0.08	A61	4.2 ± 1.0	< 60	> 0.07	B27	4.5 ± 1.1	< 60	> 0.08
A34	5.0 ± 1.1	< 60	> 0.08	A68	4.0 ± 1.1	< 60	> 0.07	B28	4.9 ± 1.1	< 60	> 0.08
A37	4.5 ± 1.1	< 60	> 0.08	A71	3.7 ± 1.0	< 60	> 0.06	B32	4.5 ± 1.1	< 60	> 0.08
A38	4.7 ± 1.1	< 60	> 0.08	A72	3.8 ± 1.0	< 60	> 0.06	B34	4.3 ± 1.0	< 60	> 0.07
A39	4.5 ± 1.1	< 60	> 0.08	A73	3.9 ± 1.0	< 60	> 0.06	B37	4.1 ± 1.0	< 60	> 0.07
A42	4.5 ± 1.1	< 60	> 0.07	A78	3.8 ± 1.0	< 60	> 0.06	B42	4.0 ± 1.1	< 60	> 0.07
A40	4.7 ± 1.0	< 60	> 0.08	A80	4.6 ± 1.3	< 60	> 0.08	B43	4.2 ± 1.0	< 60	> 0.07

NOTE—Tier 1 SPIRE dropouts covered by various radio surveys but are not detected. As in Table 4, the leading string in the object ID is omitted for clarity except when the object is the first entry of a given field. The upper limits of their radio flux densities are based on the radio catalogs described in §6.2. The lower limits of HizIdx(850) are calculated using these upper limits. The one that has HizIdx(850) ≥ 0.5 (potentially at $z > 6$) is boldfaced and marked with asterisk (see §7.4).

the surface density of 3.7 deg^{-2} , which is $2\times$ higher than that of Dowell et al. (2014).

The sample of Asboth et al. (2016) in the 274 deg^2 HeLMS field consists of 477 objects, implying the surface density of 1.7 deg^{-2} . Their objects are selected using the same color criteria as ours but are all significantly brighter, with $f_{500} > 52 \text{ mJy}$. Our sample only has 39 objects that have $f_{500} > 52 \text{ mJy}$, and the corresponding surface density would only be 0.37 deg^{-2} , which is a factor of 4.2 lower.

The sample of 7971 objects of Ivison et al. (2016) are selected using $f_{500}/f_{350} \geq 0.85$ and $f_{500}/f_{250} \geq 1.5$, which are less stringent than ours. As their full sample are not publicly available, it is difficult to make a direct comparison. Taken at the face value, their 7971 objects over 660 deg^2 implies a surface density of 12.1 deg^{-2} . They also state that at least $26 \pm 5\%$ of their objects are reliable, which then implies the minimum of 3.1 deg^{-2} . For comparison, the overall surface density of our sample is 5.9 deg^{-2} .

The sample of Donevski et al. (2018) consists of 133 objects over 55 deg^2 , implying 2.4 deg^{-2} . They use the same color criteria as ours, but impose the additional requirements of $f_{500} > 30 \text{ mJy}$ (corresponding to $S/N > 4$ on their $500 \mu\text{m}$ maps) and $f_{250} > 13.2 \text{ mJy}$. We

select a subsample from our objects that meet the same flux density cutoffs and obtain 381 objects. This implies 3.6 deg^{-2} , which is significantly larger than theirs.

7.3. Surface density of SPIRE Dropouts

The SPIRE dropouts among the S2CLS fields also seem to vary greatly in surface density (see Table 2). However, this again is largely due to a systematic effect: the selection of our SPIRE dropouts depends on the sensitivity of the S2CLS $850 \mu\text{m}$ data, which varies considerably among the fields.

To demonstrate this point, let us take the Tier 1 samples in the UDS and the COSMOS fields for examples. These two fields contribute 60.0% (57 objects) and 27.4% (26 objects) of the total, respectively, and are the only two that have sufficient statistics for our purpose. While the former covers a smaller area than the latter one (0.96 versus 1.34 deg^2), it has detected more $850 \mu\text{m}$ objects than the latter (1085 vs. 719 objects) because of its better sensitivity (0.9 versus $1.6 \text{ mJy beam}^{-1}$). This is also reflected in the SPIRE dropouts that we selected: most of these objects in the UDS field have $S_{850} < 5 \text{ mJy}$ (40 out of 57), while only 3 (out of the 26) in the COSMOS field are in the same regime.

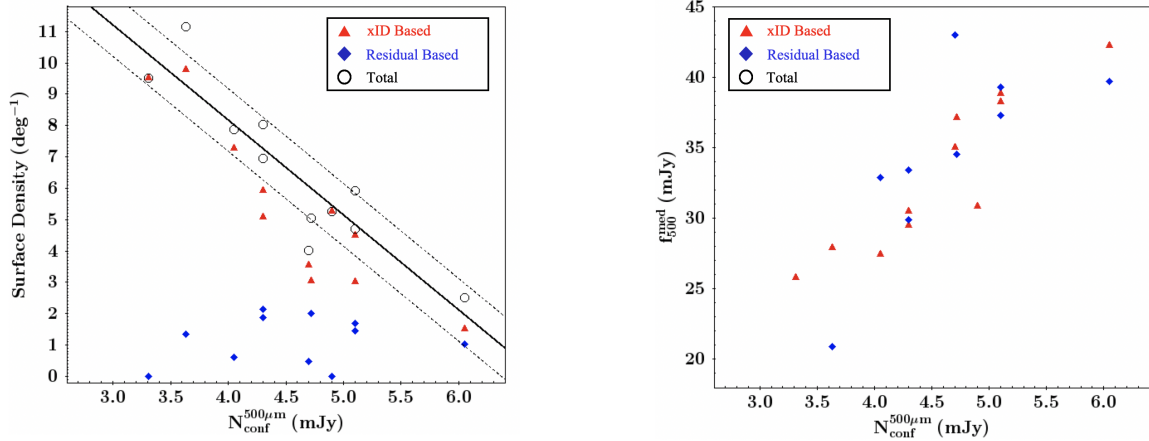


Figure 7. (left) Surface densities of the 500 μm risers in all fields against the confusion noises in 500 μm , $N_{\text{conf}}^{500\mu\text{m}}$, which are used as the proxies to the survey limits. The filled red triangles and the blue diamonds are for the objects selected based on the HERMES DR4 xID catalogs and the residual maps, respectively, and the open black circles indicate the sum of the two. (right) Median 500 μm flux densities of the 500 μm risers against $N_{\text{conf}}^{500\mu\text{m}}$ in all fields. Legends are the same as in the left panel. For clarity, the two fields that do not have residual-based objects are not shown.

According to Geach et al. (2017, see their Fig. 8), the UDS field is $\sim 95\%$ complete at $S_{850} = 5$ mJy, and so the incompleteness correction is negligible above this threshold. The surface density of its SPIRE dropouts at $S_{850} \geq 5$ mJy is therefore 17.7 deg^{-2} . The COSMOS field, on the other hand, is only $\sim 53\%$ complete at this level, and we apply the incompleteness corrections to its SPIRE dropout number counts at $S_{850} \geq 5$ mJy in the successive bins of 0.5 mJy width using Fig. 8 of Geach et al. (2017). The corrected, cumulative number count at $S_{850} \geq 5$ mJy is 28 (as oppose to the original 23 objects), and the corresponding surface density is 20.9 deg^{-2} . The difference between the two fields is well within the Poissonian noise. Taking the average of the two, we obtain the SPIRE dropout surface density of $19.3 \pm 1.6 \text{ deg}^{-2}$ at $S_{850} \geq 5$ mJy.

We note that the above value is only applicable to degree-size fields. As the spatial distributions of SPIRE dropouts show a significant clustering feature (see Figure 6), the surface density can vary significantly in small fields. In the EGS (0.32 deg^2) and the LH (0.28 deg^2) fields, we have three (out of six total) and two (out of three total) SPIRE dropouts at $S_{850} \geq 5$ mJy, respectively. The corresponding surface densities would be 9.4 and 7.1 deg^{-2} , respectively, which are both much lower than the value derived above. On the contrary, in the GOODS-N field that covers only 0.07 deg^2 , all the three SPIRE dropouts are at $S_{850} \geq 5$ mJy. This would imply the surface density of 42.9 deg^{-2} , which is $2.2\times$ higher than the average.

7.4. Prospects of 500 μm risers and SPIRE Dropouts Being at High z

While the initial motivation of our work is to select high- z ULIRGs in the EoR (see §1), it is extremely difficult to further purify our 500 μm riser and SPIRE dropout samples to achieve this goal. Without knowing the exact location of the dust emission peak, the 500 μm riser method is only expected to select objects

at $z \gtrsim 4$ in general but not to create a sample falling within a well-defined redshift range. It is also expected that the selection could be severely contaminated by objects at $z \approx 3$ due to the degeneracy between dust temperature and redshift. For example, Asboth et al. (2016) carried out 3 mm spectroscopy for two of their sources and find that one is at $z = 5.162$ and the other is at $z = 3.798$. Ivison et al. (2016) derived photometric redshifts for their 500 μm risers based on the FIR/sub-mm SEDs, and concluded that the median redshift is at 3.66 and that only a third of their 500 μm risers lie at $z > 4$. This is partly confirmed by Fudamoto et al. (2017), who have done 3 mm spectroscopy on a small subsample of 17 very red objects in Ivison et al. (2016). Among the seven objects that have secure redshifts, one is at $z = 3.8847$ and five are at $4 < z < 5$. Encouragingly, there is one object at $z = 6.027$ (see also Zavala et al. 2018). However, this object is not the reddest in their sample, which demonstrates the large uncertainty in estimating redshifts for 500 μm risers. This is also true for 850/870 μm risers. For example, Oteo et al. (2018) reported a 870 μm riser; however, it is only at $z = 4.002$. The situation for the SPIRE dropouts is even more complicated because we have even less information about their SEDs. Nevertheless, a small fraction of our objects do have further constraints from the radio data, which we discuss in detail below.

7.4.1. Constraints from Radio Data

For the objects that fall within the coverage of radio observations, it could be possible to further constrain their redshifts by incorporating the radio data. A number of photometric redshift derivation schemes have been proposed based on the FIR-radio relation (see e.g., Carilli & Yun 1999; Barger et al. 2000). However, such methods all suffer from a couple of major caveats. First, one would need to assume a fixed power-law index for the radio emission, which could have a wide range of uncertainty over $\alpha \sim -0.3$ to -0.8 . Second, one would also need to assume a fixed dust tempera-

ture, which could have a wide spread of $\sim 20\text{--}60$ K. While the choices of these parameters could be fine-tuned to work reasonably well within the typical redshift range of SMGs at $z \approx 2\text{--}4$, it is unclear how they would perform beyond this range. For example, the famous HDF 850.1, the brightest $850\text{ }\mu\text{m}$ source in the Hubble Deep Field with $S_{850} = 7.0 \pm 0.4$ mJy (Hughes et al. 1998), has $S_{1.4} = 16.73 \pm 4.25\text{ }\mu\text{Jy}$ (Cowie et al. 2009). Using the formalism of Carilli & Yun (1999), one would obtain $z_{ph} = 4.6$. If using that of Barger et al. (2000), one would obtain $z_{ph} = 3.8$. Both are significantly different from the spectroscopic redshift of $z = 5.183$ (Walter et al. 2012). Another example is HFLS3 at $z = 6.34$ of Riechers et al. (2013), which has $S_{880} = 33.0 \pm 2.4$ mJy (the SMA measurement at $880\text{ }\mu\text{m}$) and $S_{1.4} = 59 \pm 11\text{ }\mu\text{Jy}$. Ignoring the small difference between S_{880} and S_{850} , one would then obtain $z_{ph} = 5.0$ and 4.1 based on Carilli & Yun (1999) and Barger et al. (2000), respectively, both of which are also significantly different from the true value.

For this reason, we do not attempt in this work to directly derive z_{ph} using the radio data. Instead, we only select the objects that are radio weak as the most promising candidates at $z > 6$, among which some could be in the EoR.

The problem is how to define “radio weak” in this context. Lacking anything else being a better choice, we use the aforementioned HDF 850.1 and HFLS3 as the references. Recall that HDF 850.1, or our SD850_HDFN_T1_A02, is a SPIRE dropout, while FLS 3, or our 500R_FLS_T1_x44, is a $500\text{ }\mu\text{m}$ riser (but not an $850\text{ }\mu\text{m}$ riser). For the sake of the argument, we introduce a “high- z index,” or “HizIdx” for short, to quantify an object being radio weak by using the flux density ratio between the FIR/submm and radio:

$$\text{HizIdx} = \begin{cases} f_{500} \times 10^{-3} / S_{1.4} & (500\text{ }\mu\text{m} \text{ risers}) \\ S_{850} \times 10^{-3} / S_{1.4} & (\text{SPIRE dropouts}) \end{cases} \quad (3)$$

The $850\text{ }\mu\text{m}$ photometry for HDF 850.1 (at $z = 5.18$) is somewhat different among the data published by different groups (Walter et al. 2012) (see also Cowie et al. 2017). Here we adopt $S_{850} = 5.9 \pm 1.3$ mJy from the S2CLS catalog and obtain $\text{HizIdx}(850) = 0.35$. For FLS 3 (at $z = 6.43$), we obtain $\text{HizIdx}(500) = 0.75$ and $\text{HizIdx}(850) = 0.56$, respectively.

Using the above numbers as a guide, we adopt $\text{HizIdx}(500) \geq 0.7$ to further select $500\text{ }\mu\text{m}$ risers at $z > 6$. To select objects at $z > 6$ from SPIRE dropouts, we adopt $\text{HizIdx}(850) \geq 0.5$. We note that these ad hoc thresholds are so chosen only for the sake of the argument here and are the best that one could adopt at this stage. Other better choices will have to wait until spectroscopic verifications in the future.

7.4.2. High- z candidates in the $500\text{ }\mu\text{m}$ Riser Sample

For the $500\text{ }\mu\text{m}$ risers that have radio counterparts (as described in Section 5.4), we calculate their $\text{HizIdx}(500)$. For those that are within the radio coverage but are not detected, we calculate the lower limits of $\text{HizIdx}(500)$

using the upper limits of the radio flux densities appropriate in the fields. For the radio observations that are not made in 1.4 GHz , we convert the result to $S_{1.4}$ by assuming $S(\nu) \propto \nu^{-0.8}$. These results are listed in Table 7 and 8.

In total, 19 of our $500\text{ }\mu\text{m}$ risers have $\text{HizIdx}(500) \geq 0.7$, distributed over five fields. The COSMOS field is the only one that offers sufficient statistics over a large area to allow a meaningful estimate of the surface density for such radio-constrained high- z candidates. Recall that it has 17 $500\text{ }\mu\text{m}$ risers within the 3 GHz coverage, 10 of which have 3 GHz counterparts. Four of these 10 have $\text{HizIdx}(500) \geq 0.7$. The seven that are not detected at 5σ all have $\text{HizIdx}(500) \geq 0.7$. Therefore, there are 11 candidates (or 64.7% out of the total of 17) at $z > 6$ over 2 deg^2 satisfying our criterion, which correspond to a density of 5.5 deg^{-2} .

7.4.3. High- z candidates in the SPIRE Dropout Sample

Similarly, we calculate $\text{HizIdx}(850)$ or the lower limits for the SPIRE dropouts and list the results in the catalog. As it turns out, none of the objects that have identified radio counterparts satisfy our criterion for $z > 6$. However, we can still obtain useful information from those that are not detected in the existing radio data.

The most stringent limits are again from the COSMOS field over 1.34 deg^2 , which has 16 SPIRE dropouts that do not have counterparts in the 3 GHz catalog. Adopting the 5σ limit of $11.5\text{ }\mu\text{Jy}$ and assuming $S(\nu) \propto \nu^{-0.8}$ as before, we find that one object, SD850_COSMOS_T1_A03 with $S_{850} = 11.8 \pm 1.9$ mJy, has $\text{HizIdx}(850) > 0.56$ and thus satisfies our criterion for $z > 6$. Therefore, we can derive the lower limit of $z > 6$ objects among the SPIRE dropouts to be 0.8 deg^{-2} . The upper limit can be obtained by assuming that all these 16 objects are not detected even at higher sensitivity levels. Indeed, if they all remain radio undetected at the $\sim 2.5\sigma$ level, they would all have $\text{HizIdx}(850) > 0.5$. Out of these 16 objects, 15 have $S_{850} \geq 5.0$ mJy, and therefore we derive the upper limit of the surface density as 11.2 deg^{-2} to $S_{850} = 5.0$ mJy. If we further consider the incompleteness correction for the COSMOS field in $850\text{ }\mu\text{m}$ (see in §7.3), the upper limit is 13.6 deg^{-2} .

Following the same methodology, we check the upper limits inferred from the other fields, bearing in mind that they have highly nonuniform sensitivities in their radio data. On the order of the field size, the UDS (0.96 deg^2), the EGS (only about half, or $\sim 0.16\text{ deg}^2$ covered by the radio data), the LH (0.28 deg^2), and the GOODS (0.07 deg^2) fields have 13, 2, 1, and 1 radio-undetected objects at $S_{850} \geq 5$ mJy, respectively. The corresponding upper limits for $z > 6$ objects are therefore 13.5, 12.5, 3.6, and 14.3 deg^{-2} to $S_{850} = 5.0$ mJy.

We note in passing that the SPIRE dropout of Greenslade et al. (2019), their “NGP6.D1,” does not meet our HizIdx criterion for $z > 6$. This source has $S_{850} = 12.3 \pm 2.5$ mJy. Their VLA 6 GHz measurement gives $S_{6.0} = 16.9 \pm 4\text{ }\mu\text{Jy}$, which corresponds to $S_{1.4} = 54.1\text{ }\mu\text{Jy}$ if assuming $S(\nu) \propto \nu^{-0.8}$. This gives $\text{HizIdx}(850) = 0.23$. To make $\text{HizIdx}(850) > 0.7$, it would

have to have a very flat SED slope of $\alpha \leq 0.03$, which does not seem likely.

7.4.4. Global star formation rate density at $z > 6$ hidden by dust

Using the results in §7.4.2 and 7.4.3, here we attempt to estimate the IR-based (i.e., dust-embedded) global star formation rate density (GSFRD; $\dot{\rho}_*(\text{IR})$) at $z > 6$. We only use the values based on the COSMOS field. For the surface density of $z > 6$ SPIRE dropouts, we adopt the average of the lower and the upper limits in Section 6.4.3 as the representative value, i.e., 7.2 deg^{-2} . The combined surface density of $500 \mu\text{m}$ risers and SPIRE dropouts at $z > 6$ is therefore 12.7 deg^{-2} . We assume that this is applicable within $6 < z < 7$, which means that the volume density is $1.4 \times 10^{-6} \text{ Mpc}^{-3}$.

For practical purposes, we further assume that these objects all have $L_{\text{IR}} = 10^{13} L_{\odot}$, which is likely to be the lower end of the true distribution. For example, HFLS3, which is our 500R.FLS.T1.x44, has $L_{\text{IR}} = 1.55 \times 10^{13} L_{\odot}$ even after the correction for the gravitational lensing (Cooray et al. 2014). We apply the conversion given by Kennicutt (1998), which is $\text{SFR} = 1.0 \times 10^{-10} L_{\text{IR}}$ after adjusting for a Chabrier initial mass function (Chabrier 2003). This translates to $\text{SFR} = 10^3 M_{\odot} \text{ yr}^{-1}$ per object. Therefore, we obtain $\dot{\rho}_*(\text{IR}) = 1.4 \times 10^{-3} M_{\odot} \text{ yr}^{-1} \text{ Mpc}^{-3}$. This is comparable to the UV-based GSFRD derived using Lyman-break galaxies (LBGs). For example, Yan et al. (2010) have obtained $\dot{\rho}_*(\text{UV}) = (12.33, 5.50) \times 10^{-3} M_{\odot} \text{ yr}^{-1} \text{ Mpc}^{-3}$ at $z = (6.0, 7.0)$, respectively. Note that these $500 \mu\text{m}$ risers and SPIRE dropouts are not likely visible in the rest-frame UV and hence are not likely to manifest themselves as LBGs (HFLS3 is an example), which means that $\dot{\rho}_*(\text{UV})$ after dust-reddening correction cannot account for $\dot{\rho}_*(\text{IR})$. In other words, the GSFRD value at high redshifts is likely significantly higher than that derived based on LBGs alone. This point has been raised before (see, e.g. Cowie et al. 2009), and recently was further reinforced by Wang et al. (2019) in their $870 \mu\text{m}$ detections of H dropouts ($3.6 \mu\text{m}$ sources that are invisible from UV to H band), the bulk of which are likely at $z > 3$ and some of which could be at $z > 6$. Wang et al. (2019) estimated that the volume density of their objects is $2 \times 10^{-5} \text{ Mpc}^{-3}$, which is about an order of magnitude higher than that of our objects. However, as their L_{IR} are at least an order of magnitude lower, the total contribution to the GSFRD from these less luminous objects ($0.9 \times 10^{-3} M_{\odot} \text{ yr}^{-1} \text{ Mpc}^{-3}$ at $z = 6$) is comparable to that from our objects.

We shall caution that our conclusions above hinge upon a number of assumptions, most importantly the validity of the $z > 6$ candidates derived based on HiZIdx. Obviously, spectroscopic confirmation of a significant sample like what presented here is the only path to solving the problem.

8. SUMMARY

We have carried out a comprehensive search for $500 \mu\text{m}$ risers using the HerMES data in 106.5 deg^2 and for SPIRE dropouts using the S2CLS data in the

2.98 deg^2 that overlap the HerMES coverage. Both types of objects are candidate ULIRGs at high redshifts, some of which could be at $z > 6$ and in the EoR. The main objective of this paper is to present the selections and the catalogs of these rare sources to facilitate follow-up observations. We focus on the “Tier 1” objects, which we believe are the least affected by contaminations and thus are valuable targets for future studies. For completeness, the catalogs of the less promising, “Tier 2” objects are also included in this paper.

In total, we present 629 Tier 1 $500 \mu\text{m}$ risers in 11 HerMES fields, all detected at $\text{S/N} \geq 5$ (confusion noise included) in $500 \mu\text{m}$. These objects satisfy the simple criterion of $f_{500} > f_{350} > f_{250}$, which is similar to (but not exactly the same as) most of the existing selections of $500 \mu\text{m}$ risers in the literature. Compared to the existing ones, our sample is unique in its flux limit and spatial coverage. About 77.4% of this sample (487 objects) are selected from the HerMES DR4 xID catalogs (“xID based”; the objects have reported $250 \mu\text{m}$ detections), and the other 22.6% (142 objects) are selected through detecting objects in the $500 \mu\text{m}$ residual maps generated by subtracting off the sources in the xID catalogs (“residual based”; the objects do not have reported $250 \mu\text{m}$ detections). Their spatial distributions show obvious patterns of clustering. The inferred surface density depends on the survey limit, which ranges from $\sim 2.1 \text{ deg}^{-2}$ at the confusion noise level of $N_{\text{conf}}^{500\mu\text{m}} \approx 6 \text{ mJy}$ (or equivalently, 5σ flux density limit of $f_{500} \gtrsim 30 \text{ mJy}$) to $\sim 8.2 \text{ deg}^{-2}$ at $N_{\text{conf}}^{500\mu\text{m}} \approx 4 \text{ mJy}$ (or equivalently, 5σ limit of $f_{500} \gtrsim 20 \text{ mJy}$).

The search for SPIRE dropouts is relatively new, and in fact our sample is the only significant sample of its kind to date. Our Tier 1 catalog includes 95 SPIRE dropouts in five S2CLS fields that also have HerMES SPIRE data. While the limit of the SPIRE data cannot guarantee that these SPIRE dropouts are $850 \mu\text{m}$ risers, any $850 \mu\text{m}$ risers in these fields must be among these SPIRE dropouts. They all have “detection_SNR” ≥ 5 in the S2CLS catalog, and hence are highly reliable detections in $850 \mu\text{m}$. About 76.8% of them (73 objects) do not have an entry in the HerMES xID catalog (selected by “Method A”). The other 23.2% (22 objects) have $\text{S/N} < 3$ in the xID catalog (selected by “Method B”) and thus could actually be nondetections in SPIRE. The “B” objects also satisfy $(S_{850} + 0.5 \times \text{ErrSr}_{850}) > (f_{250} - 2 \times \text{et}_{250})$. The inferred surface density depends on the survey limits of both S2CLS and HerMES, and the former dominates. From the results in the COSMOS and the UDS fields (the only two degree-size fields), we derive their surface density of $19.3 \pm 1.6 \text{ deg}^{-2}$ at $S_{850} \geq 5 \text{ mJy}$.

The SEDs alone cannot be used to constrain the redshifts of these objects. As FIR/sub-mm galaxies at high redshifts should generally be radio weak, we examine the radio properties of our $500 \mu\text{m}$ risers and SPIRE dropouts using public radio data. Cross-matching with the FIRST data in the northern and the equatorial fields has revealed seven very strong AGNs among the $500 \mu\text{m}$ risers (out of 381 total in these fields), four of which are (likely) blazars because the rising trend of their SEDs ex-

tends into the radio regime. Deeper radio data are available and cover 42.4% of the 500 μm risers (267 out of 629 objects) and almost all of the SPIRE dropouts (93 out of 95 objects). The sensitivity limits of these radio data vary greatly across the fields, resulting in highly different radio detection rates. Nevertheless, the vast majority of our objects are at the sub-millijansky level and weaker, supporting the fact that they are mostly driven by star formation. For ease of use, the relevant radio properties of these objects are included in the catalogs. Furthermore, we introduce the HizIdx parameter, which is the flux density ratio between FIR/sub-mm and radio. Using the well-studied HDF 850.1 ($z = 5.18$) and HFLS3 ($z = 6.43$) as guides, we propose $\text{HizIdx}(500) \geq 0.7$ and $\text{HizIdx}(850) \geq 0.5$ to select $z > 6$ objects from the 500 μm risers and the SPIRE dropouts, respectively. The COSMOS field is the only area where the radio data are deep and wide enough to provide stringent constraints on the surface density of potential $z > 6$ far-IR/sub-mm sources. Based on the aforementioned HizIdx criteria, we find that 19 500 μm risers and one SPIRE dropout could be at $z > 6$, and we derive the surface density of $z > 6$ objects as 5.5 deg^{-2} among the 500 μm risers and $0.8\text{--}13.6 \text{ deg}^{-2}$ among the SPIRE dropouts, respectively. Finally, we point out that dust-embedded GSFRD at $z > 6$ could be comparable to that derived based on LBGs alone. To really understand the role of dust-embedded star formation in the early universe, however, spectroscopic identification of a significant $z > 6$ sample such as presented here will be necessary.

ACKNOWLEDGMENTS

We would like to thank the anonymous referee for the helpful comments. This research is supported in part by the National Natural Science Foundation of China (NSFC, grant No. 11728306), and is also sponsored in part by the Chinese Academy of Sciences (CAS), through a grant to the CAS South America Center for Astronomy (CASSACA) in Santiago, Chile. L.F. acknowledges the support from the NSFC (grant Nos. 11822303 and 11773020) and Shandong Provincial Natural Science Foundation, China (ZR2017QA001, JQ201801). This research has made use of the data from the HerMES project (<http://hermes.sussex.ac.uk>). HerMES is a Herschel Key Programme utilizing Guaranteed Time from the SPIRE instrument team, ESAC scientists, and a mission scientist. The HerMES data were accessed through the Herschel Database in Marseille (HeDaM; <http://hedam.lam.fr>) operated by CeSAM and hosted by the Laboratoire d'Astrophysique de Marseille. This research has also made use of the data from the S2CLS program, which was carried out at the James Clerk Maxwell Telescope (JCMT). The JCMT is operated by the East Asian Observatory on behalf of The National Astronomical Observatory of Japan; Academia Sinica Institute of Astronomy and Astrophysics; the Korea Astronomy and Space Science Institute; and Center for Astronomical Mega-Science (as well as the National Key R&D Program of China with No. 2017YFA0402700). Additional funding support is provided by the Science and Technology Facilities Council of the United Kingdom and participating universities in the United Kingdom and Canada.

REFERENCES

- Ackermann, M., Ajello, M., Atwood, W. B., et al. 2015, *ApJ*, 810, 14
- Arumugam, V. 2013, PhD thesis, The University of Edinburgh (United Kingdom)
- Asboth, V., Conley, A., Sayers, J., et al. 2016, *MNRAS*, 462, 1989
- Barger, A. J., Cowie, L. L., & Richards, E. A. 2000, *AJ*, 119, 2092
- Becker, R. H., White, R. L., & Helfand, D. J. 1995, *ApJ*, 450, 559
- Boone, F., Clément, B., Richard, J., et al. 2013, *A&A*, 559, L1
- Boone, F., Schaerer, D., Richard, J., et al. 2015, in *IAU General Assembly*, Vol. 29, 2256581
- Bouwens, R. J., Illingworth, G. D., Oesch, P. A., et al. 2015, *ApJ*, 803, 34
- Carilli, C. L., & Yun, M. S. 1999, *ApJL*, 513, L13
- Chabrier, G. 2003, *PASP*, 115, 763
- Condon, J. J. 1992, *ARA&A*, 30, 575
- Condon, J. J., Cotton, W. D., Yin, Q. F., et al. 2003, *AJ*, 125, 2411
- Cooray, A., Calanog, J., Wardlow, J. L., et al. 2014, *ApJ*, 790, 40
- Cowie, L. L., Barger, A. J., Hsu, L. Y., et al. 2017, *ApJ*, 837, 139
- Cowie, L. L., Barger, A. J., Wang, W. H., & Williams, J. P. 2009, *ApJL*, 697, L122
- Daddi, E., Dannerbauer, H., Krips, M., et al. 2009a, *ApJL*, 695, L176
- Daddi, E., Dannerbauer, H., Stern, D., et al. 2009b, *ApJ*, 694, 1517
- Decarli, R., Walter, F., Venemans, B. P., et al. 2017, *Nature*, 545, 457
- Diolaiti, E., Bendinelli, O., Bonaccini, D., et al. 2000, in *Proc. SPIE*, Vol. 4007, *Adaptive Optical Systems Technology*, ed. P. L. Wizinowich, 879–888
- Donevski, D., Buat, V., Boone, F., et al. 2018, *A&A*, 614, A33

- Dowell, C. D., Conley, A., Glenn, J., et al. 2014, *ApJ*, 780, 75
- Duivenvoorden, S., Oliver, S., Scudder, J. M., et al. 2018, *MNRAS*, 477, 1099
- Eales, S., Dunne, L., Clements, D., et al. 2010, *PASP*, 122, 499
- Fan, X., Carilli, C. L., & Keating, B. 2006, *ARA&A*, 44, 415
- Franzen, T. M. O., Banfield, J. K., Hales, C. A., et al. 2015, *MNRAS*, 453, 4020
- Fudamoto, Y., Ivison, R. J., Oteo, I., et al. 2017, *MNRAS*, 472, 2028
- Garn, T., Green, D. A., Riley, J. M., & Alexander, P. 2008a, *MNRAS*, 383, 75
- . 2008b, *MNRAS*, 387, 1037
- Garn, T., Green, D. A., Riley, J. M., & Alexander, P. 2009, *MNRAS*, 397, 1101
- Garn, T. S., Green, D. A., Riley, J. M., & Alexander, P. 2010, *Bulletin of the Astronomical Society of India*, 38, 103
- Geach, J. E., Dunlop, J. S., Halpern, M., et al. 2017, *MNRAS*, 465, 1789
- Greenslade, J., Aguilar, E., Clements, D. L., et al. 2019, *MNRAS*, 490, 5317
- Griffin, M. J., Abergel, A., Abreu, A., et al. 2010, *A&A*, 518, L3
- Hatsukade, B., Kohno, K., Aretxaga, I., et al. 2011, *MNRAS*, 411, 102
- Hughes, D. H., Serjeant, S., Dunlop, J., et al. 1998, *Nature*, 394, 241
- Ibar, E., Ivison, R. J., Biggs, A. D., et al. 2009, *MNRAS*, 397, 281
- Ikarashi, S., Ivison, R. J., Caputi, K. I., et al. 2015, *ApJ*, 810, 133
- . 2017, *ApJ*, 835, 286
- Ivison, R. J., Chapman, S. C., Faber, S. M., et al. 2007a, *ApJL*, 660, L77
- Ivison, R. J., Greve, T. R., Dunlop, J. S., et al. 2007b, *MNRAS*, 380, 199
- Ivison, R. J., Lewis, A. J. R., Weiss, A., et al. 2016, *ApJ*, 832, 78
- Kennicutt, Jr., R. C. 1998, *ARA&A*, 36, 189
- Levenson, L., Marsden, G., Zemcov, M., et al. 2010, *MNRAS*, 409, 83
- Ma, Z., & Yan, H. 2015, *ApJ*, 811, 58
- Marchã, M. J. M., & Caccianiga, A. 2013, *MNRAS*, 430, 2464
- Marleau, F. R., Fadda, D., Appleton, P. N., et al. 2007, *ApJ*, 663, 218
- Michałowski, M. J., Dunlop, J. S., Koprowski, M. P., et al. 2017, *MNRAS*, 469, 492
- Miller, N. A., Bonzini, M., Fomalont, E. B., et al. 2013, *ApJS*, 205, 13
- Mingaliev, M. G., Sotnikova, Y. V., Udovitskiy, R. Y., et al. 2014, *A&A*, 572, A59
- Morrison, G. E., Owen, F. N., Dickinson, M., Ivison, R. J., & Ibar, E. 2010, *ApJS*, 188, 178
- Oliver, S. J., Bock, J., Altieri, B., et al. 2012, *MNRAS*, 424, 1614
- Oteo, I., Ivison, R. J., Dunne, L., et al. 2018, *ApJ*, 856, 72
- Ott, S. 2010, in *Astronomical Society of the Pacific Conference Series*, Vol. 434, *Astronomical Data Analysis Software and Systems XIX*, ed. Y. Mizumoto, K.-I. Morita, & M. Ohishi, 139
- Owen, F. N., & Morrison, G. E. 2008, *AJ*, 136, 1889
- Owen, F. N., Morrison, G. E., Klimek, M. D., & Greisen, E. W. 2009, *AJ*, 137, 4846
- Pilbratt, G. L., Riedinger, J. R., Passvogel, T., et al. 2010, *A&A*, 518, L1
- Planck Collaboration, Adam, R., Aghanim, N., et al. 2016, *A&A*, 596, A108
- Pope, A., & Chary, R.-R. 2010, *ApJL*, 715, L171
- Riechers, D. A., Bradford, C. M., Clements, D. L., et al. 2013, *Nature*, 496, 329
- Riechers, D. A., Leung, T. K. D., Ivison, R. J., et al. 2017, *ApJ*, 850, 1
- Roseboom, I. G., Ivison, R. J., Greve, T. R., et al. 2012, *MNRAS*, 419, 2758
- Schinnerer, E., Smolčić, V., Carilli, C. L., et al. 2007, *ApJS*, 172, 46
- Schinnerer, E., Sargent, M. T., Bondi, M., et al. 2010, *ApJS*, 188, 384
- Schneider, D. P., Richards, G. T., Hall, P. B., et al. 2010, *AJ*, 139, 2360
- Simpson, C., Martínez-Sansigre, A., Rawlings, S., et al. 2006, *MNRAS*, 372, 741
- Simpson, J. M., Smail, I., Swinbank, A. M., et al. 2019, *ApJ*, 880, 43
- Smith, M. W. L., Ibar, E., Maddox, S. J., et al. 2017, *ApJS*, 233, 26
- Smolčić, V., Novak, M., Bondi, M., et al. 2017, *A&A*, 602, A1
- Strandet, M. L., Weiss, A., De Breuck, C., et al. 2017, *ApJL*, 842, L15
- Venemans, B. P., Walter, F., Zschaechner, L., et al. 2016, *ApJ*, 816, 37
- Venemans, B. P., McMahon, R. G., Walter, F., et al. 2012, *ApJL*, 751, L25

- Venemans, B. P., Walter, F., Decarli, R., et al. 2017, *ApJL*, 851, L8
- Vernstrom, T., Scott, D., Wall, J. V., et al. 2016, *MNRAS*, 462, 2934
- Viero, M. P., Wang, L., Zemcov, M., et al. 2013, *ApJ*, 772, 77
- Viero, M. P., Asboth, V., Roseboom, I. G., et al. 2014, *ApJS*, 210, 22
- Walter, F., Bertoldi, F., Carilli, C., et al. 2003, *Nature*, 424, 406
- Walter, F., Decarli, R., Carilli, C., et al. 2012, *Nature*, 486, 233
- Wang, L., Viero, M., Clarke, C., et al. 2014, *MNRAS*, 444, 2870
- Wang, T., Schreiber, C., Elbaz, D., et al. 2019, *Nature*, 572, 211
- White, G. J., Hatsukade, B., Pearson, C., et al. 2012, *MNRAS*, 427, 1830
- Yan, H., & Windhorst, R. A. 2004, *ApJL*, 600, L1
- Yan, H.-J., Windhorst, R. A., Hathi, N. P., et al. 2010, *Research in Astronomy and Astrophysics*, 10, 867
- Zavala, J. A., Montaña, A., Hughes, D. H., et al. 2018, *Nature Astronomy*, 2, 56

Table 12. Properties of 500 μm risers in sub-mm/mm

Object Name	f_{250}	f_{350}	f_{500}	S_{850}	HizIdx(500)
500R_COSMOS.T1.x01	18.1 ± 3.4	24.9 ± 6.6	26.2 ± 5.1	7.1 ± 1.9	0.56
500R_COSMOS.T1.x13	23.9 ± 3.4	28.4 ± 6.6	28.6 ± 5.1	11.5 ± 2.0	0.28
500R_COSMOS.T1.x21	25.6 ± 3.4	30.7 ± 6.6	30.8 ± 5.0	6.4 ± 1.9	> 1.45
500R_COSMOS.T1.x34	31.4 ± 3.4	35.0 ± 6.6	39.8 ± 5.1	10.4 ± 1.8	> 1.87
500R_COSMOS.T1.x25	13.8 ± 3.4	21.8 ± 6.6	31.4 ± 5.3	< 3.2	0.37
500R_EGS.T1.x42	16.0 ± 3.5	22.8 ± 4.1	27.1 ± 4.5	7.3 ± 0.9	> 0.21
500R_XMMLSS.T1.x70	29.8 ± 4.6	35.1 ± 7.7	39.4 ± 6.5	9.1 ± 1.5	> 0.39
Object Name	f_{250}	f_{350}	f_{500}	$S_{1.1}$	HizIdx(500)
500R_ADFS.T1.x14	26.3 ± 4.8	29.4 ± 5.6	29.6 ± 5.6	3.4 ± 0.4	> 0.03
500R_ADFS.T1.x20	24.9 ± 4.8	35.5 ± 5.6	37.1 ± 5.7	6.2 ± 0.5	> 0.04
500R_ADFS.T1.x28	27.3 ± 4.8	32.1 ± 5.7	34.0 ± 5.8	6.1 ± 0.8	> 0.03

NOTE—Sub-mm and mm properties of the 500 μm risers that have SCUBA2 850 μm or AzTEC 1.1 mm observations (see §A). The complications in the cases of 500R_COSMOS.T1.x21, 500R_COSMOS.T1.x34 and 500R_XMMLSS.T1.x70 are discussed in the text. HizIdx(500) is defined by Equation 3, and the values are taken from Table 7 and 8.

APPENDIX

A. PROPERTIES OF 500 μM RISERS AT SUBMILLIMETER/MILLIMETER

Only a small number of our 500 μm risers fall within the limited S2CLS coverage. In the S2CLS GOODS-N and LH fields, there are no 500 μm risers. In the COSMOS field, five of our 500 μm risers are covered, namely, 500R_COSMOS.T1.x01, x13, x21, x25, and x34. Only x25 is clearly not detected, which we assign the 2σ upper limit of $S_{850} < 3.2$ mJy (visual examination of the 3 GHz map also shows no hints of any detection). Among those that are detected, x21 is matched to COS.0345; however, its deboosted S_{850} value is reported in the S2CLS catalog as 2.80 ± 2.45 mJy, which is very different from the “observed” $S_{850} = 7.93 \pm 1.90$ mJy and hence is likely erroneous. Here we adopt the mean difference between the observed and the deboosted values in this field as 1.54 mJy, and get $S_{850} = 6.39$ mJy. The case for x34 is complicated. Its centroid is in between two S2CLS objects, COS.0170 and 0191, and is separated from them by $8.''2$ and $10.''9$, respectively. These two S2CLS objects have deboosted $S_{850} = 5.4 \pm 1.2$ and 5.0 ± 1.3 mJy, respectively, and are separated by $17.''1$. It is unclear if x34 is related with either, or if it is the blended result of the two. For our practical purposes here, we assume the latter and further assume that they are at the same redshift. By combining these two objects, we get the deboosted $S_{850} = 10.35 \pm 1.80$ mJy.

In the XMM-LSS field, one of our sources, 500R_XMMLSS.T1.x70, is covered. It actually corresponds to two objects in the S2LS catalog, S2CLS UDS.0074 and 0750, which are $12.''7$ apart and have deboosted $S_{850} = 6.44 \pm 1.26$ and 2.61 ± 0.89 mJy, respectively. As in the case for 500R_COSMOS.T1.x34 above, we combine these two entries and obtain its deboosted $S_{850} = 9.05 \pm 1.54$ mJy.

The S2CLS EGS field covers one of our 500 μm risers, 500R_EGS.T1.x42, which is matched with EGS.0007 and has $S_{850} = 7.28 \pm 0.91$ mJy in the S2CLS catalog.

Three of our objects in the ADFS field, 500R_ADFS.T1.x14, x20 and x28, are covered by the AzTEC 1.1 mm observation of Hatsukade et al. (2011) and are detected. These sources are matched with their cataloged objects AzTEC 27, 4, and 170, respectively.

The above results are summarized in Table 12.

B. FULL CATALOGS OF 500 μM RISERS AND SPIRE DROPOUTS

The Tier 1 catalogs of 500 μm risers and SPIRE dropouts are given as tables below. Their Tier 2 catalogs are provided as online data. The COSMOS and the GOODS-N fields do not have residual-based 500 μm risers (the “R” objects) in either Tier 1 or Tier 2. The EGS and the ELAISN1 fields also do not have residual-based 500 μm risers in Tier 2. The GOODS-N field does not have any Tier 2 SPIRE dropouts.

All catalogs can be obtained as machine-readable tables at the ApJS site, and are also available from the authors upon request (yanha@missouri.edu).

Table 13. Catalog of Tier 1 500 μm risers

ID	RA (degrees)	DEC (degrees)	f_{250} (mJy)	f_{350} (mJy)	f_{500} (mJy)	Radio Code	ID	RA (degrees)	DEC (degrees)	f_{250} (mJy)	f_{350} (mJy)	f_{500} (mJy)	Radio Code
500R_ADFS_T1_x01	72.5177700	-53.9919360	37.6 \pm 4.8	42.9 \pm 5.6	46.0 \pm 5.7	99	x41	72.0953300	-53.0941430	33.1 \pm 4.8	34.1 \pm 5.6	37.1 \pm 5.4	0
x02	73.8549400	-53.6504000	53.1 \pm 4.7	55.0 \pm 5.7	55.8 \pm 5.8	99	x43	69.4404300	-54.5158460	24.6 \pm 4.7	28.9 \pm 5.7	32.1 \pm 6.0	99
x03	73.0416800	-52.8747800	42.4 \pm 4.8	54.5 \pm 5.7	56.5 \pm 6.0	0	x48	70.2323600	-53.5838740	22.0 \pm 4.8	29.1 \pm 5.6	34.4 \pm 5.4	99
x04	71.6428450	-54.3566300	37.5 \pm 4.8	42.0 \pm 5.7	43.5 \pm 6.2	99	x53	68.0292900	-55.2309340	15.8 \pm 4.8	23.2 \pm 5.6	30.9 \pm 6.1	99
x07	69.0860300	-53.8102300	29.7 \pm 4.8	35.3 \pm 5.6	37.1 \pm 5.4	99	R01	69.8040960	-54.4288990	29.1 \pm 4.8	54.3 \pm 5.6	60.4 \pm 5.4	99
x08	69.6321900	-54.2527100	36.1 \pm 4.8	48.9 \pm 5.6	51.0 \pm 5.7	99	R02	73.6183930	-52.1385570	19.5 \pm 5.3	39.1 \pm 6.1	53.2 \pm 6.2	99
x10	73.3981600	-52.9431420	33.6 \pm 4.8	42.9 \pm 5.6	45.5 \pm 5.5	99	R05	71.2906730	-53.0018590	20.7 \pm 4.8	38.3 \pm 5.6	42.0 \pm 5.5	0
x11	70.3567050	-54.2958370	34.7 \pm 4.8	39.5 \pm 5.6	39.7 \pm 5.8	99	R07	69.9738140	-55.1511090	7.5 \pm 5.3	24.1 \pm 6.2	41.0 \pm 6.4	99
x14	71.7467800	-53.3914030	26.3 \pm 4.8	29.4 \pm 5.6	29.6 \pm 5.6	0	R08	73.3624050	-52.5277680	20.7 \pm 4.8	36.3 \pm 5.7	40.2 \pm 5.5	99
x15	72.2722240	-54.1076550	34.1 \pm 4.8	41.4 \pm 5.8	44.2 \pm 7.2	99	R10	73.9366080	-52.9216160	22.5 \pm 4.9	35.4 \pm 5.6	36.9 \pm 5.5	99
x16	68.5898700	-54.5882030	27.3 \pm 4.8	31.9 \pm 5.6	33.2 \pm 5.9	99	R14	71.0967830	-53.4363370	11.6 \pm 4.8	24.8 \pm 5.6	35.3 \pm 5.5	0
x17	73.2279050	-53.0704700	27.6 \pm 4.8	30.4 \pm 5.6	31.3 \pm 5.7	99	R16	67.9182410	-54.0250010	9.0 \pm 5.3	23.1 \pm 6.0	34.6 \pm 6.3	99
x18	72.6491550	-53.2460670	30.1 \pm 4.8	35.8 \pm 5.6	37.9 \pm 5.5	0	R18	73.0194620	-52.0331570	25.1 \pm 5.4	32.2 \pm 6.1	34.3 \pm 6.6	99
x19	73.5484400	-52.7083300	31.4 \pm 4.8	38.8 \pm 5.6	42.8 \pm 5.4	99	R19	67.3707110	-54.1425910	19.5 \pm 5.3	32.3 \pm 5.9	34.2 \pm 6.3	99
x20	71.1698100	-53.7612230	24.9 \pm 4.8	35.5 \pm 5.6	37.1 \pm 5.7	0	R20	71.1480240	-53.2264870	15.9 \pm 4.8	33.0 \pm 5.6	33.8 \pm 5.5	0
x26	72.2347950	-54.1312830	21.7 \pm 4.8	33.1 \pm 5.6	34.0 \pm 5.5	99	R23	68.9597700	-54.5637620	25.2 \pm 4.8	26.4 \pm 5.6	32.2 \pm 5.7	99
x28	70.8641100	-53.7012860	27.3 \pm 4.8	32.1 \pm 5.7	34.0 \pm 5.8	0	R26	73.5431610	-53.3780030	23.6 \pm 4.8	30.7 \pm 5.6	31.6 \pm 5.5	99
x35	67.9800500	-55.1544040	28.2 \pm 4.8	34.5 \pm 5.7	35.1 \pm 6.3	99	R29	73.4149630	-53.0009730	28.9 \pm 4.8	29.8 \pm 5.6	30.5 \pm 5.5	99
x37	69.6234700	-53.6538900	26.9 \pm 4.8	28.5 \pm 5.6	29.0 \pm 5.8	99	R32	74.1133250	-53.1690950	11.7 \pm 4.8	17.5 \pm 5.6	28.6 \pm 5.5	99
x40	69.8740000	-53.7536770	21.1 \pm 4.8	28.1 \pm 5.6	28.7 \pm 5.5	99	R34	71.8686400	-53.5979220	12.5 \pm 4.8	27.1 \pm 5.6	28.3 \pm 5.5	0
500R_CDFS_T1_x004	52.7319600	-28.8153230	47.3 \pm 3.4	59.0 \pm 3.9	60.0 \pm 3.9	1	x176	52.5909230	-27.7079180	17.7 \pm 3.4	19.5 \pm 4.0	27.2 \pm 3.9	0
x007	52.5725400	-27.5764300	37.5 \pm 3.4	37.7 \pm 3.9	45.4 \pm 3.9	0	x177	52.5599670	-28.9544070	23.9 \pm 3.4	25.6 \pm 4.0	36.1 \pm 3.9	99
x009	53.7353200	-29.8309040	39.1 \pm 3.4	47.1 \pm 3.9	48.8 \pm 4.2	99	x178	53.5423740	-28.6750700	16.3 \pm 3.4	25.1 \pm 3.9	30.2 \pm 4.0	0
x011	54.2535060	-29.3634620	34.6 \pm 3.4	48.6 \pm 3.9	55.7 \pm 3.9	99	x180	52.6851580	-28.2588040	16.7 \pm 3.4	23.3 \pm 4.0	28.9 \pm 4.8	0
x015	52.5498120	-28.8914400	36.0 \pm 3.4	44.2 \pm 4.1	56.2 \pm 3.9	0	x183	51.6547130	-28.7698290	16.0 \pm 3.4	21.6 \pm 3.9	26.2 \pm 3.9	1
x020	53.9682850	-30.0772600	29.3 \pm 3.4	34.2 \pm 4.0	39.0 \pm 3.9	99	x184	51.7977260	-29.1630690	21.0 \pm 3.4	21.1 \pm 3.9	22.2 \pm 3.9	99
x021	51.1410870	-29.2218600	36.4 \pm 3.4	40.0 \pm 3.9	55.8 \pm 4.0	99	x186	51.5931850	-29.2047960	19.5 \pm 3.4	23.3 \pm 3.9	26.3 \pm 3.9	99
x023	52.6076800	-27.6362250	28.0 \pm 3.4	28.4 \pm 3.9	41.1 \pm 3.9	1	x187	52.6416660	-27.6620160	17.2 \pm 3.4	21.1 \pm 3.9	21.9 \pm 4.0	1
x024	51.7497900	-29.3143060	26.3 \pm 3.4	34.6 \pm 3.9	38.4 \pm 4.0	99	x188	53.5512770	-27.0338780	19.3 \pm 3.4	25.2 \pm 4.0	25.4 \pm 4.2	99
x025	51.3113560	-29.0133250	33.7 \pm 3.4	34.5 \pm 3.9	42.3 \pm 3.9	99	x189	52.6669650	-27.6229740	20.2 \pm 3.4	24.6 \pm 3.9	29.1 \pm 4.0	0
x026	54.8958100	-27.9312860	24.3 \pm 3.4	28.9 \pm 3.9	29.0 \pm 3.9	99	x190	53.3894160	-27.9915800	16.2 \pm 3.4	24.3 \pm 3.9	28.6 \pm 4.0	0
x028	54.6605300	-28.9603500	22.8 \pm 3.4	31.8 \pm 3.9	33.8 \pm 4.1	99	x192	51.4127400	-29.5066660	23.9 \pm 3.4	29.1 \pm 3.9	31.6 \pm 3.9	99
x030	52.7051050	-28.9989360	26.8 \pm 3.4	32.8 \pm 3.9	34.0 \pm 4.1	99	x193	51.6848200	-28.1811140	19.3 \pm 3.4	21.6 \pm 3.9	21.9 \pm 3.9	1
x034	51.6982420	-28.2527940	28.2 \pm 3.4	40.7 \pm 4.0	44.7 \pm 4.3	0	x194	54.2248600	-28.7390820	12.8 \pm 3.4	19.0 \pm 3.9	23.2 \pm 4.1	99
x036	52.2846260	-26.9746250	31.6 \pm 3.4	42.2 \pm 3.9	44.0 \pm 3.9	99	x196	52.5485100	-29.5002650	18.5 \pm 3.4	20.0 \pm 3.9	20.8 \pm 4.0	99
x037	53.9073680	-28.5219960	30.4 \pm 3.4	35.3 \pm 4.0	36.2 \pm 5.4	0	x198	52.4261300	-29.4327550	13.2 \pm 3.4	21.2 \pm 4.0	22.8 \pm 4.3	99

Table 13 continued

Table 13 (*continued*)

ID	RA (degrees)	DEC (degrees)	f_{250} (mJy)	f_{350} (mJy)	f_{500} (mJy)	Radio Code	ID	RA (degrees)	DEC (degrees)	f_{250} (mJy)	f_{350} (mJy)	f_{500} (mJy)	Radio Code
x038	52.5739630	-27.7930930	26.3 ± 3.4	31.1 ± 4.0	37.7 ± 4.0	0	x199	51.1902900	-29.1488950	17.5 ± 3.4	19.6 ± 3.9	20.9 ± 4.0	99
x040	53.4226760	-26.3876440	26.6 ± 3.5	28.1 ± 3.9	31.9 ± 4.1	99	x203	53.0208360	-26.9755040	13.2 ± 3.4	22.6 ± 3.9	24.9 ± 3.9	99
x043	53.2791670	-30.1495480	26.9 ± 3.4	37.3 ± 3.9	41.0 ± 4.0	99	x204	54.8569070	-27.4803600	19.5 ± 3.4	21.4 ± 3.9	22.1 ± 4.0	99
x048	52.9007600	-27.9130730	21.1 ± 3.5	24.6 ± 3.9	27.9 ± 4.2	0	x205	51.0237460	-29.32339080	11.3 ± 3.4	13.4 ± 3.9	22.6 ± 3.9	99
x050	53.2634960	-29.9049190	26.8 ± 3.4	33.2 ± 3.9	34.6 ± 3.9	99	x206	54.5963400	-29.6491370	14.9 ± 3.4	17.6 ± 3.9	20.5 ± 4.0	99
x052	52.7254260	-30.0157200	21.5 ± 3.4	21.9 ± 4.0	23.6 ± 4.0	99	x207	53.8339200	-29.2509290	21.0 ± 3.4	27.8 ± 3.9	33.6 ± 4.2	99
x053	51.4428440	-29.5194020	35.5 ± 3.4	43.0 ± 3.9	47.5 ± 4.0	99	x208	51.2654150	-29.4699650	23.0 ± 3.4	29.6 ± 4.1	30.5 ± 3.9	99
x055	53.2145700	-26.3998580	29.9 ± 3.5	32.0 ± 4.0	33.5 ± 4.5	99	x209	53.6398430	-26.8464700	15.6 ± 3.4	25.4 ± 3.9	26.0 ± 4.0	99
x056	53.5557020	-29.3240950	24.3 ± 3.4	33.6 ± 4.1	38.6 ± 4.2	99	x210	54.2329600	-29.1523230	17.1 ± 3.4	20.5 ± 3.9	21.6 ± 4.0	99
x058	52.4616200	-27.4895670	25.5 ± 3.4	25.6 ± 3.9	25.9 ± 4.2	0	x211	52.6299900	-27.7940620	15.9 ± 3.4	25.3 ± 3.9	31.1 ± 3.9	0
x059	51.5431060	-28.2829880	23.7 ± 3.4	30.1 ± 3.9	30.6 ± 4.2	99	x212	54.1848200	-26.9562440	15.0 ± 3.4	19.2 ± 3.9	19.9 ± 3.9	99
x063	51.1669800	-28.4947400	14.6 ± 3.4	25.4 ± 4.0	30.3 ± 4.2	99	x213	54.2337760	-28.7861860	16.0 ± 3.4	18.5 ± 3.9	21.3 ± 3.9	99
x065	54.4068150	-29.2127530	21.1 ± 3.4	28.8 ± 3.9	28.9 ± 4.1	99	x217	54.8097600	-28.4938720	8.7 ± 3.4	18.6 ± 3.9	20.3 ± 3.9	99
x066	52.6915320	-29.0121420	22.8 ± 3.4	31.4 ± 3.9	33.3 ± 3.9	99	x218	51.5767440	-28.3484880	15.0 ± 3.4	21.1 ± 4.0	26.2 ± 4.0	99
x067	51.3506160	-27.5122490	28.9 ± 3.4	36.9 ± 3.9	37.3 ± 4.2	99	x219	52.3446800	-26.9536880	17.7 ± 3.4	19.0 ± 3.9	25.0 ± 4.0	99
x068	51.4468300	-26.9354320	17.3 ± 3.4	20.4 ± 3.9	25.0 ± 3.9	99	x220	51.1491900	-29.1442620	12.6 ± 3.4	22.2 ± 3.9	23.5 ± 3.9	99
x070	51.5362430	-29.1326540	23.8 ± 3.4	25.3 ± 3.9	26.0 ± 3.9	99	x224	52.3393700	-26.9944200	15.9 ± 3.4	22.6 ± 3.9	32.8 ± 4.0	99
x071	52.0971450	-29.2917040	12.5 ± 3.4	19.5 ± 3.9	24.5 ± 4.3	99	x225	53.1949000	-28.9455590	15.7 ± 3.4	22.3 ± 3.9	22.8 ± 4.1	99
x072	54.8995820	-26.8342900	25.5 ± 3.4	34.9 ± 3.9	36.2 ± 4.0	99	x232	53.9821740	-30.0659900	24.0 ± 3.4	29.1 ± 3.9	37.8 ± 3.9	99
x075	51.5190200	-27.1231230	22.5 ± 3.4	23.8 ± 3.9	27.0 ± 4.0	99	x234	53.9575080	-27.9086760	19.9 ± 3.4	24.1 ± 3.9	27.7 ± 4.0	99
x076	52.0472950	-26.1498370	20.1 ± 3.4	27.0 ± 4.0	33.3 ± 5.3	99	x235	53.0917320	-30.0858940	20.3 ± 3.4	23.9 ± 3.9	31.0 ± 3.9	99
x077	54.6550700	-29.2009100	16.0 ± 3.4	19.8 ± 4.0	26.7 ± 4.7	99	x236	51.6024360	-29.5118540	21.2 ± 3.4	28.2 ± 3.9	28.9 ± 4.0	99
x078	53.9950800	-29.4863050	29.0 ± 3.4	42.0 ± 3.9	46.2 ± 4.1	99	x237	52.9581900	-28.9786070	20.7 ± 3.4	26.3 ± 3.9	27.2 ± 4.1	99
x086	54.8163200	-26.6703660	27.6 ± 3.4	32.3 ± 3.9	33.2 ± 4.1	99	x240	51.7187540	-28.5580480	11.5 ± 3.4	20.1 ± 3.9	23.9 ± 4.0	0
x092	52.0868450	-26.8624900	26.3 ± 3.4	33.5 ± 3.9	34.0 ± 3.9	99	x243	52.1575400	-29.3072570	14.9 ± 3.4	19.1 ± 3.9	29.4 ± 4.1	99
x096	54.5722730	-27.9654900	17.1 ± 3.4	21.7 ± 4.0	22.8 ± 3.9	99	x246	51.8032800	-27.8684310	17.4 ± 3.4	29.9 ± 4.0	36.6 ± 4.6	0
x098	51.4810000	-26.6054290	17.3 ± 3.4	25.3 ± 4.0	31.2 ± 4.1	99	x247	51.9136900	-27.2171820	14.2 ± 3.4	17.7 ± 3.9	21.0 ± 4.0	99
x099	53.7805700	-30.2361530	18.5 ± 3.4	24.3 ± 3.9	25.3 ± 4.0	99	x252	51.6748960	-29.7964900	18.7 ± 3.4	33.9 ± 4.0	34.5 ± 3.9	99
x101	51.9685400	-27.1321140	20.5 ± 3.4	21.1 ± 3.9	21.8 ± 4.0	99	x257	53.3595400	-26.6043170	11.0 ± 3.4	17.6 ± 4.0	26.4 ± 4.7	99
x103	54.2743900	-29.6487300	18.3 ± 3.4	18.7 ± 3.9	21.9 ± 4.1	99	x261	54.6149370	-26.8073750	17.8 ± 3.4	27.7 ± 3.9	28.5 ± 4.1	99
x104	53.3980830	-28.6924230	18.4 ± 3.4	25.2 ± 3.9	26.0 ± 3.9	1	x262	54.0569230	-28.5717660	14.1 ± 3.4	19.2 ± 3.9	21.4 ± 3.9	99
x107	52.3968930	-27.6564980	24.0 ± 3.4	29.1 ± 3.9	36.0 ± 3.9	1	x267	54.4151950	-29.6465550	15.7 ± 3.4	25.0 ± 4.0	28.9 ± 4.6	99
x115	52.4333720	-29.8354240	19.0 ± 3.4	31.6 ± 3.9	36.2 ± 4.1	99	x268	53.5648000	-27.9012340	13.6 ± 3.4	19.6 ± 3.9	21.4 ± 4.0	0
x116	53.9837760	-29.6162300	19.4 ± 3.4	22.3 ± 4.1	27.9 ± 5.3	99	x274	53.4732740	-29.0672780	15.0 ± 3.4	23.7 ± 3.9	25.7 ± 4.2	99
x117	54.9789620	-27.2803650	21.4 ± 3.4	26.5 ± 3.9	27.4 ± 4.0	99	x280	53.5963100	-29.8118780	16.9 ± 3.4	21.9 ± 3.9	23.7 ± 4.3	99
x118	53.4985160	-28.4658930	21.7 ± 3.4	27.7 ± 3.9	27.9 ± 3.9	0	x282	52.4446120	-27.3647380	11.5 ± 3.4	21.9 ± 3.9	24.7 ± 3.9	1
x119	52.6982420	-28.1717600	20.5 ± 3.4	24.6 ± 3.9	25.8 ± 4.2	0	x284	52.5372120	-27.7062230	12.2 ± 3.4	20.9 ± 4.0	32.1 ± 4.0	0
x123	51.4113900	-29.3688700	31.7 ± 3.4	33.5 ± 3.9	37.7 ± 4.1	99	R02	53.3198670	-26.3801330	31.0 ± 3.9	33.6 ± 4.4	42.7 ± 4.5	99
x124	51.5114300	-28.1846680	26.7 ± 3.4	28.0 ± 3.9	33.5 ± 4.1	0	R03	54.0044690	-26.5067550	29.9 ± 3.9	39.7 ± 4.3	41.3 ± 4.4	99

Table 13 *continued*

Table 13 (continued)

32

ID	RA (degrees)	DEC (degrees)	f_{250} (mJy)	f_{350} (mJy)	f_{500} (mJy)	Radio Code	ID	RA (degrees)	DEC (degrees)	f_{250} (mJy)	f_{350} (mJy)	f_{500} (mJy)	Radio Code
x129	53.1585120	-26.3664720	23.6 ± 3.4	26.7 ± 3.9	26.7 ± 4.1	99	R05	54.1006610	-30.1577090	28.1 ± 3.6	33.0 ± 4.1	37.8 ± 4.2	99
x134	52.5857200	-28.3420890	17.6 ± 3.4	22.2 ± 3.9	22.7 ± 3.9	0	R07	54.1150170	-30.3027000	16.3 ± 4.2	25.7 ± 4.5	31.5 ± 4.8	99
x135	54.0591500	-27.5316410	18.9 ± 3.4	19.2 ± 4.0	23.1 ± 4.5	99	R09	51.4714540	-27.6863530	20.9 ± 3.7	26.9 ± 4.1	30.4 ± 4.4	99
x137	51.0864940	-29.6473880	21.1 ± 3.4	33.9 ± 3.9	39.6 ± 4.2	99	R14	52.4582260	-27.4341000	12.6 ± 3.4	21.3 ± 3.9	26.8 ± 3.9	0
x139	53.9368970	-27.8885750	21.1 ± 3.4	24.5 ± 4.0	27.6 ± 4.5	99	R17	51.6275480	-29.3989370	14.5 ± 3.4	23.8 ± 3.8	25.1 ± 3.9	99
x142	53.9128230	-29.5150570	19.8 ± 3.4	24.4 ± 4.0	25.9 ± 4.3	99	R18	52.7229700	-26.2976610	13.4 ± 3.7	17.5 ± 4.0	24.9 ± 4.2	99
x148	52.2252600	-29.5673200	22.5 ± 3.4	33.2 ± 3.9	35.4 ± 4.1	99	R24	54.2990110	-28.2041550	15.3 ± 3.4	19.8 ± 3.8	23.2 ± 3.9	99
x149	51.5961040	-29.0586430	20.0 ± 3.4	26.1 ± 3.9	30.5 ± 4.1	99	R27	52.6959460	-28.6623530	15.1 ± 3.4	20.9 ± 3.9	22.8 ± 4.0	0
x152	52.6246760	-26.5163860	18.6 ± 3.4	23.9 ± 4.1	33.9 ± 4.6	99	R28	52.4562680	-26.8329900	11.6 ± 3.4	22.2 ± 3.9	22.7 ± 4.0	99
x155	51.4627530	-26.9218830	18.4 ± 3.4	25.9 ± 3.9	26.7 ± 4.1	99	R30	53.7278140	-27.0302200	14.8 ± 3.4	20.9 ± 3.9	22.4 ± 4.0	99
x162	52.6515000	-26.7467480	18.1 ± 3.4	23.2 ± 4.0	23.9 ± 4.0	99	R32	53.9888420	-27.9607340	9.6 ± 3.4	17.7 ± 3.8	22.0 ± 4.0	0
x166	51.7917800	-28.3055460	19.5 ± 3.4	20.7 ± 3.9	22.3 ± 4.2	0	R33	54.0377730	-27.8183910	11.6 ± 3.4	19.1 ± 3.8	21.7 ± 3.9	99
x170	52.7494700	-28.8928720	18.2 ± 3.4	18.7 ± 3.9	20.9 ± 4.1	0	R37	52.8901080	-26.8169130	9.5 ± 3.4	15.5 ± 3.9	20.6 ± 3.9	99
x171	51.8051600	-26.9355130	19.8 ± 3.4	22.9 ± 4.0	26.1 ± 4.5	99	R40	52.0725410	-29.7677250	11.1 ± 3.5	16.8 ± 3.9	20.1 ± 4.0	99
x175	53.0619540	-26.8791300	14.4 ± 3.4	19.4 ± 4.0	27.5 ± 4.5	99	R41	53.7388600	-29.7164060	15.2 ± 3.4	17.6 ± 3.8	19.8 ± 4.0	99
500R_COSMOS_T1_x01	149.8404500	1.7941180	18.1 ± 3.4	24.9 ± 6.6	26.2 ± 5.1	1	x22	151.0009900	1.6792000	17.1 ± 3.4	28.7 ± 6.5	30.9 ± 5.0	0
x02	150.4261300	2.0053530	18.8 ± 3.4	23.8 ± 6.6	26.4 ± 5.0	0	x23	150.4910300	1.7460680	25.2 ± 3.4	29.1 ± 6.6	31.1 ± 5.2	1
x04	150.7384800	1.7167940	21.5 ± 3.4	27.1 ± 6.6	27.2 ± 5.1	0	x24	150.6682600	1.7611610	19.2 ± 3.4	24.5 ± 6.6	31.4 ± 5.2	1
x05	150.4101900	2.6267820	23.6 ± 3.4	23.8 ± 6.6	27.4 ± 5.0	1	x25	150.0729700	1.9746080	13.8 ± 3.4	21.8 ± 6.6	31.4 ± 5.3	1
x07	150.7576800	1.6521520	21.1 ± 3.4	27.8 ± 6.6	27.9 ± 5.2	1	x26	150.2456400	1.5524390	13.4 ± 3.4	21.1 ± 6.6	32.2 ± 5.1	1
x08	150.4257700	2.6241420	23.5 ± 3.4	25.4 ± 6.6	28.1 ± 5.0	1	x29	150.2241400	1.2151000	22.7 ± 3.4	31.3 ± 6.6	35.3 ± 5.2	0
x09	149.9419400	3.0635480	18.5 ± 3.4	27.3 ± 6.6	28.1 ± 5.3	0	x31	150.3587600	1.9640030	20.0 ± 3.4	26.3 ± 6.6	36.0 ± 5.2	1
x10	150.4185300	2.5040790	24.0 ± 3.4	26.3 ± 6.6	28.3 ± 5.2	0	x32	151.2334000	1.5128880	30.4 ± 3.4	34.6 ± 6.7	36.2 ± 5.6	0
x13	149.6910700	2.7247700	23.9 ± 3.4	28.4 ± 6.6	28.6 ± 5.1	1	x34	150.0410300	2.3727840	31.4 ± 3.4	35.0 ± 6.6	39.8 ± 5.1	0
x14	150.7497300	3.2002590	20.1 ± 3.4	25.5 ± 6.6	28.9 ± 5.6	0	x35	149.3146000	1.8588260	32.3 ± 3.4	34.6 ± 6.6	41.0 ± 5.0	0
x16	149.3423500	1.8230420	24.3 ± 3.4	26.6 ± 6.6	28.9 ± 5.0	0	x36	149.9280100	3.2734710	37.7 ± 3.4	43.7 ± 6.6	44.1 ± 5.0	0
x20	150.3911300	3.2064280	15.3 ± 3.4	22.1 ± 6.6	30.5 ± 5.1	0	x38	150.8306900	1.4414390	26.9 ± 3.4	42.4 ± 6.6	47.0 ± 5.0	0
x21	149.3446500	2.6189590	25.6 ± 3.4	30.7 ± 6.6	30.8 ± 5.0	0							
500R_EGS_T1_x03	216.5585600	53.9789350	29.9 ± 3.6	34.7 ± 4.1	36.0 ± 4.3	99	x27	216.0079800	53.3887020	15.2 ± 3.5	21.6 ± 4.1	22.0 ± 4.4	1
x05	214.1281100	51.4164900	21.0 ± 3.5	21.5 ± 4.1	21.7 ± 4.2	99	x30	214.7403400	51.9318900	14.7 ± 3.5	22.0 ± 4.1	22.5 ± 4.5	99
x07	213.9541000	51.4231260	23.4 ± 3.5	26.4 ± 4.2	26.6 ± 5.0	99	x32	216.3026400	53.9945680	20.9 ± 3.6	29.6 ± 4.1	33.9 ± 4.3	99
x08	215.1040800	53.3255160	22.3 ± 3.5	31.4 ± 4.1	33.0 ± 4.4	0	x33	214.9982100	52.5651320	16.1 ± 3.5	25.1 ± 4.1	28.7 ± 4.3	99
x09	215.3185300	52.8410150	22.3 ± 3.5	22.4 ± 4.2	25.0 ± 4.6	0	x36	216.0300900	53.2989540	16.3 ± 3.5	24.3 ± 4.1	29.1 ± 4.3	0
x10	215.6385000	53.2386200	27.4 ± 3.5	42.5 ± 4.1	44.0 ± 4.3	1	x38	216.1635400	53.3102460	15.4 ± 3.5	21.9 ± 4.1	24.3 ± 4.3	99
x11	214.4943200	52.0634600	23.4 ± 3.5	27.5 ± 4.1	29.1 ± 4.4	99	x39	213.1064600	51.6999300	15.8 ± 3.5	21.8 ± 4.1	27.8 ± 4.4	99
x12	215.9491600	52.8048970	20.0 ± 3.5	25.2 ± 4.1	25.6 ± 4.5	99	x41	216.5895700	53.4528400	13.3 ± 3.5	24.6 ± 4.2	35.2 ± 4.5	99
x15	215.8743000	53.0961600	22.2 ± 3.5	32.0 ± 4.1	38.9 ± 4.4	99	x42	214.6202700	52.6815870	16.0 ± 3.5	22.8 ± 4.1	27.1 ± 4.5	0
x19	216.2766400	53.6971320	22.9 ± 3.5	29.9 ± 4.2	31.0 ± 4.8	99	x45	215.9670300	53.5852850	14.8 ± 3.5	21.2 ± 4.1	23.3 ± 4.3	0
x20	214.0929100	51.8842430	19.2 ± 3.5	30.6 ± 4.1	35.7 ± 4.7	99	x46	214.4893600	52.8088150	15.7 ± 3.5	21.5 ± 4.2	24.0 ± 4.8	0

Table 13 continued

Table 13 (continued)

ID	RA (degrees)	DEC (degrees)	f_{250} (mJy)	f_{350} (mJy)	f_{500} (mJy)	Radio Code	ID	RA (degrees)	DEC (degrees)	f_{250} (mJy)	f_{350} (mJy)	f_{500} (mJy)	Radio Code
x24	216.2123900	53.8251340	21.7 ± 3.5	26.3 ± 4.2	26.4 ± 4.3	99	R1	213.9066360	52.6572320	21.3 ± 3.7	33.6 ± 4.2	34.6 ± 4.5	99
x26	214.0280600	52.7272830	21.4 ± 3.5	23.8 ± 4.1	26.4 ± 4.5	99	R2	214.4268210	51.7150490	22.9 ± 3.6	30.4 ± 4.1	31.3 ± 4.4	99
500R_ELAINI_T1_x001	242.7039200	56.2591500	115.1 ± 4.3	164.9 ± 5.1	170.7 ± 5.1	0	x062	241.3792700	54.9484800	23.7 ± 4.3	26.0 ± 5.1	32.9 ± 5.1	0
x003	242.1348600	53.9311030	37.1 ± 4.3	49.7 ± 5.1	51.1 ± 5.3	0	x064	243.9905700	55.4108700	23.4 ± 4.3	29.6 ± 5.3	35.7 ± 5.9	0
x004	243.4325300	55.7518350	42.1 ± 4.3	51.5 ± 5.1	55.2 ± 4.9	0	x068	243.1342200	55.7191050	21.2 ± 4.3	24.9 ± 5.1	28.0 ± 5.0	0
x006	239.1006800	54.7868000	36.7 ± 4.3	48.3 ± 5.2	51.2 ± 5.8	99	x070	243.1609300	55.6348700	31.1 ± 4.3	35.4 ± 5.1	40.9 ± 5.2	0
x008	244.0415600	55.2608380	40.4 ± 4.3	50.2 ± 5.1	55.2 ± 4.9	0	x071	242.5957000	57.1425800	18.8 ± 4.3	25.0 ± 5.1	27.8 ± 4.9	99
x009	244.6938200	54.8193170	37.0 ± 4.3	42.1 ± 5.2	43.1 ± 5.0	0	x073	239.7578000	54.8806900	18.3 ± 4.3	22.7 ± 5.2	25.2 ± 4.9	99
x012	241.2710300	55.3460660	26.4 ± 4.2	27.7 ± 5.1	31.1 ± 5.1	0	x075	244.4383100	54.0328600	22.5 ± 4.3	28.0 ± 5.5	38.9 ± 5.1	0
x014	246.0013900	55.1751900	34.6 ± 4.3	43.4 ± 5.1	45.0 ± 5.1	99	x078	243.1582500	56.4281300	24.2 ± 4.3	38.6 ± 5.2	40.0 ± 5.8	0
x016	239.5892300	55.4060100	31.6 ± 4.4	51.9 ± 5.1	66.1 ± 5.0	99	x079	242.3164500	53.8282280	23.1 ± 4.3	35.7 ± 5.1	36.0 ± 5.1	0
x020	243.9223000	56.4000360	33.2 ± 4.3	35.0 ± 5.1	35.7 ± 4.9	99	x081	242.2225800	54.9060130	16.3 ± 4.3	21.3 ± 5.1	29.8 ± 5.2	0
x025	243.4413900	56.1078100	25.5 ± 4.3	31.3 ± 5.3	36.9 ± 5.7	0	x082	244.3308700	54.6205520	22.9 ± 4.3	25.2 ± 5.1	28.2 ± 5.2	0
x026	240.3003700	55.1443820	30.5 ± 4.3	32.1 ± 5.1	37.6 ± 5.0	0	x083	242.1376600	55.3718220	14.9 ± 4.3	25.4 ± 5.1	29.3 ± 5.0	0
x028	242.7136400	53.9555900	22.8 ± 4.3	26.9 ± 5.1	27.4 ± 5.0	0	x087	244.7988300	54.0676540	24.0 ± 4.3	24.4 ± 5.1	27.9 ± 5.5	0
x031	242.7473900	55.1347920	25.7 ± 4.3	32.5 ± 5.1	32.6 ± 4.9	0	x091	241.4371600	53.7267150	15.4 ± 4.3	26.2 ± 5.2	28.6 ± 5.3	0
x032	245.6210800	55.9797940	24.3 ± 4.3	36.9 ± 5.3	38.2 ± 5.8	99	x093	244.0140000	54.8528440	13.7 ± 4.3	25.7 ± 5.1	34.0 ± 4.9	0
x033	240.2582000	54.3189700	28.1 ± 4.3	28.6 ± 5.1	36.5 ± 5.5	0	x096	243.9840100	56.3520770	23.1 ± 4.3	29.6 ± 5.1	33.0 ± 5.0	99
x038	244.8977800	54.7465480	26.2 ± 4.3	33.5 ± 5.1	35.8 ± 4.9	0	x099	240.4714200	54.4069440	19.1 ± 4.3	24.5 ± 5.1	25.3 ± 4.9	0
x044	241.4639600	54.2210240	25.1 ± 4.3	34.7 ± 5.1	35.0 ± 5.0	0	x101	242.9226400	53.2643470	17.6 ± 4.3	25.3 ± 5.1	26.7 ± 5.0	99
x045	242.6650700	56.3330150	24.9 ± 4.3	36.7 ± 5.2	39.5 ± 5.2	0	x103	242.4475600	55.4198760	14.1 ± 4.3	25.0 ± 5.1	25.9 ± 5.0	0
x053	244.3956600	54.2975900	19.1 ± 4.3	21.5 ± 5.2	28.4 ± 5.0	0	R1	243.6432840	56.9892240	0.0 ± 7.5	19.2 ± 7.6	45.4 ± 8.8	99
x054	243.3606700	54.4348560	22.5 ± 4.3	39.0 ± 5.1	48.9 ± 5.0	0	R2	242.1018860	53.2652100	11.7 ± 6.4	34.6 ± 6.5	45.1 ± 7.1	99
x056	241.6858700	55.7780720	20.0 ± 4.3	28.1 ± 5.1	28.9 ± 5.1	0	R3	242.0944510	57.2992760	22.3 ± 7.7	38.9 ± 8.2	44.9 ± 8.8	99
x057	243.4121400	54.6986160	14.6 ± 4.3	21.0 ± 5.1	27.6 ± 5.2	0	R4	239.9017060	55.3027900	0.0 ± 6.1	2.6 ± 6.6	41.2 ± 7.0	99
x059	240.4498300	53.9934120	22.6 ± 4.3	28.7 ± 5.1	30.5 ± 5.1	99	R5	243.8106840	53.2725060	11.7 ± 6.1	18.2 ± 6.6	39.5 ± 7.0	99
x060	243.2105000	54.4390680	21.5 ± 4.3	31.6 ± 5.1	33.8 ± 5.2	0	R7	242.2207620	56.8871230	4.4 ± 6.1	17.2 ± 6.5	35.5 ± 6.9	99
x061	244.6767600	55.7831340	27.1 ± 4.3	39.9 ± 5.2	40.8 ± 5.2	0							
500R_ELAIN2_T1_x01	249.4733100	39.8209400	63.2 ± 5.0	88.1 ± 26.1	90.4 ± 6.0	99	x38	251.0744200	40.7094350	25.5 ± 4.9	34.1 ± 26.1	34.9 ± 5.9	0
x02	247.5254400	41.4275700	54.5 ± 5.0	61.0 ± 26.1	65.8 ± 6.1	0	x43	247.8864000	41.1780700	26.2 ± 5.0	28.3 ± 26.1	32.8 ± 6.0	0
x03	249.8164200	41.4753460	47.0 ± 5.0	55.5 ± 26.1	64.8 ± 6.0	1	x45	249.1655300	40.1143070	16.1 ± 5.0	26.9 ± 26.1	31.4 ± 6.0	0
x04	248.5108300	41.1363950	41.8 ± 5.0	50.7 ± 26.1	52.5 ± 5.9	0	x49	249.1930500	40.2439000	22.9 ± 5.0	33.8 ± 26.1	36.6 ± 6.0	1
x06	249.4193700	39.8774100	37.4 ± 4.9	41.0 ± 26.2	46.9 ± 7.3	99	x51	249.3868600	41.3875960	16.5 ± 5.0	33.9 ± 26.2	34.1 ± 6.4	0
x07	249.7083400	42.0200420	41.5 ± 4.9	42.9 ± 26.1	48.8 ± 5.9	0	R04	251.1321420	41.6944960	23.4 ± 5.5	37.8 ± 26.2	51.8 ± 6.5	99
x08	249.7570500	41.7758330	40.2 ± 5.0	47.2 ± 26.1	48.3 ± 6.2	0	R05	248.2254880	40.3192730	25.8 ± 5.1	42.2 ± 26.1	46.9 ± 5.8	0
x09	250.6436500	40.9340480	37.0 ± 4.9	41.9 ± 26.1	42.7 ± 6.2	0	R06	247.4879430	41.3421870	23.6 ± 5.2	35.3 ± 26.2	44.7 ± 6.0	0
x12	248.7276300	41.4133200	33.3 ± 4.9	43.4 ± 26.1	44.4 ± 6.0	0	R07	250.4821820	41.4370100	17.9 ± 5.0	28.2 ± 26.2	43.3 ± 5.9	0
x18	249.8772300	40.7988550	27.9 ± 4.9	30.4 ± 26.1	31.2 ± 6.0	0	R08	248.3821020	40.4918350	35.5 ± 5.0	40.6 ± 26.1	43.0 ± 5.9	0
x19	248.9647400	41.3401070	29.5 ± 5.0	34.9 ± 26.1	38.2 ± 6.0	0	R11	251.1406140	41.9976880	20.1 ± 5.8	35.4 ± 26.3	39.8 ± 7.0	99

Table 13 continued

Table 13 (continued)

ID	RA (degrees)	DEC (degrees)	f_{250} (mJy)	f_{350} (mJy)	f_{500} (mJy)	Radio Code	ID	RA (degrees)	DEC (degrees)	f_{250} (mJy)	f_{350} (mJy)	f_{500} (mJy)	Radio Code
x20	250.9758600	40.9618300	26.4 ± 5.0	32.3 ± 26.2	38.2 ± 5.9	0	R14	249.5857170	42.4655940	26.7 ± 5.7	35.0 ± 26.3	37.3 ± 6.5	99
x24	248.0347000	40.0041770	24.8 ± 5.0	25.5 ± 26.1	32.6 ± 5.9	0	R15	248.7851350	41.3051660	26.7 ± 5.0	35.9 ± 26.1	37.3 ± 5.8	0
x27	250.1509900	40.2990650	24.2 ± 5.0	43.8 ± 26.2	45.0 ± 5.9	0	R17	247.9022540	40.3007140	14.2 ± 5.0	34.4 ± 26.1	35.0 ± 5.9	0
x28	249.2099900	40.8414100	25.7 ± 5.0	27.5 ± 26.2	33.6 ± 6.4	0	R21	249.3005430	39.8004150	20.5 ± 5.5	27.2 ± 26.3	33.6 ± 6.5	99
x30	247.5463000	40.8246880	26.0 ± 5.0	32.8 ± 26.1	33.4 ± 6.0	0	R23	250.7459520	42.0942440	24.3 ± 5.5	28.2 ± 26.3	32.9 ± 6.5	99
x31	248.5687100	40.4128880	27.3 ± 5.0	33.5 ± 26.2	35.0 ± 6.2	0	R27	248.6041940	41.1328820	8.9 ± 5.0	28.3 ± 26.1	31.4 ± 5.9	0
x33	248.7289700	39.6258620	26.2 ± 5.0	32.8 ± 26.1	35.8 ± 6.1	0	R28	248.8744920	41.8146970	10.5 ± 5.0	22.8 ± 26.2	29.8 ± 5.8	0
x35	251.4622800	40.8737400	29.9 ± 4.9	33.1 ± 26.1	36.9 ± 6.3	99	R29	250.6316540	41.0494160	14.9 ± 5.0	25.6 ± 26.1	29.6 ± 5.9	0
x36	248.8387500	41.2397900	28.1 ± 4.9	49.1 ± 26.2	53.8 ± 7.1	0							
500R_ELAISS1_T1_x01	7.5730430	-42.4126740	55.3 ± 4.0	72.2 ± 4.9	92.8 ± 4.9	99	x54	9.4041210	-45.0392900	20.7 ± 4.0	24.4 ± 4.9	25.9 ± 4.7	99
x02	8.1660870	-42.9165570	41.8 ± 4.0	42.4 ± 4.9	44.8 ± 4.8	0	x55	7.8442540	-43.6858440	20.5 ± 4.0	25.6 ± 4.9	26.6 ± 4.7	0
x03	8.5301780	-45.3173830	37.5 ± 4.0	38.2 ± 4.9	38.8 ± 4.7	99	x58	9.3514700	-42.0054970	25.9 ± 4.0	31.0 ± 4.9	33.5 ± 4.9	99
x04	10.1632980	-44.4283940	37.8 ± 4.0	50.5 ± 4.9	52.6 ± 4.7	99	x61	9.2115210	-44.2211270	18.3 ± 4.0	19.1 ± 4.9	24.0 ± 4.7	0
x05	9.7355060	-42.3740040	40.6 ± 4.1	44.3 ± 5.0	44.7 ± 5.8	99	x63	7.2704830	-42.0204350	19.3 ± 4.1	21.6 ± 4.8	27.6 ± 5.1	99
x07	10.3368040	-45.1218450	31.0 ± 4.1	32.8 ± 4.9	33.3 ± 5.9	99	x71	9.6303930	-43.1631500	18.1 ± 4.0	23.6 ± 4.9	25.2 ± 4.7	0
x10	7.2784800	-43.2463500	34.1 ± 4.0	38.0 ± 4.9	38.5 ± 5.1	99	x72	9.4046820	-44.3142780	20.7 ± 4.0	33.3 ± 4.9	35.3 ± 4.8	0
x14	7.0078160	-42.8157420	28.6 ± 4.0	36.0 ± 4.9	36.9 ± 4.8	99	x76	7.4539890	-43.6200640	21.4 ± 4.0	25.7 ± 5.0	28.1 ± 5.0	0
x16	10.1881420	-44.2214850	31.3 ± 4.0	34.5 ± 4.9	48.8 ± 4.7	99	x77	10.2519650	-43.3964200	15.5 ± 4.0	21.0 ± 4.9	25.1 ± 4.7	99
x17	10.1256450	-44.6077800	27.1 ± 4.0	34.3 ± 4.9	34.8 ± 4.7	99	x79	9.3473050	-42.2357750	17.2 ± 4.0	24.0 ± 5.0	26.8 ± 5.2	99
x18	8.1500240	-44.1745760	39.7 ± 4.0	52.0 ± 4.9	53.3 ± 4.7	0	x80	9.8358310	-42.7884500	17.1 ± 4.0	23.3 ± 4.9	28.5 ± 4.7	99
x19	10.1535900	-42.5922130	27.5 ± 4.1	39.1 ± 5.0	43.2 ± 5.4	99	x81	10.2929060	-44.8402000	11.1 ± 4.0	20.8 ± 4.9	29.1 ± 4.7	99
x20	7.9792860	-42.3241420	32.9 ± 4.0	33.9 ± 4.9	35.1 ± 4.7	99	x84	7.5880940	-44.3231280	18.2 ± 4.1	21.6 ± 4.9	25.9 ± 4.6	0
x21	8.3067740	-42.5121300	31.0 ± 4.0	43.0 ± 4.8	49.0 ± 4.7	99	x85	8.3485720	-43.2133900	15.5 ± 4.0	21.9 ± 4.9	25.4 ± 4.7	0
x22	7.2142690	-43.2308920	26.1 ± 4.0	42.6 ± 4.9	45.0 ± 4.6	99	x86	10.4253850	-43.5782000	12.6 ± 4.0	23.1 ± 5.0	27.9 ± 5.2	99
x23	8.7997690	-42.7559800	30.3 ± 4.0	42.4 ± 4.9	46.7 ± 4.7	99	x89	9.7820820	-42.8376430	10.2 ± 4.0	19.2 ± 4.9	24.1 ± 4.7	99
x25	8.3177230	-44.6524800	25.8 ± 4.0	26.4 ± 4.9	27.4 ± 4.9	99	R01	8.6933630	-45.2360340	22.9 ± 4.5	37.2 ± 5.2	46.5 ± 5.2	99
x26	8.0315080	-43.7848700	31.0 ± 4.0	34.0 ± 4.9	37.2 ± 5.0	0	R03	8.3605230	-45.1390240	16.6 ± 4.5	31.1 ± 5.3	40.9 ± 5.2	99
x29	8.9446150	-42.1464000	23.2 ± 4.0	27.5 ± 4.9	29.2 ± 4.7	99	R04	9.0633750	-42.1772970	17.2 ± 4.5	26.8 ± 5.2	40.0 ± 5.2	99
x31	6.9647380	-42.5789900	26.7 ± 4.0	26.9 ± 4.9	28.7 ± 5.0	99	R05	9.1488110	-42.2212520	23.9 ± 4.5	35.9 ± 5.2	38.6 ± 5.2	99
x32	8.5753560	-42.4578970	21.1 ± 4.0	23.0 ± 4.9	25.4 ± 4.9	99	R06	10.5404570	-43.1401360	23.3 ± 5.5	36.9 ± 5.8	38.2 ± 6.4	99
x34	9.3138850	-42.5712000	22.9 ± 4.0	23.8 ± 4.9	24.1 ± 4.7	99	R07	8.6181960	-45.3151390	21.7 ± 4.7	37.2 ± 5.2	37.6 ± 5.3	99
x37	7.7280140	-43.7831000	22.9 ± 4.0	23.7 ± 4.9	26.6 ± 4.9	0	R08	10.4440930	-42.7699610	21.6 ± 4.5	35.4 ± 5.2	36.8 ± 5.1	99
x38	9.9900390	-43.6213150	24.4 ± 4.0	30.5 ± 5.0	30.5 ± 4.9	99	R11	9.7506690	-42.5901630	8.2 ± 4.3	23.2 ± 5.1	30.4 ± 4.9	99
x39	7.4767650	-42.3724560	26.1 ± 4.0	36.7 ± 4.9	46.3 ± 4.7	99	R12	8.9158070	-45.0944570	20.7 ± 4.3	24.4 ± 5.0	30.3 ± 4.8	99
x40	7.3295750	-42.7385860	20.8 ± 4.0	20.9 ± 4.9	25.2 ± 4.7	99	R13	8.8405350	-45.2788130	12.5 ± 4.7	22.9 ± 5.3	29.5 ± 5.3	99
x41	8.4672190	-45.3357350	21.5 ± 4.0	34.2 ± 4.9	37.6 ± 4.9	99	R15	7.5176500	-44.3423670	19.1 ± 4.6	23.8 ± 5.2	29.4 ± 5.2	99
x43	8.0250060	-45.0015260	22.2 ± 4.0	27.5 ± 4.9	28.1 ± 4.7	99	R16	8.9019500	-43.9100070	14.7 ± 4.0	26.9 ± 4.9	29.0 ± 4.6	0
x45	9.2921090	-43.7120600	26.3 ± 4.0	27.0 ± 4.9	28.2 ± 4.7	0	R17	7.9397140	-42.0873940	20.0 ± 4.5	21.6 ± 5.2	27.8 ± 5.1	99
x46	7.9919200	-43.9876900	21.2 ± 4.0	24.9 ± 4.9	25.0 ± 4.8	0	R18	7.4465620	-42.3655930	20.5 ± 4.4	25.4 ± 5.4	27.8 ± 5.1	99

Table 13 continued

Table 13 (continued)

ID	RA (degrees)	DEC (degrees)	f_{250} (mJy)	f_{350} (mJy)	f_{500} (mJy)	Radio Code	ID	RA (degrees)	DEC (degrees)	f_{250} (mJy)	f_{350} (mJy)	f_{500} (mJy)	Radio Code
x47	9.2930340	-43.1076300	22.9 ± 4.0	32.0 ± 4.9	32.0 ± 4.7	0	R19	7.9437990	-45.2825770	15.7 ± 4.5	23.7 ± 5.3	27.2 ± 5.2	99
x49	8.8640320	-42.5011180	19.4 ± 4.0	23.3 ± 4.9	29.9 ± 5.0	99	R20	7.5004040	-44.2993590	18.2 ± 4.5	26.1 ± 5.3	26.6 ± 5.2	99
x51	10.4830060	-43.0886340	28.2 ± 4.0	36.2 ± 4.9	37.5 ± 4.8	99	R26	7.9629710	-43.7610050	13.8 ± 4.4	21.0 ± 5.2	25.8 ± 5.1	0
x53	9.7077120	-42.2273030	23.2 ± 4.0	25.1 ± 4.9	25.6 ± 4.7	99	R27	10.1876680	-44.5124800	10.2 ± 4.0	22.6 ± 4.8	24.0 ± 4.6	99
500R_FLS_T1_x02	259.7872300	60.1205520	36.0 ± 5.5	40.8 ± 6.0	41.0 ± 5.9	99	x35	256.5182000	58.4881900	26.7 ± 5.5	28.1 ± 6.2	31.8 ± 5.8	99
x03	257.2208600	58.8160970	39.0 ± 5.5	43.6 ± 6.3	46.8 ± 6.0	99	x36	256.6789600	60.6350400	26.1 ± 5.5	30.6 ± 6.0	30.6 ± 5.8	99
x04	261.5066800	60.1805150	35.8 ± 5.5	39.2 ± 6.0	40.3 ± 5.8	99	x37	258.2403300	59.7001400	25.8 ± 5.5	30.9 ± 6.0	34.8 ± 5.8	99
x06	258.3609600	58.4001580	47.0 ± 5.5	50.1 ± 6.1	53.6 ± 5.9	99	x42	256.6977000	60.2464830	16.3 ± 5.5	23.7 ± 6.0	30.9 ± 5.8	99
x07	261.3957200	58.8613130	39.1 ± 5.5	43.3 ± 6.1	45.5 ± 5.9	1	x43	256.8321200	60.4376400	33.2 ± 5.5	53.2 ± 6.0	61.1 ± 5.9	99
x09	260.2061800	59.7744940	27.8 ± 5.5	46.7 ± 6.0	48.7 ± 5.8	99	x44	256.6993400	58.7729720	17.0 ± 5.5	33.4 ± 6.1	44.3 ± 6.1	99
x11	259.7167400	59.9014300	28.4 ± 5.5	33.1 ± 6.0	35.0 ± 5.8	1	x45	256.8684700	60.2745900	23.4 ± 5.5	31.1 ± 6.0	37.3 ± 5.8	99
x12	261.1949500	59.5561560	21.1 ± 5.5	32.1 ± 6.0	33.7 ± 5.8	99	x46	260.7970300	60.3312030	16.2 ± 5.5	25.7 ± 6.2	33.8 ± 6.6	99
x13	261.0537000	58.1153260	32.1 ± 5.6	42.4 ± 6.1	46.1 ± 6.5	99	x49	261.0396000	58.3882400	27.8 ± 5.5	34.9 ± 6.2	38.8 ± 6.7	99
x14	256.7055700	59.3762600	31.1 ± 5.5	39.5 ± 6.1	41.7 ± 6.0	99	x50	260.8136600	59.1536560	20.0 ± 5.5	29.6 ± 6.0	32.3 ± 5.9	1
x15	259.8840300	60.4752240	25.4 ± 5.5	41.6 ± 6.1	41.9 ± 5.8	99	R01	258.2862780	59.1571580	33.6 ± 5.6	49.2 ± 6.0	51.0 ± 5.8	99
x16	259.2150600	58.3634640	31.9 ± 5.5	36.0 ± 6.0	38.2 ± 5.9	99	R02	257.0850120	60.0418170	32.2 ± 5.5	43.4 ± 6.0	46.5 ± 5.8	99
x18	257.1197500	59.6780100	35.9 ± 5.5	42.2 ± 6.0	45.0 ± 5.9	99	R03	260.1050360	58.2539910	26.8 ± 5.6	38.2 ± 6.0	43.3 ± 5.8	99
x21	259.2410300	60.1728320	27.8 ± 5.5	46.9 ± 6.1	47.2 ± 5.9	99	R04	256.7723980	60.6496560	16.9 ± 5.8	24.8 ± 6.4	42.1 ± 6.3	99
x23	260.4969500	59.4218500	27.5 ± 5.5	29.0 ± 6.1	33.2 ± 6.1	99	R05	260.0490780	58.8437580	19.9 ± 5.6	34.8 ± 6.1	39.9 ± 5.8	99
x28	258.6703000	58.3429300	27.3 ± 5.5	33.4 ± 6.3	34.7 ± 6.9	1	R07	259.3683640	59.2924290	25.3 ± 5.6	36.4 ± 6.0	38.6 ± 5.8	99
x29	260.3498000	59.2983250	23.5 ± 5.5	27.9 ± 6.0	32.8 ± 6.0	99	R10	260.1893690	58.5978440	24.0 ± 5.6	25.6 ± 6.0	36.1 ± 5.8	99
x30	259.6657400	58.3446350	23.9 ± 5.5	38.7 ± 6.1	41.6 ± 5.9	1	R11	257.8784960	59.6585270	16.8 ± 5.5	25.7 ± 6.0	35.4 ± 5.8	99
x31	257.9499200	58.5761570	40.6 ± 5.5	56.1 ± 6.0	64.4 ± 5.8	99	R13	258.9340220	59.1486130	13.3 ± 5.6	21.3 ± 6.1	32.5 ± 5.8	99
x32	258.7505800	60.4297300	17.6 ± 5.6	22.3 ± 6.0	32.5 ± 5.8	99	R16	257.7951780	59.3413190	20.1 ± 5.6	28.6 ± 6.0	29.1 ± 5.8	99
x33	259.7567700	59.2779100	25.7 ± 5.5	27.4 ± 6.0	30.2 ± 5.8	99							
500R_GOODSN_T1_x01	189.7736000	62.0934260	31.1 ± 2.1	43.2 ± 2.8	43.5 ± 3.5	0	x10	189.9244100	62.4236800	17.2 ± 2.1	26.3 ± 2.8	27.6 ± 3.4	99
x03	188.7572500	62.3737750	21.7 ± 2.1	26.8 ± 2.8	29.2 ± 3.4	0	x16	188.3899000	62.1568570	11.7 ± 2.1	18.2 ± 2.8	24.1 ± 3.4	99
x09	189.7990600	62.0264130	17.9 ± 2.1	22.7 ± 2.8	24.1 ± 3.4	0	x20	188.7918400	62.1868200	10.9 ± 2.1	16.8 ± 2.8	18.9 ± 3.4	1
500R_LH_T1_x001	160.2103100	56.1147500	64.9 ± 3.8	119.2 ± 4.8	137.5 ± 4.5	0	x188	157.6477700	57.8652530	21.2 ± 3.8	22.3 ± 4.8	26.0 ± 4.6	0
x002	165.4973300	58.6576540	70.3 ± 0.0	72.6 ± 4.8	75.2 ± 0.0	0	x190	163.4511600	56.7920880	16.9 ± 3.8	25.4 ± 4.8	25.7 ± 4.5	0
x003	159.4345600	57.1986000	56.2 ± 3.8	61.4 ± 4.8	64.7 ± 4.7	1	x191	165.0856500	57.4782900	15.1 ± 3.8	24.0 ± 4.8	25.1 ± 4.6	99
x005	160.4710200	58.7568550	49.0 ± 3.8	68.2 ± 4.8	70.8 ± 4.8	0	x192	159.8823500	56.7337800	18.7 ± 3.8	24.9 ± 4.8	25.4 ± 4.6	0
x006	162.9744400	60.5200900	37.0 ± 3.8	41.6 ± 4.8	50.3 ± 5.2	99	x196	160.7510000	57.8922800	18.6 ± 3.8	27.5 ± 4.8	29.8 ± 4.5	0
x012	162.4874600	58.5641140	41.7 ± 3.8	48.3 ± 4.8	50.2 ± 4.6	0	x199	161.4817800	57.9256320	16.4 ± 3.8	22.0 ± 4.8	23.2 ± 4.5	0
x014	165.4424600	57.6662980	35.3 ± 3.8	45.1 ± 4.8	52.0 ± 4.5	99	x201	159.9243500	58.5299700	16.7 ± 3.8	22.8 ± 4.8	23.0 ± 4.5	0
x016	156.2868500	59.0083240	42.9 ± 3.8	46.9 ± 4.8	48.7 ± 4.6	99	x203	163.8069500	58.8959540	13.4 ± 3.8	21.5 ± 4.8	25.6 ± 4.5	0
x017	165.3661800	59.8619420	42.1 ± 0.0	43.2 ± 4.8	45.8 ± 0.0	99	x204	162.6299700	56.5125730	19.8 ± 3.8	33.6 ± 4.8	37.0 ± 4.7	99
x019	157.2983100	57.6911050	32.9 ± 3.8	43.0 ± 4.9	43.4 ± 5.3	0	x206	160.2573200	56.3359450	18.3 ± 3.8	27.2 ± 4.9	27.9 ± 5.2	0
x021	157.1233500	59.2248880	36.4 ± 3.8	37.3 ± 4.8	40.9 ± 4.7	99	x208	161.38665400	60.0077440	20.6 ± 3.8	27.8 ± 4.8	31.5 ± 4.7	0

Table 13 continued

Table 13 (continued)

ID	RA (degrees)	DEC (degrees)	f_{250} (mJy)	f_{350} (mJy)	f_{500} (mJy)	Radio Code	ID	RA (degrees)	DEC (degrees)	f_{250} (mJy)	f_{350} (mJy)	f_{500} (mJy)	Radio Code
x028	165.7378700	58.009260	34.5 ± 3.8	47.8 ± 4.8	51.8 ± 4.6	99	x211	164.7647100	58.3363880	15.7 ± 3.8	20.1 ± 4.8	26.0 ± 4.5	0
x029	157.2097200	58.2731000	22.7 ± 3.8	26.2 ± 4.8	27.4 ± 4.6	99	x212	162.6342600	55.6990130	21.7 ± 3.8	28.6 ± 4.8	29.4 ± 4.6	99
x034	162.6435200	60.5433000	34.2 ± 3.8	34.4 ± 4.8	34.5 ± 5.0	99	x214	158.6432200	56.5285450	21.8 ± 3.8	23.5 ± 4.8	27.2 ± 4.6	99
x038	157.6440900	57.8923000	29.2 ± 3.8	38.6 ± 4.8	42.0 ± 4.7	0	x215	157.8736400	58.5639900	20.2 ± 3.8	25.6 ± 4.8	28.4 ± 4.6	99
x039	160.1574000	55.6817050	28.3 ± 3.8	39.7 ± 4.8	44.2 ± 4.7	1	x216	159.8366200	59.8805540	14.3 ± 3.8	20.9 ± 4.8	24.9 ± 4.5	0
x041	157.5173600	58.009260	24.4 ± 3.8	29.5 ± 4.8	31.4 ± 4.6	0	x217	160.3839700	59.6642840	19.8 ± 3.8	29.0 ± 4.8	29.4 ± 4.8	0
x045	163.9036400	59.5162400	30.4 ± 3.8	31.3 ± 4.8	31.9 ± 4.7	99	x224	159.8995500	57.1155240	12.7 ± 3.8	20.5 ± 4.8	22.7 ± 4.5	0
x046	164.6024600	56.7853000	26.5 ± 3.8	26.7 ± 4.8	28.9 ± 4.9	99	x226	161.0703700	60.1694680	14.3 ± 3.8	30.2 ± 4.8	30.3 ± 4.6	0
x048	162.5957000	55.7876100	27.8 ± 3.8	30.1 ± 4.7	30.5 ± 4.4	99	x230	158.8239900	56.7683100	15.3 ± 3.8	29.8 ± 4.8	30.3 ± 4.6	0
x049	165.3606400	56.8361740	32.5 ± 3.8	37.6 ± 4.8	39.4 ± 5.0	99	x231	164.1621700	59.6258400	15.1 ± 3.9	21.1 ± 4.8	33.3 ± 4.5	99
x050	163.6935300	59.6084630	25.4 ± 3.8	32.9 ± 4.8	37.6 ± 4.5	99	x233	159.9667700	56.8604350	19.9 ± 3.8	30.8 ± 4.8	35.6 ± 4.6	0
x056	162.8832000	56.6057660	24.8 ± 3.8	38.9 ± 4.8	45.1 ± 4.5	0	x235	159.8640000	57.0078700	17.9 ± 3.8	24.4 ± 4.8	26.1 ± 5.2	0
x057	161.7783800	55.8344400	30.6 ± 3.8	33.4 ± 5.1	36.2 ± 5.6	0	x238	160.0268600	56.4916730	17.0 ± 3.8	24.7 ± 4.8	25.3 ± 4.5	0
x058	157.9663800	57.7215350	27.6 ± 3.8	34.4 ± 4.8	34.8 ± 4.5	0	x239	159.7755700	57.1365000	12.0 ± 3.8	18.6 ± 4.8	23.2 ± 4.5	0
x061	163.8057900	56.2244640	26.3 ± 3.7	38.5 ± 4.8	42.7 ± 4.6	99	x240	159.6128800	59.2551880	16.9 ± 3.8	22.9 ± 4.8	24.8 ± 4.8	0
x062	161.2159000	57.3971860	26.5 ± 3.8	29.9 ± 4.8	29.9 ± 4.6	0	x245	162.9422500	58.0646500	19.8 ± 3.8	27.9 ± 4.8	30.5 ± 4.6	0
x063	163.7543300	57.1250080	23.1 ± 3.8	26.7 ± 4.8	27.5 ± 4.7	0	x248	163.1489700	58.0137900	15.3 ± 3.8	27.3 ± 4.8	31.5 ± 4.7	0
x067	162.0749000	58.3494070	29.9 ± 3.8	34.3 ± 4.8	34.8 ± 4.8	0	x249	165.3836800	58.0452100	17.7 ± 3.8	27.5 ± 4.8	30.7 ± 4.9	0
x070	165.3189800	58.5554470	36.3 ± 3.8	39.8 ± 4.8	40.5 ± 4.7	0	x252	160.1281300	56.8181150	15.8 ± 3.8	24.4 ± 4.8	26.1 ± 4.7	0
x071	163.5534200	56.6875700	22.9 ± 3.8	23.8 ± 4.8	24.8 ± 4.7	99	x257	157.5387700	59.2476040	19.6 ± 3.8	24.2 ± 4.8	28.8 ± 4.5	99
x076	161.5572700	55.6107250	26.6 ± 3.8	37.1 ± 4.7	42.9 ± 4.5	0	x262	160.7136100	57.5219200	12.9 ± 3.8	23.2 ± 4.8	27.5 ± 4.5	99
x078	162.7648800	59.2746930	21.0 ± 3.8	24.6 ± 4.8	29.3 ± 5.2	0	R01	164.9188950	59.5097300	40.2 ± 5.7	53.4 ± 6.3	60.9 ± 6.5	99
x080	159.9581100	57.1879600	27.8 ± 3.8	29.8 ± 4.8	30.1 ± 4.7	0	R02	161.0740510	55.4109330	29.1 ± 5.0	37.9 ± 5.6	58.5 ± 6.0	99
x082	157.5438500	59.2835700	21.0 ± 3.8	26.2 ± 4.8	29.9 ± 4.6	99	R03	165.8240660	59.6815300	35.7 ± 6.3	53.4 ± 6.9	57.4 ± 7.5	99
x083	165.6189000	58.0033870	26.7 ± 3.8	29.8 ± 4.8	29.9 ± 4.5	99	R06	165.1978470	59.3353470	24.6 ± 5.6	44.6 ± 6.0	53.2 ± 6.7	99
x085	163.3653100	56.4301220	27.6 ± 3.8	32.0 ± 4.8	36.0 ± 4.7	0	R08	163.6534670	60.3856530	31.6 ± 4.5	47.3 ± 5.2	52.1 ± 5.3	99
x090	163.5243500	56.4503940	19.4 ± 3.8	28.1 ± 4.8	30.0 ± 4.5	0	R10	166.4412750	57.1884430	34.3 ± 4.8	44.6 ± 5.4	49.4 ± 5.8	99
x092	159.9470000	59.0228200	23.7 ± 3.8	28.2 ± 4.8	28.6 ± 4.6	0	R11	159.9566930	56.6216570	31.1 ± 3.9	45.5 ± 4.7	46.6 ± 4.6	0
x093	163.1306900	56.7429580	25.9 ± 3.8	34.4 ± 4.8	39.4 ± 5.1	0	R13	165.3718850	58.6555980	21.7 ± 5.0	39.9 ± 5.7	46.3 ± 5.9	0
x096	157.5291300	58.0450970	22.7 ± 3.8	29.7 ± 4.8	30.7 ± 4.6	0	R14	156.0292580	58.9669930	28.2 ± 4.7	41.5 ± 5.4	45.7 ± 5.7	99
x097	163.6224400	59.4118300	27.4 ± 3.8	30.2 ± 4.8	30.9 ± 4.6	0	R16	156.4030410	58.9480680	29.3 ± 4.4	37.5 ± 5.1	39.6 ± 5.2	99
x098	166.0936600	57.2025450	24.9 ± 3.8	26.4 ± 4.8	34.9 ± 4.5	99	R18	161.2003440	60.5559280	20.1 ± 5.1	35.0 ± 5.8	39.0 ± 5.7	99
x099	160.3612000	57.2526440	20.2 ± 3.8	28.1 ± 4.8	29.7 ± 4.5	0	R22	159.6929880	56.1620990	25.7 ± 4.0	30.7 ± 4.8	37.3 ± 4.7	0
x103	157.5592300	58.8311900	22.1 ± 3.8	26.9 ± 4.9	30.5 ± 5.2	99	R27	158.0416600	56.7689050	26.8 ± 4.3	32.2 ± 5.1	36.1 ± 5.2	0
x105	160.7376400	59.6635630	26.0 ± 3.8	33.1 ± 4.8	35.0 ± 4.8	0	R28	158.5426840	59.6248530	18.5 ± 4.5	35.7 ± 5.3	35.8 ± 5.3	99
x107	164.6179500	57.6990130	25.0 ± 3.8	31.2 ± 4.8	35.3 ± 4.8	0	R30	164.5306600	59.7918730	20.7 ± 5.6	22.9 ± 6.4	35.4 ± 6.6	99
x110	162.9453100	58.3270340	23.0 ± 3.8	33.0 ± 4.8	35.2 ± 4.7	0	R31	163.7113080	60.0975740	22.6 ± 4.2	32.0 ± 5.0	34.9 ± 5.0	99
x118	161.9691200	60.1344800	25.2 ± 3.8	34.8 ± 4.8	36.6 ± 4.9	99	R32	158.8485150	59.9731210	19.6 ± 5.1	27.4 ± 5.8	34.8 ± 6.3	99
x119	161.3193700	58.3547060	24.6 ± 3.8	28.6 ± 4.8	29.7 ± 4.9	0	R33	164.3138850	56.4151980	29.5 ± 4.8	33.1 ± 5.4	34.6 ± 5.5	99

Table 13 continued

Table 13 (continued)

ID	RA (degrees)	DEC (degrees)	f_{250} (mJy)	f_{350} (mJy)	f_{500} (mJy)	Radio Code	ID	RA (degrees)	DEC (degrees)	f_{250} (mJy)	f_{350} (mJy)	f_{500} (mJy)	Radio Code
x125	159.5949600	59.6118850	23.3 ± 3.8	31.7 ± 4.8	33.6 ± 5.4	0	R37	161.7022040	55.6209620	11.5 ± 4.7	26.8 ± 5.5	33.8 ± 5.5	0
x126	162.7170100	56.4316750	19.7 ± 3.8	26.6 ± 4.8	30.9 ± 4.5	0	R39	157.1564300	57.8825660	10.3 ± 4.3	12.2 ± 5.2	33.1 ± 5.2	0
x127	162.5613900	58.9401100	22.8 ± 3.8	30.4 ± 4.8	32.8 ± 4.6	0	R43	162.0889880	58.6611880	19.5 ± 3.7	28.3 ± 4.6	31.2 ± 4.5	0
x130	163.5031000	59.7616460	22.4 ± 3.8	31.8 ± 4.8	33.0 ± 4.5	99	R45	161.2803730	55.9559260	20.2 ± 4.0	29.6 ± 4.8	31.0 ± 4.8	0
x136	159.3364900	59.6548160	18.5 ± 3.8	23.8 ± 4.8	24.7 ± 4.6	0	R47	157.7468550	59.3377740	18.6 ± 4.4	24.9 ± 5.1	30.8 ± 5.1	99
x137	162.1767700	57.4715770	20.9 ± 3.8	26.5 ± 4.8	29.1 ± 4.7	0	R48	157.5894250	59.3804780	9.7 ± 4.7	17.9 ± 5.3	30.7 ± 5.5	99
x138	162.9243200	59.6706850	24.7 ± 3.8	26.8 ± 4.8	38.3 ± 4.5	0	R50	161.7618730	55.7468060	16.3 ± 4.0	29.1 ± 4.9	30.2 ± 4.8	0
x142	156.6864800	58.4602280	18.1 ± 3.8	27.0 ± 4.8	27.8 ± 4.6	99	R51	157.6950370	57.7577770	14.1 ± 3.9	22.8 ± 4.8	29.7 ± 4.7	0
x148	164.3733800	59.7304800	19.9 ± 3.8	24.6 ± 4.8	26.0 ± 5.0	99	R52	161.6336420	60.3369590	17.5 ± 4.0	28.6 ± 4.9	29.0 ± 4.8	99
x149	158.2025500	56.3381600	28.0 ± 3.9	43.5 ± 4.8	50.2 ± 5.3	99	R55	164.9715000	58.5906830	18.5 ± 3.9	26.5 ± 4.8	27.3 ± 4.7	0
x154	160.8355100	57.3465040	16.5 ± 3.8	20.6 ± 4.8	25.0 ± 4.6	0	R56	162.6942610	60.5302920	17.1 ± 4.4	24.4 ± 5.2	27.0 ± 5.1	99
x155	162.1904000	59.8251400	13.5 ± 3.8	19.4 ± 4.8	22.6 ± 4.5	0	R57	157.6725480	58.0445660	9.2 ± 3.8	21.7 ± 4.7	26.6 ± 4.6	0
x162	160.9322700	56.0268330	18.9 ± 3.8	27.3 ± 4.8	29.9 ± 4.7	0	R58	159.8182410	57.8763440	20.0 ± 3.8	24.3 ± 4.7	26.5 ± 4.6	0
x170	160.8808300	57.9549670	16.4 ± 3.8	26.0 ± 4.8	27.3 ± 4.5	0	R61	164.7121570	56.8519660	13.2 ± 3.8	24.4 ± 4.7	26.1 ± 4.6	99
x171	162.8708200	56.0687520	25.4 ± 3.8	29.8 ± 4.8	32.2 ± 4.5	99	R66	159.3201820	56.2519120	15.9 ± 4.0	22.9 ± 4.9	25.1 ± 4.8	0
x172	162.1929800	58.4518050	26.1 ± 3.8	28.3 ± 4.8	29.1 ± 4.6	0	R67	161.2083850	59.6262550	4.9 ± 3.8	17.6 ± 4.7	25.1 ± 4.6	0
x173	159.6956800	56.1868320	23.9 ± 3.8	28.9 ± 4.8	32.4 ± 5.2	0	R68	163.5320850	58.3045100	11.8 ± 3.8	19.4 ± 4.7	24.9 ± 4.6	0
x174	163.0163600	58.5649220	17.3 ± 3.8	22.3 ± 4.8	25.6 ± 4.9	0	R70	156.6459850	58.5453700	15.2 ± 4.0	21.6 ± 4.8	24.4 ± 4.8	99
x179	165.5440500	58.0698240	24.8 ± 3.8	24.9 ± 4.8	25.5 ± 4.8	0	R71	165.0245530	58.5239100	5.2 ± 3.9	13.5 ± 4.8	24.3 ± 4.8	0
x180	161.6305500	59.9054570	24.6 ± 3.8	25.8 ± 4.8	26.7 ± 4.5	0	R73	160.2602280	56.9672890	12.0 ± 3.8	23.5 ± 4.7	24.2 ± 4.6	0
x184	164.2049700	58.5325280	20.2 ± 3.8	25.2 ± 4.8	27.7 ± 4.6	0							
500R_XMMLSS_T1_x01	35.4638750	-6.7881400	42.7 ± 4.5	45.7 ± 8.2	52.0 ± 7.1	99	x77	37.5646440	-4.1012730	25.6 ± 4.6	30.3 ± 7.6	32.0 ± 6.3	99
x03	36.2023200	-4.2065420	46.0 ± 4.5	57.4 ± 7.6	59.2 ± 6.3	99	x81	34.4320900	-3.1526560	25.0 ± 4.5	39.2 ± 7.7	46.8 ± 6.7	99
x05	35.2150000	-3.5765250	44.4 ± 4.5	46.4 ± 7.7	63.7 ± 6.3	99	x83	34.8303260	-6.7639270	15.4 ± 4.6	32.8 ± 7.6	32.8 ± 6.3	1
x07	36.1155500	-4.8230660	31.8 ± 4.5	45.5 ± 7.7	47.2 ± 6.4	99	x84	37.7175370	-4.4059930	26.1 ± 4.6	27.2 ± 7.8	40.9 ± 7.2	99
x08	34.2053870	-2.3493410	33.8 ± 4.6	36.3 ± 7.7	45.2 ± 6.3	99	x95	36.9986400	-5.5569910	28.3 ± 4.6	49.2 ± 7.6	62.6 ± 6.3	99
x12	32.5189100	-4.9609560	34.0 ± 4.6	40.6 ± 7.6	42.7 ± 6.4	99	R01	35.5499030	-7.0390710	24.2 ± 5.7	46.5 ± 8.2	77.8 ± 7.4	99
x13	37.3286700	-3.3225070	37.8 ± 4.5	43.9 ± 7.6	50.4 ± 6.4	99	R02	37.3702490	-3.4341550	43.4 ± 5.6	49.9 ± 8.2	54.6 ± 7.4	99
x18	35.9399200	-2.6448750	33.9 ± 4.6	40.2 ± 7.6	44.5 ± 6.4	99	R03	35.2198110	-7.2153330	25.2 ± 6.0	32.1 ± 8.8	49.1 ± 7.7	99
x22	34.8219900	-2.2439880	32.8 ± 4.6	38.0 ± 7.7	43.6 ± 6.8	99	R04	35.2859100	-7.1726580	27.6 ± 5.6	38.6 ± 8.2	47.0 ± 7.1	99
x26	35.6203500	-4.2926400	33.8 ± 4.5	34.6 ± 7.6	37.2 ± 6.3	99	R06	36.5244140	-3.3076310	18.1 ± 5.1	37.8 ± 7.9	44.3 ± 6.7	99
x30	33.3256450	-2.9493650	33.5 ± 4.6	35.6 ± 7.7	37.2 ± 6.8	99	R07	33.1355210	-4.7839840	29.8 ± 5.1	39.5 ± 7.9	44.1 ± 6.7	99
x32	35.2069360	-3.5443820	30.5 ± 4.5	37.8 ± 7.7	42.2 ± 6.7	99	R08	36.0208140	-6.5047160	32.8 ± 5.1	42.5 ± 8.0	42.9 ± 6.7	99
x33	35.6233830	-4.4421260	27.1 ± 4.5	35.1 ± 7.7	39.1 ± 6.9	99	R09	35.4270090	-5.9561270	29.1 ± 5.1	41.5 ± 7.9	42.8 ± 6.6	99
x44	37.0219080	-5.2028940	23.2 ± 4.6	40.2 ± 7.6	42.5 ± 6.3	99	R11	33.4903300	-5.9040590	25.1 ± 5.6	29.7 ± 8.2	41.6 ± 7.1	99
x46	34.7346700	-4.5947770	30.8 ± 4.5	43.4 ± 7.6	44.0 ± 6.4	99	R12	33.8941210	-3.6739460	17.0 ± 5.1	39.7 ± 7.9	40.7 ± 6.8	99
x51	34.5510030	-3.6252920	31.5 ± 4.5	37.5 ± 7.6	38.8 ± 6.4	99	R13	32.8288620	-4.5427930	21.9 ± 5.7	39.1 ± 8.6	39.7 ± 7.1	99
x52	37.6737630	-3.9850090	36.2 ± 4.6	50.9 ± 7.7	51.5 ± 6.8	99	R15	34.8945750	-2.9320120	-0.6 ± 5.1	27.0 ± 7.9	39.5 ± 6.7	99
x55	34.8089800	-4.6281540	25.7 ± 4.5	37.7 ± 7.6	37.9 ± 6.3	99	R16	35.3064850	-2.2784060	21.0 ± 5.3	38.4 ± 8.0	38.5 ± 6.8	99

Table 13 continued

Table 13 (*continued*)

ID	RA (degrees)	DEC (degrees)	f_{250} (mJy)	f_{350} (mJy)	f_{500} (mJy)	Radio Code	ID	RA (degrees)	DEC (degrees)	f_{250} (mJy)	f_{350} (mJy)	f_{500} (mJy)	Radio Code
x56	35.4444050	-3.7358530	30.2 \pm 4.6	37.9 \pm 7.8	41.8 \pm 6.6	99	R17	35.1615470	-6.7988910	24.8 \pm 5.6	34.5 \pm 8.2	38.3 \pm 7.3	99
x59	36.7346800	-3.4521300	30.2 \pm 4.5	49.7 \pm 7.7	55.6 \pm 6.6	99	R19	35.0419490	-2.7736710	18.8 \pm 5.1	31.7 \pm 7.9	35.7 \pm 6.6	99
x61	33.4610900	-3.3534510	20.6 \pm 4.6	24.0 \pm 7.6	32.8 \pm 6.3	99	R20	33.0884220	-4.1131160	25.1 \pm 5.1	32.4 \pm 7.9	35.5 \pm 6.7	99
x62	34.1221350	-4.4218690	24.7 \pm 4.5	40.2 \pm 7.6	40.8 \pm 6.3	99	R21	33.2329800	-4.1399960	28.3 \pm 5.1	34.8 \pm 7.9	35.2 \pm 6.7	99
x63	35.7164840	-3.2421370	23.1 \pm 4.5	35.5 \pm 7.7	38.3 \pm 6.7	99	R23	33.6404160	-4.3430560	20.6 \pm 5.1	34.5 \pm 7.9	34.5 \pm 6.7	99
x70	34.1848600	-5.0404740	29.8 \pm 4.5	35.1 \pm 7.7	39.4 \pm 6.5	0	R25	34.0929370	-6.0485150	19.8 \pm 5.1	33.4 \pm 7.9	34.0 \pm 6.8	99
x71	35.2055800	-6.0045300	21.0 \pm 4.6	32.6 \pm 7.7	38.3 \pm 6.3	99	R26	35.3921270	-2.3801770	18.2 \pm 5.0	28.2 \pm 7.9	33.3 \pm 6.7	99
x74	35.1017300	-3.0180250	30.8 \pm 4.6	33.5 \pm 7.6	35.7 \pm 6.3	99	R27	34.7219570	-3.7016850	17.0 \pm 5.0	28.4 \pm 7.9	33.2 \pm 6.6	99

NOTE—Full catalog of Tier 1 500 μ m risers. See Table 3 caption for the description of the table columns. The 350 μ m confusion noise in the ELAIS-N2 field is abnormally high based on the HerMES DR4 catalog; nevertheless this does not affect our selection.

Table 14. Catalog of Tier 1 SPIRE dropouts based on S2CLS 850 μm data

Object Name	RA ₈₅₀ (degrees)	DEC ₈₅₀ (degrees)	S/N ₈₅₀	S ₈₅₀ (mJy)	RA _{SPIRE} (degrees)	DEC _{SPIRE} (degrees)	f ₂₅₀ (mJy)	f ₃₅₀ (mJy)	f ₅₀₀ (mJy)	Δ ($''$)	Radio Code
SD850_COSMOS_T1_A02	150.038273	2.140164	9.0	9.0 \pm 1.3	0
A03	149.989321	2.457937	8.7	11.8 \pm 1.9	0
A04	149.792953	2.815101	8.3	11.7 \pm 2.1	1
A06	149.475156	2.085589	7.1	9.5 \pm 2.0	0
A07	149.781791	2.976741	6.9	9.5 \pm 2.0	0
A08	150.101092	2.334055	6.7	6.2 \pm 1.5	0
A10	149.881993	2.511809	6.1	7.9 \pm 1.9	0
A11	149.879814	2.242368	6.0	5.4 \pm 1.4	1
A12	149.411846	1.970017	5.8	7.6 \pm 1.8	0
A13	149.958243	1.920718	5.7	6.7 \pm 1.6	0
A15	150.071089	1.724625	5.6	5.8 \pm 1.4	1
A18	149.645181	2.300642	5.4	5.1 \pm 1.3	1
A19	150.121665	2.090167	5.3	5.1 \pm 1.2	0
A20	150.196163	2.171276	5.3	4.7 \pm 1.2	1
A22	150.097205	2.021279	5.2	5.5 \pm 1.4	0
A23	149.995427	2.582379	5.2	6.3 \pm 1.7	1
A26	150.034929	2.284053	5.2	4.0 \pm 0.9	0
A29	149.679013	2.568419	5.1	6.3 \pm 1.8	0
A30	149.681180	2.754516	5.1	6.7 \pm 1.8	1
A31	149.851046	1.485195	5.0	7.2 \pm 2.0	0
B03	150.109433	2.257389	6.7	5.5 \pm 1.1	150.109220	2.256556	2.5 \pm 3.4	3.4 \pm 6.6	0.0 \pm 13.0	3.1	0
B05	150.027677	2.642935	6.3	8.0 \pm 1.8	150.027700	2.642787	3.9 \pm 3.4	8.5 \pm 6.6	12.9 \pm 5.0	0.5	0
B06	150.088867	2.010723	6.0	6.3 \pm 1.4	150.087950	2.011739	3.7 \pm 3.4	5.5 \pm 6.6	5.2 \pm 5.2	4.9	1
B07	149.390370	2.678273	5.9	8.5 \pm 1.9	149.389980	2.677629	5.8 \pm 3.4	9.7 \pm 6.6	6.7 \pm 5.3	2.7	0
B14	150.096646	2.229055	5.3	4.1 \pm 0.9	150.095660	2.229530	10.0 \pm 3.4	10.4 \pm 6.6	8.7 \pm 5.1	3.9	1
B16	150.155036	2.819592	5.2	6.3 \pm 1.6	150.154080	2.820342	6.1 \pm 3.4	6.9 \pm 6.6	6.4 \pm 5.1	4.4	1
SD850_EGS_T1_A09	214.949397	52.911500	5.7	5.7 \pm 1.4	0
A11	214.599005	52.890286	5.5	7.1 \pm 1.7	0
A12	214.353485	52.587132	5.4	4.7 \pm 1.1	0
A13	214.939372	52.991022	5.2	5.0 \pm 1.3	0
A16	213.892437	52.253694	5.0	4.6 \pm 1.3	99
B03	213.767385	52.169767	5.7	6.0 \pm 1.5	213.766140	52.171010	3.1 \pm 3.5	6.8 \pm 4.1	9.2 \pm 4.3	5.2	99
SD850_GOODSN_T1_A01	189.113499	62.204072	7.3	6.7 \pm 1.4	0
A02	189.218337	62.207453	7.1	5.9 \pm 1.3	0
B01	189.133490	62.286865	7.5	7.2 \pm 1.2	189.134600	62.287964	5.5 \pm 2.1	8.0 \pm 2.8	6.8 \pm 3.4	4.4	1
SD850_LH_T1_A02	161.257607	59.067536	7.1	6.8 \pm 1.4	1

Table 14 *continued*

Table 14 (*continued*)

Object Name	RA ₈₅₀ (degrees)	DEC ₈₅₀ (degrees)	S/N ₈₅₀	S ₈₅₀ (mJy)	RA _{SPiRE} (degrees)	DEC _{SPiRE} (degrees)	f ₂₅₀ (mJy)	f ₃₅₀ (mJy)	f ₅₀₀ (mJy)	Δ ($''$)	Radio Code
A03	161.837264	58.864684	6.6	6.3 ± 1.6	1
A04	161.589142	58.909478	5.2	4.7 ± 1.2	0
SD850_UDS_T1_A05	34.364277	-5.112469	8.8	7.5 ± 1.2	0
A08	34.192897	-5.467413	8.0	6.7 ± 1.2	0
A09	34.787128	-5.232388	7.9	6.4 ± 1.1	1
A10	34.365367	-5.294135	7.8	6.2 ± 1.2	0
A11	34.807265	-5.330707	7.6	5.8 ± 1.1	0
A15	34.171888	-5.020192	7.3	6.0 ± 1.2	0
A16	34.682602	-4.652448	7.3	6.7 ± 1.4	0
A18	34.459098	-4.995253	7.1	5.6 ± 1.1	0
A19	34.497583	-5.084696	7.1	5.9 ± 1.1	0
A23	34.590231	-5.376903	6.9	5.6 ± 1.2	0
A33	34.657716	-5.271331	6.4	4.9 ± 1.1	0
A34	34.386570	-5.275804	6.3	5.0 ± 1.1	0
A36	34.201459	-4.983538	6.0	4.8 ± 1.1	0
A37	34.431755	-5.445248	5.9	4.5 ± 1.1	0
A38	34.525424	-4.659147	5.9	4.7 ± 1.1	0
A39	34.144934	-5.403505	5.9	4.5 ± 1.1	0
A40	34.132886	-4.947953	5.9	4.7 ± 1.0	0
A41	34.175191	-5.117415	5.9	4.8 ± 1.1	1
A42	34.499236	-4.781922	5.8	4.5 ± 1.1	0
A45	34.184702	-5.050197	5.7	4.4 ± 1.1	0
A47	34.638660	-4.968561	5.6	4.4 ± 1.1	0
A48	34.196534	-4.751876	5.6	4.1 ± 1.0	1
A50	34.769932	-5.431835	5.6	4.2 ± 1.1	0
A51	34.270701	-4.660793	5.6	4.7 ± 1.1	0
A54	33.948731	-5.133943	5.5	4.4 ± 1.1	0
A55	34.386059	-4.840807	5.5	4.2 ± 1.1	0
A56	34.332450	-5.287463	5.5	4.1 ± 1.0	0
A57	34.463557	-4.802478	5.5	4.3 ± 1.1	1
A59	34.203636	-5.120760	5.4	4.4 ± 1.1	0
A60	34.177552	-4.817421	5.4	4.2 ± 1.1	0
A61	34.177360	-5.260747	5.4	4.2 ± 1.0	0
A62	34.570122	-5.263020	5.4	4.0 ± 1.0	1
A68	34.403298	-5.401915	5.3	4.0 ± 1.1	0
A71	33.997833	-5.105647	5.1	3.7 ± 1.0	0
A72	34.341386	-5.240798	5.1	3.8 ± 1.0	0
A73	34.140175	-4.866292	5.1	3.9 ± 1.0	0
A78	34.492558	-4.989141	5.1	3.8 ± 1.0	0

Table 14 *continued*

Table 14 (*continued*)

Object Name	RA ₈₅₀ (degrees)	DEC ₈₅₀ (degrees)	S/N ₈₅₀	S ₈₅₀ (mJy)	RA _{SPIRE} (degrees)	DEC _{SPIRE} (degrees)	f ₂₅₀ (mJy)	f ₃₅₀ (mJy)	f ₅₀₀ (mJy)	Δ ($''$)	Radio Code
A79	34.165175	-5.064633	5.1	3.8 ± 1.0	0
A80	33.933212	-5.013935	5.1	4.6 ± 1.3	0
A81	34.513792	-5.459690	5.1	3.8 ± 1.0	0
A82	34.736333	-5.163525	5.1	3.9 ± 1.1	0
A84	34.842361	-5.240134	5.0	3.4 ± 1.0	0
A85	34.175701	-5.226858	5.0	3.6 ± 1.0	0
B04	34.530450	-4.736921	10.2	8.5 ± 1.4	34.530490	-4.737500	7.6 ± 4.6	11.5 ± 7.6	10.0 ± 6.3	2.1	1
B11	34.854024	-5.156240	8.4	6.9 ± 1.2	34.854774	-5.156475	7.6 ± 4.6	8.5 ± 7.6	12.0 ± 6.3	2.8	1
B14	34.094707	-5.414588	7.1	5.7 ± 1.2	34.094696	-5.415883	3.7 ± 4.6	2.0 ± 7.6	1.9 ± 6.3	4.7	0
B16	34.263437	-4.721343	7.0	5.6 ± 1.1	34.262383	-4.722320	6.2 ± 4.6	9.4 ± 7.6	10.9 ± 6.3	5.2	1
B18	34.398269	-5.476356	6.7	5.4 ± 1.1	34.397648	-5.477387	12.8 ± 4.6	14.9 ± 7.6	19.9 ± 6.4	4.3	0
B22	34.722897	-5.046865	6.3	5.2 ± 1.1	34.722443	-5.046918	4.6 ± 4.6	2.7 ± 7.6	2.4 ± 6.3	1.6	0
B24	34.512072	-4.946362	6.1	4.6 ± 1.0	34.511486	-4.945260	8.2 ± 4.6	11.1 ± 7.6	8.4 ± 6.3	4.5	0
B27	34.507623	-5.086918	6.0	4.5 ± 1.1	34.508090	-5.087186	5.4 ± 4.6	6.7 ± 7.6	4.6 ± 6.3	1.9	0
B28	34.610166	-4.743574	6.0	4.9 ± 1.1	34.609160	-4.743804	1.9 ± 4.6	0.4 ± 7.6	0.0 ± 6.3	3.7	0
B32	34.263770	-5.476884	5.8	4.5 ± 1.1	34.263054	-5.475765	10.7 ± 4.6	11.3 ± 7.6	9.9 ± 6.3	4.8	0
B34	34.890702	-4.956778	5.7	4.3 ± 1.0	34.890600	-4.956821	12.6 ± 4.6	12.9 ± 7.6	10.4 ± 6.3	0.4	0
B37	34.071515	-5.005697	5.6	4.1 ± 1.0	34.071117	-5.004618	1.7 ± 4.6	2.7 ± 7.6	3.8 ± 6.3	4.1	0
B42	34.768583	-4.954624	5.4	4.0 ± 1.1	34.768105	-4.953702	1.8 ± 4.6	0.6 ± 7.6	2.4 ± 6.3	3.7	0
B43	34.527745	-5.464688	5.4	4.2 ± 1.0	34.528156	-5.463637	6.9 ± 4.6	10.4 ± 7.6	6.0 ± 6.4	4.1	0

NOTE—Full catalog of Tier 1 SPIRE dropouts. See Table 4 caption for the descriptions of the table columns.